On the numerical simulation of the multilayer injection moulding process

Computational Mechanics

On the numerical simulation of the multilayer injection moulding process

W.F. Zoetelief

CIP-DATA KONINKLIJKE BIBLIOTHEEK, DEN HAAG

Zoetelief, W.F.

On the numerical simulation of the multilayer injection moulding process / / W.F. Zoetelief.-Eindhoven : Instituut Vervolgopleidingen, Technische Universiteit Eindhoven. - Ill.
Opleiding: Computational mechanics. - With ref.
ISBN 90-5282-200-X bound
Subject headings: multilayer injection moulding; numerical simulations.

On the numerical simulation of the multilayer injection moulding process

W.F. Zoetelief

Computational Mechanics
Department of Engineering Fundamentals
Centre for Polymers and Composites
August 1992
(WFW 92.100)

This work was supervised by:
Prof.Dr.Ir. H.E.H. Meijer
Dr.Ir. G.W.M. Peters

Contents

Abstract

In multilayer injection moulding process, two or three polymeric materials are sequentially or simultaneously injected in a mould to make products that, for example, consist of a core layer of a material with specific properties enclosed by a shell layer of another material. For a succesful application of this technique to complex shaped products, it must be known which material has to be injected at what time to get the desired layer distribution. This can be achieved by numerical simulation of the flow during filling of the mould. Particle tracking is modelled by labeling each particle with its "identity". The identity of a particle, for instance its position and time at inflow into the mould, does not change. Therefore this problem can be expressed as a conservation law which can be added to the set of balance and constitutive equations needed to describe the injection moulding process.

The conservation of identity is written as an instationary scalar convection equation. For the numerical solution of this type of equation, a large class of methods are available. Methods based on the Finite Difference Method (FDM) and the Finite Element Method (FEM) are tested with the convection of a Gaussian hill. For FDM the Van Leer scheme seems to give the best results, that means little diffusion with no dispersion. For FEM the Galerkin finite element method with a Crank-Nicholson time discretization gives the best results, but with still unwanted dispersion. The latter solution method is chosen for implementation in VIp, a software package for moulding processes based on FEM.

The results show that particle tracking based on the conservation of identity is an attractive method. The Galerkin FEM needs some improvement as expected from the result of the test problems. Future research should be focused on that problem and also on the experimental validation of the calculations.

For a detailed description of the flow of a particle it is not only needed to use the right modeling strategy but also the right material data. Therefore in this report attention has been paid to the rheological characterization of two amorphous thermoplastics. The properties in shear of a polystyrene and a polycarbonate melt are measured using a rotational rheometer. Both linear and non-linear viscoelastic measurements are discussed. Finally the material data are fitted to three different constitutive models: a generalized Newtonian model, the Leonov model and the Wagner model.

Notation

Quantities

A, a	scalar
$\vec{a}$	vector
$\mathbf{A}$	second tensor
$\underset{\sim}{A}$, $\underset{\sim}{a}$	column
$\underline{\underline{A}}$	matrix
$\mathbf{I}$	second unit tensor

Operations and functions

$\mathbf{A}^c$	conjugation
$\vec{a} \cdot \vec{b}$, $\mathbf{A} \cdot \mathbf{B}$	inner product
$\mathbf{A} : \mathbf{B}$	double inner product
$\mathbf{A}^{-1}$, $\underline{\underline{A}}^{-1}$	inversion
$\|\vec{a}\|$, $\|\mathbf{A}\|$	norm
$I_1^{\mathbf{A}} \equiv tr(\mathbf{A})$	first invariant of a second order tensor, or trace
$I_2^{\mathbf{A}}$	second invariant of a second order tensor
$I_3^{\mathbf{A}} \equiv det(\mathbf{A})$	third invariant of a second order tensor, or determinant
$\mathbf{A}^d = \mathbf{A} - \frac{1}{3} tr(\mathbf{A})\,\mathbf{I}$	deviatoric part of a second order tensor
$\underset{\sim}{a}^T$, $\underline{\underline{A}}^T$	transposition
$\vec{\nabla}$	gradient operator
$\dot{a}$	material time derivative
$\frac{\partial a}{\partial t}$	spatial time derivative

Chapter 1

Introduction

The injection moulding process is a flexible production process for the fabrication of plastics parts. Characteristic for this process are the complex shaped, integrated products manufactured in large numbers with small cycle times. Nowadays there are a number of different injection moulding techniques available. Examples are: gas assisted-, foam-, thermoset-, (reinforced) reaction-, two-shot-, and multilayer injection moulding. In this report the attention will be focussed on the modeling of the multilayer injection moulding process.

For the sake of clearness a short description of the injection moulding machine and the process will be given. The injecton moulding machine consists of an injection and a clamping unit (Fig 1.1). The injection unit contains of a screw rotating in a heated barrel for plasticizing the granulated polymer fed by the hopper. When sufficient material is plasticized the screw acts as a piston and pushes the melt through a nozzle and runner system into the mould cavity. The clamping unit contains the two mould halfs and prevents the mould from opening by the high pressure that occurs during the process. The process can be divided in three stages: the injection, packing and holding, and the cooling stage. In the injection stage the molten polymer is forced into the mould. After complete filling of the cavity extra material will be injected to compensate for the shrinkage, the so-called packing and holding stage. From the moment the gate is frozen completely no more material can be added and the cooling stage begins. When the temperature is decreased below the ejection temperature the mould is opened and the product can be taken out for further cooling to the ambient temperature.

1.1 Multilayer injection moulding

In the multilayer injection moulding process, two or three polymer materials are sequentially or simultaneously injected in the mould to fabricate prod-

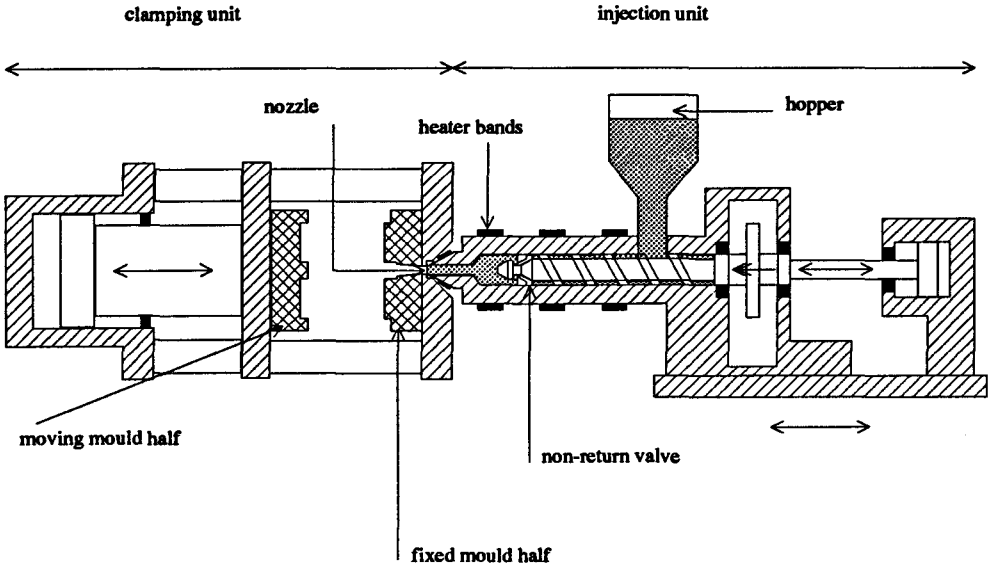

Figure 1.1: Injection moulding machine

ucts with a layered structure. The distribution of the layers in the product depends on the position of the gate, geometry of the injection nozzle and the method of injection (simultaneous and/or sequential). By changing the sequence of injection of two components A and B (A,B; A,B,A; A,B/A,A; A,A/B,A; etc.) the thickness and also the place (centric or excentric) of the layers can be controlled (see Fig. 1.2). The multilayer technology differs from the multi-shot injection technology, where a first shot after complete solidification is placed in a larger mould-cavity followed by the injection of a second shot against or around the previous shot.

The multilayer (or multicomponent, sandwich or co-) injection technique is first developed by ICI in 1967 ([19]). They were able to produce large, light-weigth, and stiff products. The sequential injection of two components (A,B; A,B,A) limited the practical applications to sandwich constructions with a three layered structure. The component B, the core layer, often consists of the A material with a physical or chemical foaming agent. In this way large parts with hard, flat, and glossy skin layers could be moulded without high clamping forces, since the shrinkage is compensated for by the expansion of the core material instead of packing at high pressures as in the convential injection moulding process. Applications of the thick-walled (> 4 mm) products can be found in the automotive, housing, and sanitary branches. In applications where thin-walled products are more suitable, light-weight, high-stiffnes products can be moulded more economically using ribs.

During the last years the multilayer injection moulding technology has

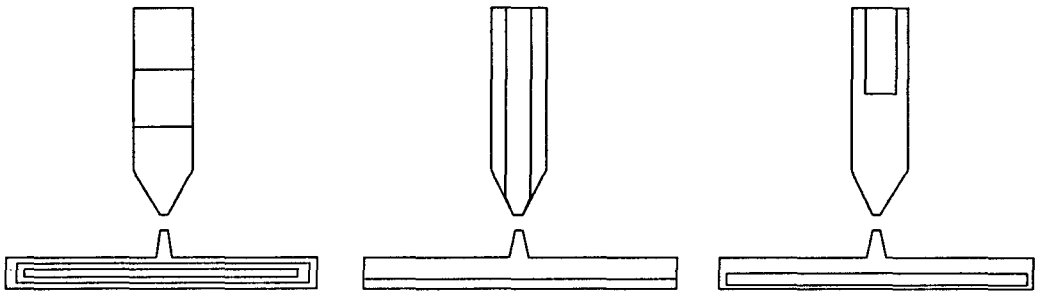

Figure 1.2: Schematic representation of two component injection moulding with sequential, simultaneous, and combined injection

been applied to thin-walled products using the Battenfeld two-channel technique (see Fig. 1.3) [17]. With this technique not only sequential injection is possible as in the ICI technique, but also simultaneous injection of two components (A,A/B,A; A,B/A,A). In this way, thin, excentric layers can be realized in a product to fabricate products consisting of three layers in one cycle. Until now this only could be achieved with the multi-shot method.

Some examples of applications are shielding against electro-magnetic interference of e.g. computer housings, where a Faraday-cage is created by a conductive layer inside the product, or in barrier products, where a thin layer of a material with a low permeability for gases is enclosed by outer layers that provide other desired properties of the product (like stiffness and appareance) combined with water resistency. In this way the advantage of the injection moulding process with his versatility in geometrical design of the products can be extended with the ability of combining different materials with their specific properties in one product. However, some limitations of the existing technology should be overcome. First the ability of injection of two components only has to be extended to three components. As in comparison with coextrusion techniques, where polar and apolar materials together with a third component as a glue (compatibilizer) are used to get attractive combinations in one product, these material combinations would make also the multilayer technique more competitive. This limitation is being removed by the development of a three component injection moulding machine at our laboratory based on the Battenfeld system. Secondly, the complexity of the products is limited to relatively simple geometries. To overcome this drawback, one must be able to predict the flow of every particle in the mould. For

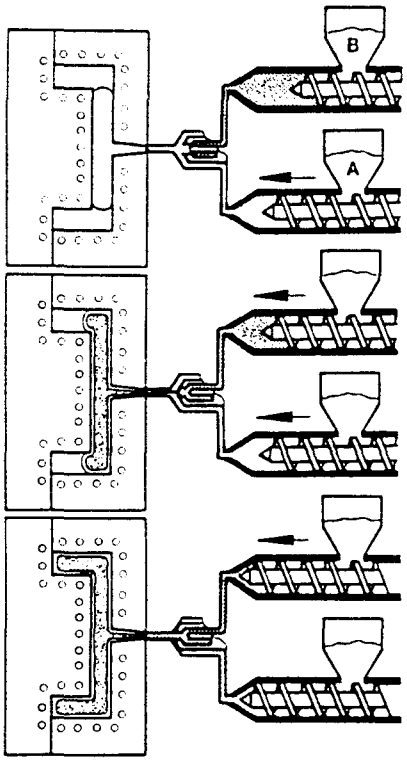

Figure 1.3: Principal of mould filling with the Battenfeld system

this purpose numerical tools have to be developed for calculating the flow path of particles. In that case it is also possible to predict what has to be injected given a desired layer distribution in a product. Only with such a tool a succesfull application of the multilayer technique for complex shaped products is possible.

1.2 Scope of the work

A flexible multilayer injection moulding technology together with numerical simulation tools for predicting the flow paths during mould filing should be developed. The injection technology will be realized in two steps. First an injection moulding machine will be equipped with a valve system capable of controlling the flow of the three components. Secondly a more flexible system will be constructed based on an accumulator between the distribution device and the mould as proposed by Vos et al. [61]. Besides the practical applications of the multilayer technique, this method will be used as a test of numerical models which describe the flow during the injection phase of the process. Within the modeling of the flow, the melt is considered as a generalized Newtonian fluid. Visco-elastic stresses are calculated by substitution of the calculated flow-field into a visco-elastic constitutive equation. This is

called the decoupled approach [15], i.e. the viscoelasticity of the material is supposed to have no significant influence on the flow kinematics. With the multilayer technique the total deformation history can be investigated experimentally and compared with the numerical calculations. In that way a validation of the decoupled approach will be accomplished. Viscoelastic stresses are important for predicting the influence of material properties and process conditions on product quality, especially for the use in precision injection moulding.

1.3 Outline

This report mainly deals with the mathematical modeling of the multilayer injection moulding process. In chapter 2 the basic equations will be given with special emphasis on the modeling of the particle tracking and the fountain flow phenomena. Input data is important in simulation of the injection moulding process. In chapter 3 the rheological characterization of two commercial amorphous polymers will be presented. The important model parameters will be calculated from the measured data. Chapter 4 deals with the solution of the problem of particle tracking. As well as finite difference methods as finite element solution methods will be discussed. Results of calculations will be given in chapter 5.

Chapter 2

Modeling the multilayer injection moulding process

Modeling the multilayer injection moulding process is almost identical with that for convential injection moulding. Therefore no detailed derivation of the equations will be given in this chapter. The reader is refered to literature: Douven [15], Isayev [22], Tucker [28], and Sitters [56].

In section 2.1 and 2.2 briefly the main balance and constitutive equations will be given. Section 2.3 deals with the problem of particle tracking. In the last section the fountain flow phenomena are discussed.

2.1 Fundamental equations

The full set of equations needed to describe the injection moulding process consists of the balance equations and the constitutive equations. First the balance equations will be given followed by the constitutive equations used in this report.

2.1.1 Balance equations

From the continuum mechanics, which main goal is the determination of the fields of density, temperature, and motion for the material points considered, the balance equations can be derived. These balance equations read in their local form as follows:

Balance of mass (continuity equation)

$$\dot{\rho} + \rho\vec{\nabla} \cdot \vec{v} = 0 \tag{2.1}$$

where ρ denotes the density, $\vec{v}$ the velocity vector, and $\vec{\nabla}$ the gradient operator.

Balance of momentum

$$\vec{\nabla} \cdot \boldsymbol{\sigma}^c + \rho \vec{f} = \rho \dot{\vec{v}} \tag{2.2}$$

with $\boldsymbol{\sigma}^c$ the Cauchy stress tensor, and $\vec{f}$ the specific body force.

Balance of moment of momentum

$$\boldsymbol{\sigma} = \boldsymbol{\sigma}^c \tag{2.3}$$

Balance of energy (first law of thermodynamics)

$$\rho \dot{e} = \boldsymbol{\sigma} : \mathbf{D} - \vec{\nabla} \cdot \vec{h} + \rho r \tag{2.4}$$

where e is the specific internal energy, $\mathbf{D}$ is the deformation rate tensor, $\vec{h}$ the heat flux vector, and r is the specific heat source.

2.1.2 Constitutive equations

The set of balance equations only can be solved if relations for $\boldsymbol{\sigma}$, $\vec{h}$ and e as function of density, temperature and motion are known. In this section the constitutive equations for the Cauchy stress tensor and the thermal properties will be given in their final form. For a more detailed description the reader will be referred to Douven, chapter 2 [15].

Cauchy stress tensor

There are many different constitutive models for relating the Cauchy stress tensor to the independent variables ρ, T and $\vec{x}$. Here, three different models will be discussed. First the generalized Newtonian fluid model will be described. This model is most commonly used in simulating the injection phase of the multilayer injection moulding process. It neglects all the viscoelastic effects of the polymers. The other two models, the compressible Leonov and the Wagner model, are capable of describing viscoelastic effects. The compressible Leonov model is a differential constitutive equation whereas the compressible Wagner equation is written in an integral form.

Generalized Newtonian fluid behaviour

Ignoring the elastic effects and assuming that $\boldsymbol{\sigma}^d$ is only a function of the shear rate, the material behaviour of a polymer melt can be presented by a compressible generalized Newtonian model. The equations read as follows:

$$\boldsymbol{\sigma} = -p\mathbf{I} + \boldsymbol{\sigma}^d \tag{2.5}$$

$$p = p_0 - \mu\, tr(\mathbf{D}), \qquad \boldsymbol{\sigma}^d = 2\eta \mathbf{D}^d \tag{2.6}$$

$$\mu = \mu(p_0, T, \dot{\rho}, I_2^{\mathbf{D}^d}), \qquad \eta = \eta(p_0, T, \dot{\rho}, I_2^{\mathbf{D}^d}) \tag{2.7}$$

with μ and η are the bulk and shear viscosity respectively, p the hydrostatic pressure, T the temperature, and $\mathbf{I}$ the unit tensor.

Compressible Leonov model

The compressible Leonov model is a viscoelastic differential constitutive equation that can be used for calculation of the flow-induced stresses that occur during injection of a viscoelastic fluid into the mould. For this purpose the original formulation by Leonov [39, 40] is extended to compressible fluids (Baaijens [1]). The model is given for the multi-mode case, because this representation has the best predictive quality.

$$\boldsymbol{\sigma} = -p\mathbf{I} + \boldsymbol{\sigma}_e^d + \boldsymbol{\sigma}_p \tag{2.8}$$

$$\boldsymbol{\sigma}_e^d = \sum_{i=1}^{m} \frac{\eta_i}{\theta_i} \bar{\mathbf{B}}_{ei}^d, \qquad \boldsymbol{\sigma}_p = 2\eta_r \mathbf{D}^d \tag{2.9}$$

$$\nu = \nu(p, T) \tag{2.10}$$

$$\mathbf{D}_{pi} = \frac{1}{4\theta_i}(\bar{\mathbf{B}}_{ei}^d - \bar{\mathbf{B}}_{ei}^{-d}) \tag{2.11}$$

$$\overset{\nabla}{\bar{\mathbf{B}}}_{ei} = (\mathbf{L}^d - \mathbf{D}_{pi}) \cdot \bar{\mathbf{B}}_{ei} + \bar{\mathbf{B}}_{ei} \cdot (\mathbf{L}^{dc} - \mathbf{D}_{pi}) \tag{2.12}$$

where η_i and θ_i are the viscosity and relaxation time of mode i respectively, η_r is the retardation viscosity, ν is the specific volume, $\mathbf{L}$ is the velocity gradient tensor, and $\mathbf{B}_e$ is the Finger tensor. The parameters η_i, θ_i and η_r can be determined by measuring the linear viscoelastic functions only ([41]) as will be shown in chapter 3 where also the temperature dependency of these parameters will be discussed.

Compressible Wagner model

The Wagner model (Wagner [63, 62]) is a special case of the K-BKZ model ([32, 5]). In this representation factorability, i.e time effects are separated from strain effects, is assumed (Larson [35]).

$$\boldsymbol{\sigma} = -p(\rho(t))\mathbf{I} + \int_{-\infty}^{t} M(t-\tau) h(\bar{\mathcal{I}}_1, \bar{\mathcal{I}}_2) \bar{\mathbf{C}}_t^{-d}(\tau)\, d\tau \tag{2.13}$$

$$\rho = \rho(p, T) \tag{2.14}$$

with t the time, M the memory function, h the damping function, $\mathbf{C}_t$ the relative deformation tensor and $\bar{\mathcal{I}}_1, \bar{\mathcal{I}}_2$ invariants of $\mathbf{C}_t$. The memory function M can be obtained by measuring the linear viscoelastic functions. For determination of the damping function h, measurements in the non-linear regime have to be carried out. There are various ways of expressing the damping function h. Wagner *et al.* [65] choose

$$h(\bar{\mathcal{I}}_1, \bar{\mathcal{I}}_2) = m e^{-n_1\sqrt{I-3}} + (1-m) e^{-n_2\sqrt{I-3}} \tag{2.15}$$

$$I = \alpha \bar{I}_1 + (1-\alpha)\bar{I}_2$$

where Papanastasiou *et al.* [46] propose

$$h(\bar{I}_1, \bar{I}_2) = \frac{1}{1+\beta(I-3)} \tag{2.16}$$

The memory function can be expressed with a continuous relaxation time spectrum $H(\theta)$

$$M(t-\tau, T) = \int_{-\infty}^{\infty} \frac{H(\theta)}{\theta} e^{-(t-\tau)/\theta} d\ln\theta \tag{2.17}$$

where the relaxation time θ depends on the temperature. When H is represented as a discrete relaxation time spectrum

$$H(\theta) = \sum_{i=1}^{m} G_i \theta_i \delta(\theta - \theta_i) \tag{2.18}$$

with δ the Dirac delta function and G_i the relaxation shear modulus of mode i, the memory function reads:

$$M(t-\tau, T) = \sum_{i=1}^{m} \frac{G_i}{\theta_i} e^{-(t-\tau)/\theta_i} \tag{2.19}$$

Thermal properties

The constitutive equations for the thermal behaviour are Fourier's law for the heat flux vector and an equation for the internal energy. Fourier's law reads:

$$\vec{h} = -\boldsymbol{\lambda} \cdot \vec{\nabla} T \tag{2.20}$$

with $\boldsymbol{\lambda}$ the thermal conductivity tensor. The specific internal energy e can be written as (Bird [7], Sitters [56])

$$\dot{e} = c_p \dot{T} + \frac{p_o}{\rho^2}\dot{\rho} + \frac{T}{\rho^2}\left(\frac{\partial \rho}{\partial T}\right)_{p_0} \dot{p}_0 \tag{2.21}$$

$$c_p = c_p(p_0, T) = \left(\frac{\partial g}{\partial T}\right)_{p_0}$$

where c_p is the thermal capacity at constant hydrostatic pressure and $g = e + p_0/\rho$ is the specific enthalpy. It must be noted that equation (2.21) is derived under assumption that the elasticity has a neglible contribution to the mechanical dissipation.

2.2 Thin film approximation

The geometry of injection moulded products gives the opportunity to simplify the equations considerably. In the most practical applications the thickness of a injection moulded product is small (0.5–4 mm) compared with the other dimensions. The cavities consist of narrow, weakly curved channels, and therefore the thin film approximation can be employed (Hieber and Shen [23], Sitters [56], Boshouwers and van der Werf [9], Douven [15]).

A local Cartesian vector base $O_\epsilon : \{\vec{\epsilon}_1, \vec{\epsilon}_2, \vec{\epsilon}_3\}$ can be defined in every point of the midplane of the mould. Where the vector $\vec{\epsilon}_3$ is normal with respect to the midplane. An arbitrary vector $\vec{a}$ can be decomposed in a vector $\vec{a}^*$ parallel to the midplane and a component in the direction of $\vec{\epsilon}_3$

$$\vec{a} = a_i^\epsilon \vec{\epsilon}_i = \vec{a}^* + a_3^\epsilon \vec{\epsilon}_3 \tag{2.22}$$

Because of the high viscosity of a polymer melt the Reynolds number (ratio of viscous forces and the inertial forces) is small and therefore the inertial and body forces in the momentum equation (2.2) may be neglected. The main consequences of the approximation are that

- the pressure is independent of the $\vec{\epsilon}_3$ direction
- the velocity gradients parallel to the midplane are small compared with those in the $\vec{\epsilon}_3$ direction
- the velocity components in the $\vec{\epsilon}_3$ direction are small compared with the components tangent to the midplane
- the thermal conduction parallel to the midplane may be neglected with respect to conduction in the $\vec{\epsilon}_3$ direction

As a consequence the shear rate $\dot{\gamma} = \sqrt{2\mathbf{D}^d : \mathbf{D}^d}$ reduces to $\left| \frac{\partial \vec{v}^*}{\partial x_3^\epsilon} \right|$. Finally the term in equation 2.6 containing the bulk viscosity μ is neglected, which implies that the thermodynamic pressures is equal to the hydrostatic pressure. With these simplifications the set of equations for a generalized Newtonian fluid read as

$$\vec{\nabla}^* \cdot \vec{v}^* + \frac{\partial v_3^\epsilon}{\partial x_3^\epsilon} = -\frac{\dot{\rho}}{\rho} \tag{2.23}$$

$$\vec{\nabla}^* p = \frac{\partial}{\partial x_3^\epsilon}\left(\eta \frac{\partial \vec{v}^*}{\partial x_3^\epsilon}\right), \qquad \frac{\partial p}{\partial x_3^\epsilon} = 0, \tag{2.24}$$

$$\rho c_p \dot{T} = \frac{\partial}{\partial x_3^\epsilon}\left(\lambda \frac{\partial \vec{T}}{\partial x_3^\epsilon}\right) + \eta\dot{\gamma}^2 - \frac{T}{\rho}\left(\frac{\partial \rho}{T}\right)_p \dot{p} \tag{2.25}$$

This set of equations is instationary, non-linear and coupled because the viscosity and density are both temperature and pressure dependent.

The pressure field is solved numerically by the Galerkin finite element method in the midplane of the cavity. The temperature and the velocity fields

are solved by the finite difference method in the full domain of the cavity. Therefore the thin film approximation often is called the $2\frac{1}{2}$D approach. Further details regarding to the numerical solution of this problem can be found in Douven, chapter 4 ([15]).

2.3 Particle tracking

In simulating the multilayer injection moulding process it is needed to known where and when a material particle has to be injected to end up at the desired position in the product. A way of particle tracking is to follow a certain particle during the flow by constructing its flow path ℓ. Given a particle φ at the position $\vec{x}_0$ at time t_0 its flow path ℓ can be expressed as:

$$\ell : \vec{x}(\vec{x}_f, t_f; t) \qquad \forall t \in [t_0, t_f] \tag{2.26}$$

$$\text{with} \qquad \vec{x}(\vec{x}_0, t_0; t_0) = \vec{x}_0 \tag{2.27}$$

Because the velocity vector $\vec{v}(\vec{x}, t)$ is tangent to ℓ, the flow path can be constructed by integrating

$$\frac{\mathrm{d}\vec{x}}{\mathrm{d}t} = \vec{v}(\vec{x}, t) \tag{2.28}$$

with equation (2.27) as initial condition. This initial value problem can be adequately solved by a Runga-Kutta integration method (Caspers [11]). A disadvantage of this method is that for every time step the velocity field must be stored. This requires a large storage capacity.

Another method of particle tracking is to give particles when they enter the mould a set of labels $\underset{\sim}{\xi}$, representing their 'identity' ([47, 48, 67]). During the flow in the mould the identity of each particle does not change. For that reason the conservation of identity can be expressed by

$$\dot{\underset{\sim}{\xi}} = \frac{\mathrm{D}\underset{\sim}{\xi}}{\mathrm{D}t} = \underset{\sim}{0} \text{ in } \Gamma_m, \qquad \underset{\sim}{\xi}(\vec{x}, t) = \underset{\sim}{\mathrm{f}}(\vec{x}, t) \text{ on } \Gamma_e \tag{2.29}$$

where $\underset{\sim}{\xi}$ is for instance a column containing the starting position and time (x_0, y_0, z_0, t_0), or the colour and viscosity. The problem of particle tracking can be solved with either a Lagrangian or an Eulerian approach.

Lagrangian approach

The path of every particle can be determined under consideration that:

$$\vec{x} = \vec{x}(\vec{x}_0, t), \qquad \vec{x}(\vec{x}_0, t_0) = \vec{x}_0 \tag{2.30}$$

From equation 2.30 it may be clear that $\underset{\sim}{\xi}(\vec{x}, t) = \underset{\sim}{\xi}(\vec{x}_0, t_0)$.

Eulerian approach

In a fixed frame of reference the conservation of identity can be expressed as:

$$\frac{\partial \underset{\sim}{\xi}}{\partial t} + \vec{v} \cdot \vec{\nabla} \underset{\sim}{\xi} = \underset{\sim}{0} \tag{2.31}$$

In this representation the change of label values in space is calculated instead of tracking particles. The actual tracking can be carried out by determining the positons of a given set of labels in time. For the use in multilayer injection moulding, the label values at the end of filling give information where and when every particle has entered the mould. By pointing out specific layers in the product, only the label values of the particles in these layers have to be determined to know what configuration must be injected to get the desired multilayer product. The main advantage of the method of conservation of identity is that the storage capacity required is much smaller than for the path construction method because only the label values at one time (end of filling) must be stored. Moreoever, using the Eulerian approach the followed path of the particles is not important. Numerical experiments have showed that the Eulerian approach turned out to be the most flexible and efficient in use ([11, 58]).

It must be noted that both methods only give the desired result, i.e. the prediction of the injection sequence for a desired configuration of the layers, if the material properties of the injected materials are the same. Because the material properties affect the velocity field, only the injected sequence of materials can be traced back. All other configurations will lead to wrong results. However, this result can be used as a start condition in an iteration loop. Such a iteration process proceeds as follows:

1. Simulate the injection with one material.
2. Point out the desired configuration and determine the injection sequence.
3. Use this sequence for the simulation of the injection with the different components.
4. Point out the desired configuration, etc.
5. Repeat step 3 and 4 until the injected and calculated configuration correspond to a sufficient degree.

2.4 Fountain flow phenomena

During the filling of a mould cavity two flow regimes can be recognized: the main flow and a front flow. In the front flow a specific flow pattern behind the advancing free surface has been observed experimentally. Tracer studies gave detailed information of the deformation of the fluid when it passes the front region (Coyle *et al.* [14], Cogos *et al.* [21], and Schmidt [53]). These observations showed that a fluid particle that enters the front flow

first decelerates in the direction of the flow and obtains at the same time a velocity component in the direction normal to the flow thus spilling the material outwards to the mould walls (figure 2.1). This phenomena, known

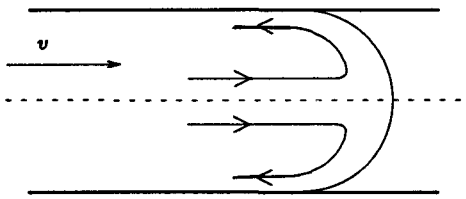

Figure 2.1: Fountain flow phenomena

as the *fountain effect* (Rose [52]), has an important effect on the particle distribution in a moulded product especially for all material elements close to the mould walls. Local breakthrough of core layers to the outside of the product is completely controlled by the fountain region and mostly undesired, although some applications just ask for a specific material at the outside of the product (colour, gloss, UV stability, soft touch, etc.). Therefore it is important to incorporate the fountain flow effects in the modeling of the multilayer injection moulding process.

The studies dealing with the modeling of the fountain flow can be divided in those who describe an interface between two liquids or those describing a free front advancing in a capillary tube or in between plates. Bhattacharji and Savic [6] made the first attempt to give an semi-analytical solution of the Navier-Stokes equations for the liquid/liquid interface. Numerical solutions were obtained using the Marker-and-Cell technique (Cogos *et al.* [21] and Kamal *et al.* [30, 31, 34]), or finite element methods (Behrens *et al.* [4], Coyle *et al.* [14], and Mavridis and coworkers [43, 44]). Dupret and Vanderschuren [16], Manas-Zlowzower *et al.* [42] Sitters [56] proposed a simple model that can be used well in combination with the thin-film approximation. In this model the fountain flow is idealized by a single straight line moving with the average front velocity $\bar{v}_s$ (see figure. 2.2). These models, defined in two dimensions, can be used for the three dimensional flow in a mould by assuming that the pressure gradient tangent to the front $\left(\frac{\partial p}{\partial t}\right)$ can be neglected. In the front region a curved x-s plane can be constructed in the direction normal to the front (figure 2.3) where such a 2D front model can be applied.

Depicting the fountain flow in the Lagrangian framework with the mould wall moving with $-\bar{v}_s$, the front flow can be divided in two parts (figure 2.4): a high-velocity region $0 < z < z_f$ and a low-velocity region $z_f < z < H/2$, where z_f is the position where $v_s(z) = \bar{v}_s$. According to the balance of mass

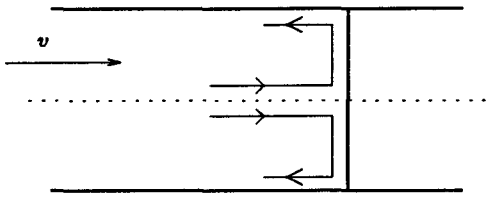

Figure 2.2: Simplified front model in injection moulding

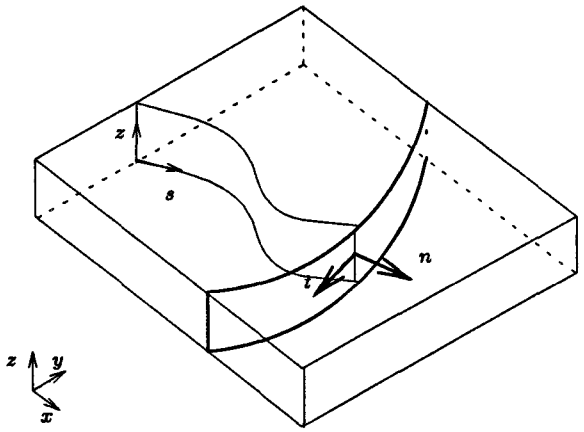

Figure 2.3: Fountain flow model in injection moulding

(assuming an incompressible fluid), the relation between the inflow z_i and the outflow position z_o can be expressed by:

$$\int_{z_i}^{z_f} (v_s(z') - \bar{v}_s)\, dz' = \int_{z_f}^{z_o} (\bar{v}_s - v_s(z'))\, dz' \tag{2.32}$$

In the case of a Newtonian fluid it can be derived easily that $z_f = 1/\sqrt{3}H/2$ and that $z_o^3 - z_o + z_i - z_i^3 = 0$. With this simple model an estimation can be made of the gapwise distribution of some quantities if it is assumed that the properties of a particle are not influenced by the fountain flow. For some applications, however, the residence time in the fountain flow is of importance. For example in the case of multilayer or in reactive injection moulding. Therefore this model has to be adapted.

The semi-analytical model of Bhattacharji and Savic gives the opportunity to derive relatively easy a relation between the residence time in the front flow and the inflow or outflow position ([58]). With the known velocity field (see Appendix A) the flow paths can be constructed (Fig 2.5).

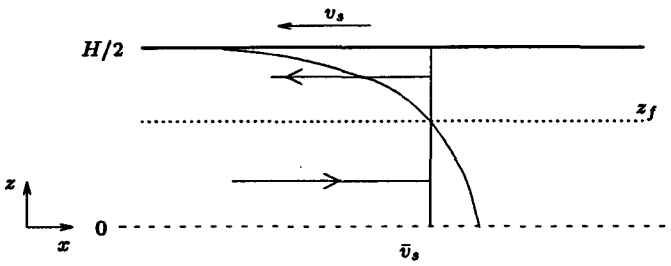

Figure 2.4: Lagrangian representation of simplified front model (only one mould half is considered)

Integrating along a flow-path, corresponding with an certain inflow position

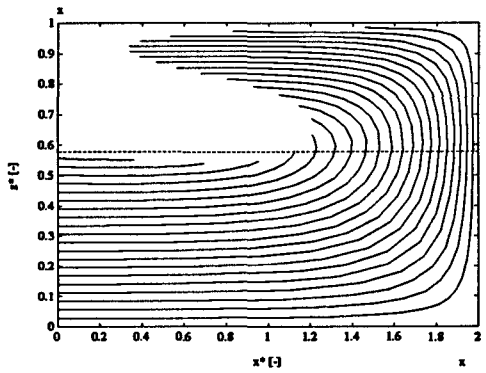

Figure 2.5: Flow paths in the fountain region for a certain time interval

until a particle re-enters the main flow, gives the residence time. The residence time and inflow position both as function of the outflow position are plotted in figure 2.6. This representation can be parametrized by fitting the curves with a polynomial. In this way not much extra computing effort is required for incorporating a front model.

2.5 Conclusion

The balance and constitutive equations given in this chapter can be applied for simulating the 'normal' as well as the multilayer injection moulding process. In the latter case, an extra conservation law is added for solving the particle tracking problem. In the next chapter, the aspects of the numerical solution of the particle tracking problem, are discussed.

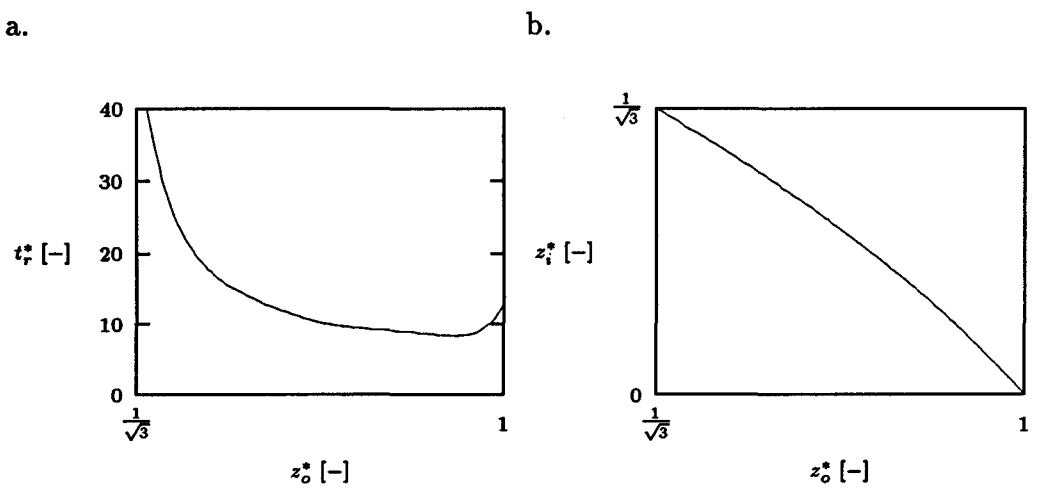

Figure 2.6: Residence time t_r (a) and inflow position z_i (b) in front region as function of outflow position z_o

Chapter 3

Rheological characterization

In describing the flow in the mould the material behaviour of the molten polymer plays an important role. This chapter deals with the determination of the rheological properties of two amorphous polymers, a polystyrene (PS, Styron 678E from DOW Chemical) and a polycarbonate (PC, Makrolon CD 2000 from Bayer) in shear flow.

3.1 Viscoelastic measurements

The experiments for determining the properties of a viscoelastic fluid in shear can be divided in measurements in the linear and the non-linear viscoelastic regime. The linear properties are often determined by oscillatory shear experiments, while the non-linear properties can be determined by transient measurements.

3.1.1 Oscillatory shear experiments

The linear viscoelastic properties are measured by small amplitude (i.e in the linear viscoelastic regime) oscillatory shear experiments. They were carried out on a Rheometrics Dynamic Spectrometer RDS-II. For the measurements a circular shaped specimen is placed between two parallel disk and heated above T_g. By imposing a sinusoidal shear strain on the sample the respons can be measured. The shear strain is of the form

$$\gamma(t) = \gamma_0 \cos(\omega t) = \gamma_0 \Re(e^{i\omega t}) \tag{3.1}$$

where γ_0 is the shear strain amplitude and ω is the angular frequency. In the linear viscoelastic regime the shear stess τ_{12} will be sinusoidal with frequency ω, but with a different amplitude and out of phase with the strain input.

$$\tau_{12}(t) = \gamma_0 \Re(G^* e^{i\omega t}) = \gamma_0 G_d \Re(e^{i(\omega t+\delta)}) \tag{3.2}$$

This equation can also be expressed as:

$$\tau_{12}(t) = \gamma_0 G' \sin \omega t + \gamma_0 G'' \cos \omega t \tag{3.3}$$

with G' the storage modulus and G'' the loss modulus as the real and imaginary parts of the complex shear modulus G^* respectively. The dynamic shear modulus G_d and the loss angle δ are defined as

$$G_d = \sqrt{G'^2 + G''^2} \qquad \tan \delta = \frac{G'}{G''} \tag{3.4}$$

Besides the complex shear modulus, a complex viscosity can be defined:

$$\eta^* = \frac{-i}{\omega} G^* = \eta' - i\eta'' \tag{3.5}$$

with $\eta' = \frac{G''}{\omega}$ and $\eta'' = \frac{G'}{\omega}$.

The temperature dependency of the shear moduli and the viscosity can be modeled by assuming that the material is *thermorheologically simple.* For such a material it is observed that a set of isothermal curves (for instance G_d as function of ω) can be shifted onto a mastercurve by a shift along the logarithmic time or frequency axis. The shift depends on the temperature difference between the mastercurve and the shifted curve. The mastercurve constructed, spreads over several decades in time or frequency while the measurements are carried out within a limited time or frequency range. Besides the horizontal shift, also a small vertical shift of the curves, due to density changes with temperature, has to be applied. The mastercurves can be described by:

$$G_d(\omega a_T, T_0) = b_T G_d(\omega, T) \tag{3.6}$$

$$\delta(\omega a_T, T_0) = \delta(\omega, T) \tag{3.7}$$

where T_0 is the reference temperature corresponding with the temperature of the mastercurve and $a_T = a(T, T_0)$, $b_T = b(T, T_0)$ are the horizontal and vertical shift factors respectively. The horizontal shift factor for amorphous polymers can be described well with the so called WLF-equation. Williams, Landel and Ferry [66] found that for amorphous materials, in the range from the glass transition temperature T_g to about $T_g + 100$K, the shift function can be modeled by

$$\log a_T = -\frac{c_1(T - T_0)}{c_2 + T + T_0} \tag{3.8}$$

where c_1, c_2 are material constants. The vertical shift factor is often modeled by a temperature-density correction

$$b_T = \frac{\rho T_0}{\rho T} \tag{3.9}$$

The construction of the mastercurve proceeds as follows: first shift the loss angle δ horizontally along the frequency axis onto a mastercurve. Then apply the so obtained shift to the dynamic modulus G_d and shift these curves vertically onto the mastercurve. Only in this way, both shift factors can be determined seperately (Leblans [38]). The results of this procedure can be found in the figures 3.1 to 3.3 for the PS melt and in the figures 3.4 to 3.6 for the PC melt. The WLF-parameters are listed in table 3.1. From figure 3.3b it can concluded that the temperature density correction for PS cannot describe the vertical shift factors.

	PS Styron 678E	PC Makrolon CD2000
c_1	4.54	3.05
c_2 K	150.36	134.72
T_0 K	462	511

Table 3.1: WLF parameters

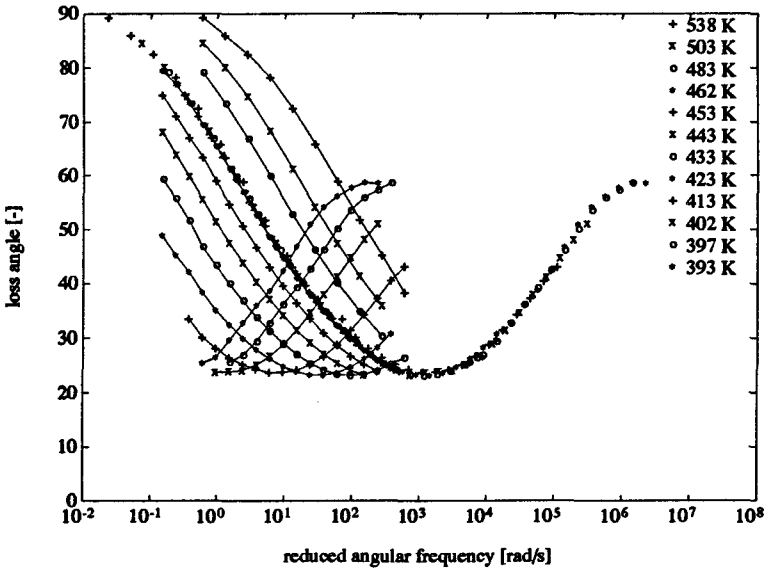

Figure 3.1: Loss angle as a function of angular frequency at various temperatures for PS Styron 678E. $T_0 = 462$K.

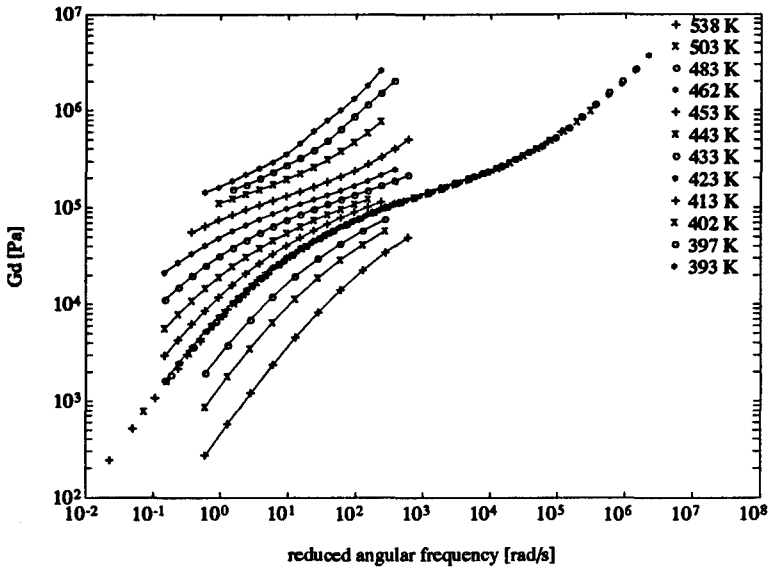

Figure 3.2: Dynamic modulus as a function of angular frequency at various temperatures for PS Styron 678E. $T_0 = 462$K.

a. b.

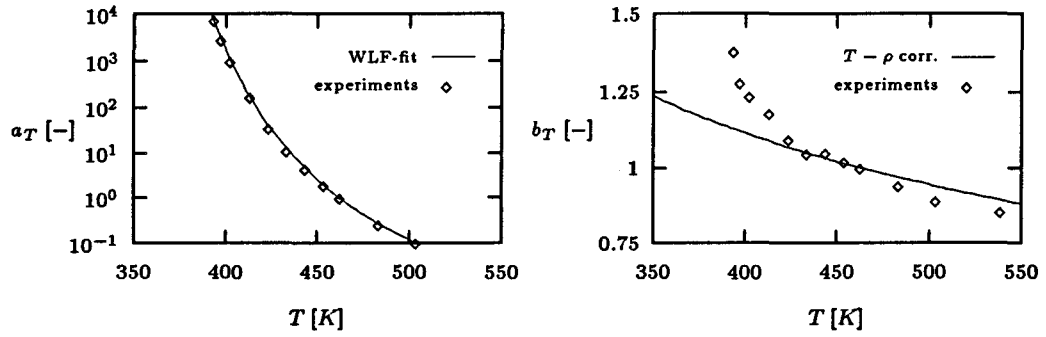

Figure 3.3: Horizontal shift a_T and vertical shift b_T against temperature for PS Styron 678E

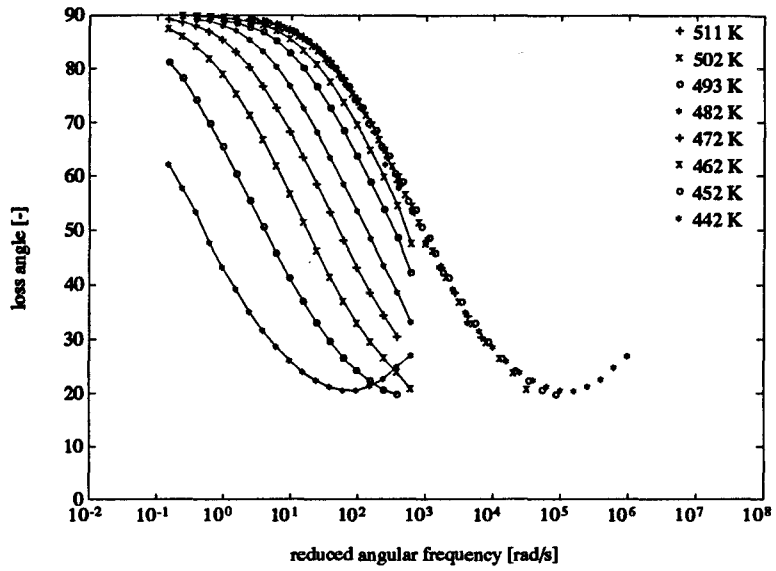

Figure 3.4: Loss angle as a function of angular frequency at various temperatures for PC Makrolon CD2000. $T_0 = 511$K.

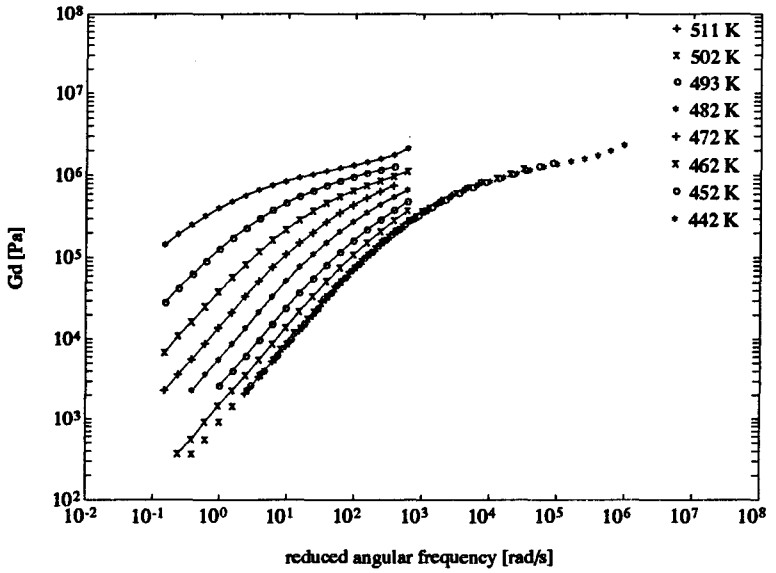

Figure 3.5: Dynamic modulus as a function of angular frequency at various temperatures for PC Makrolon CD2000. $T_0 = 511$K.

a. b.

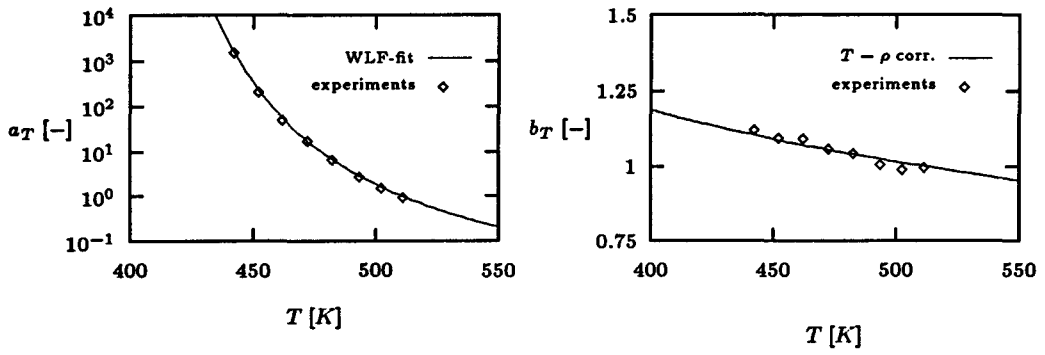

Figure 3.6: Horizontal shift a_T vertical shift b_T against temperature for PC Makrolon CD2000

3.1.2 Non-linear shear flow experiments

The non-linear shear flow behaviour is measured by means of three types of experiments:

- step strain stress relaxation
- stress growth at constant shear rate
- stress relaxation after cessation of steady shearing flow

With the results of these tests the damping function in the Wagner model can be determined. Moreover, they can be used for testing the predictive quality of the viscoelastic constitutive models obtained. The non-linear shear flow behaviour can be described by the transient shear viscosity η, the transient first normal stress coefficient ψ_1, and the relaxation modulus G, defined as

$$\eta^{+,-}(t,\dot{\gamma}_0) = \frac{\tau_{12}(t)}{\dot{\gamma}_0} \tag{3.10}$$

$$\psi_1^{+,-}(t,\dot{\gamma}_0) = \frac{\tau_{11}(t) - \tau_{22}(t)}{\dot{\gamma}_0^2} \tag{3.11}$$

$$G(t,\gamma_0) = \frac{\tau_{12}(t)}{\gamma_0} \tag{3.12}$$

where the superscript denotes that the property is measured in a start-up shear (+) or in a relaxation after steady shear flow experiment (-) respectively.

The experiments are carried out on a Rheometrics Dynamic Spectrometer RDS-II and on a Rheometrics Mechanical Spectrometer RMS-800 (at DSM Research) using a plate-cone geometry. With the latter apparatus, it is possible to measure the first normal stress difference ass well. It proved

to be impossible to measure the non-linear properties accurate enough for PC with the available apparatus ([55]). Therefore only results for the PS samples are given.

Step strain stress relaxation

In a step strain stress relaxation experiment a shear strain γ_0 is imposed upon a relaxed fluid. The strain history is given by

$$\gamma(t,t') = \begin{cases} 0 & \text{for } t-t' < t \\ \dot{\gamma}_0 \cdot (t-t') - \dot{\gamma}_0 t & \text{for } t \leq t-t' < t+\Delta t \\ \gamma_0 = \dot{\gamma}_0 \Delta t & \text{for } t-t' \geq t+\Delta t \end{cases} \tag{3.13}$$

where Δt is the finite time needed for imposing the shear strain γ_0 on the sample. Figure 3.7 shows the measured shear relaxation modulus for $\gamma_0 = 0.5, 1, 2, 3, 4$, and 5 at a reference temperature of $T_0 = 462$K with $\Delta t = 0.06s$. The maximum γ_0 is limited to a value of 5 to avoid overload of the torque transducer of the apparatus.

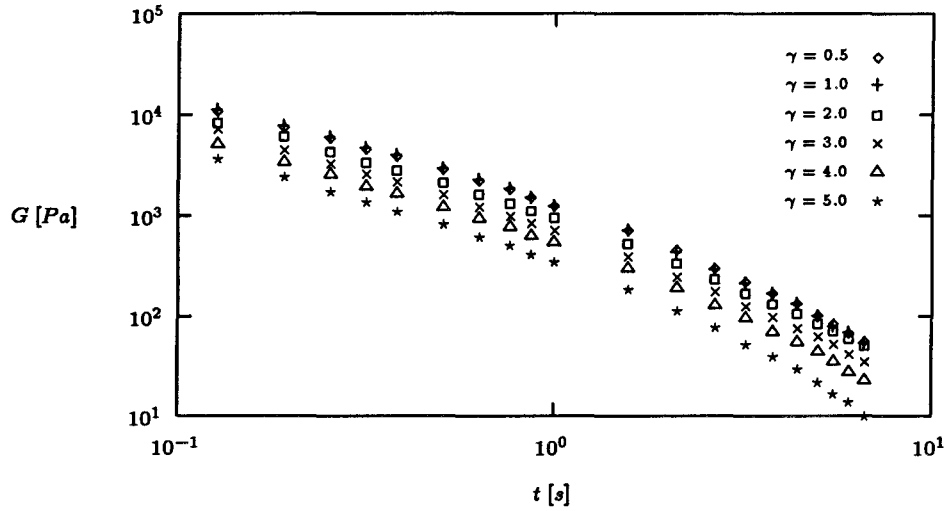

Figure 3.7: Shear relaxation modulus for $\gamma_0 = 0.5, 1, 2, 3, 4$, and 5 for PS Styron 678E at $T = 462$K.

Stress growth at constant shear rate

By applying a constant shear rate $\dot{\gamma}_0$ on a sample, the strain as a function of time is defined by:

$$\gamma(t,t') = \begin{cases} \dot{\gamma}_0 \cdot (t-t') & \text{for } t-t' < t \\ \dot{\gamma}_0 t & \text{for } t-t' \geq t \end{cases} \tag{3.14}$$

The transient viscosity η^+ and the transient primary normal stress coefficient ψ_1^+ are measured at $T = 462K$ for the shear rates: $\dot{\gamma}_0 = 0.2, 0.4, 1, 2$, and $4s^{-1}$. The maximum shear strain value was $\gamma = 20$ for all shear rates. The results are given in figure 3.8 and figure 3.9.

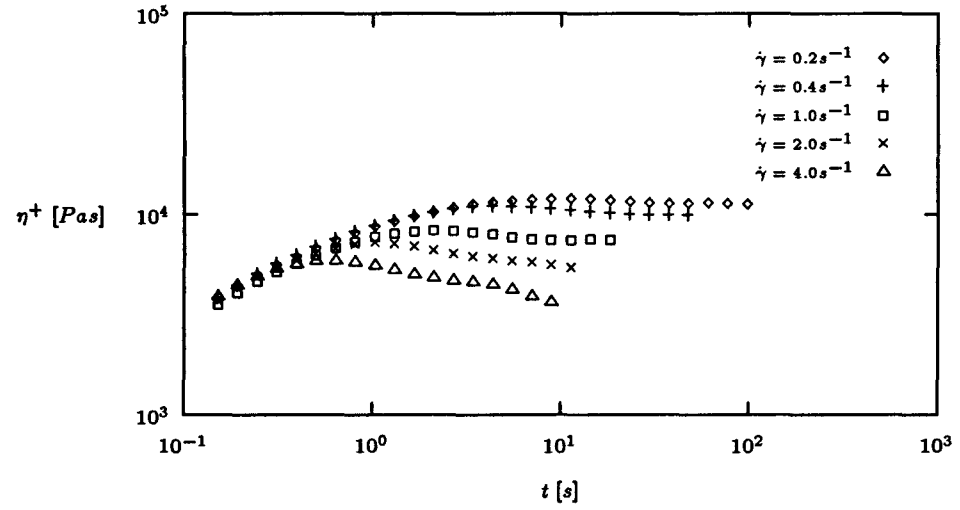

Figure 3.8: Transient shear viscosity for a start-up flow at constant shear rates of $\dot{\gamma}_0 = 0.2, 0.4, 1, 2$, and $4s^{-1}$ for PS Styron 678E at $T = 462$K.

Stress relaxation after cessation of steady shearing flow

When a constant shear rate experiment is continued long enough, the stresses will reach steady-state values. After cessation of the stationary flow the stresses will decay to zero. Neglecting the time of the sudden stoppage, the shear history can be expressed as:

$$\gamma(t,t') = \begin{cases} 0 & \text{for } t-t' < t \\ \dot{\gamma}_0 \cdot (t-t') - \dot{\gamma}_0 t & \text{for } t-t' \geq t \end{cases} \tag{3.15}$$

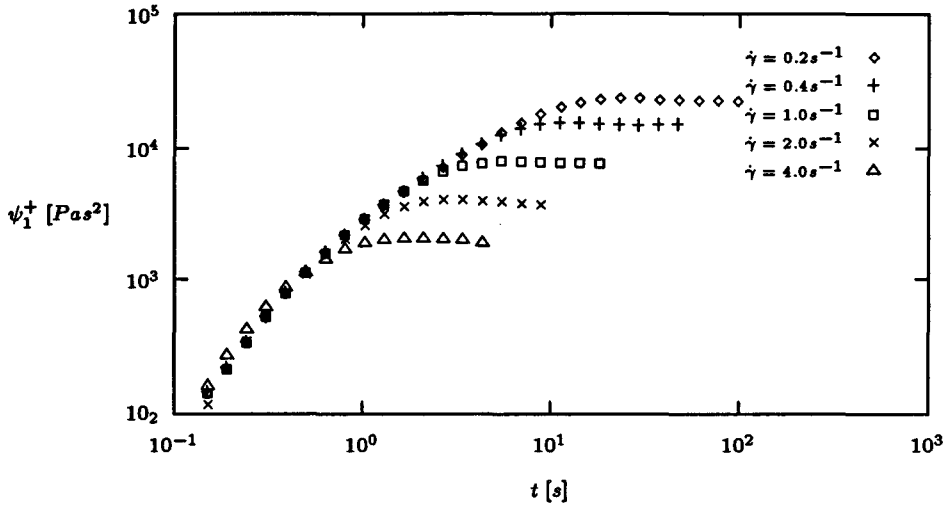

Figure 3.9: Transient primary normal stress coefficient for a start-up flow at constant shear rates of $\dot{\gamma}_0 = 0.2, 0.4, 1, 2$, and $4s^{-1}$ at for PS Styron 678E $T = 462$K.

Again the transient viscosity η^- and the transient primary normal stress coefficient ψ_1^- are measured at $T = 462$K for the shear rates of $\dot{\gamma}_0 = 0.2, 0.4, 1, 2$, and $4s^{-1}$. The results are shown in figure 3.10 and figure 3.11.

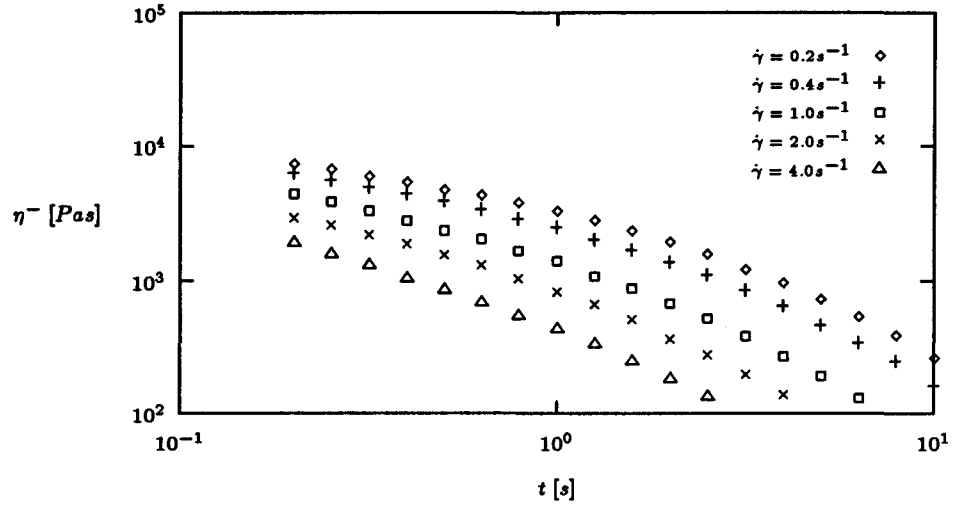

Figure 3.10: Transient shear viscosity after cessation of steady flow at shear rates of $\dot{\gamma}_0 = 0.2, 0.4, 1, 2$, and $4s^{-1}$ for PS Styron 678E at $T = 462$K.

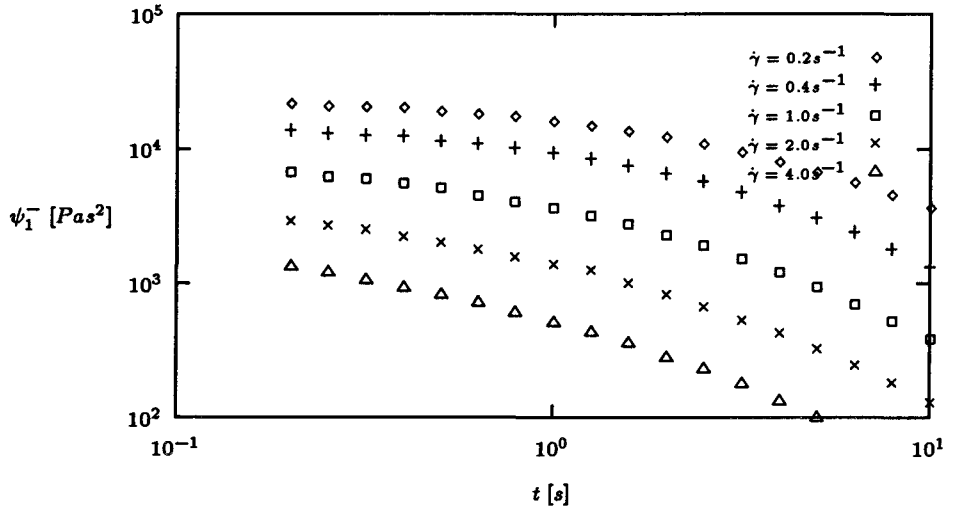

Figure 3.11: Transient primary normal stress coefficient after cessation of steady flow at shear rates of $\dot{\gamma}_0 = 0.2, 0.4, 1, 2$, and $4s^{-1}$ for PS Styron 678E at $T = 462$K.

3.2 Determination of the model parameters

In order to use viscoelastic models to calculate the material behaviour in various types of deformations like e.g. injection moulding, it is necessary that the model parameters are available. For the models described in Section 2.1.2 this implies the determination of the relaxation spectrum and the damping parameters.

3.2.1 Relaxation spectrum

In the linear viscoelastic regime, the relation between deformation and stress can be described by the Boltzmann superposition principle, which is given by:

$$\tau_{12}(t) = \int_{-\infty}^{t} G(t-t')\dot{\gamma}(t')\,dt' \tag{3.16}$$

where $G(t)$ is the linear shear relaxation modulus. In using any of the models available, an explicit mathematical function of the modulus is needed. Often the function of a generalized Maxwell model is used:

$$G(t-t') = \sum_{i=1}^{N} G_i e^{-\frac{t-t'}{\theta_i}} \tag{3.17}$$

in which G_i the shear modulus and θ_i the relaxation time corresponding to the i-th relaxation mode. For the use of this representation, N pairs of values (G_i, θ_i) have to determined from the experimental data.

Some authors ([38, 54]) prefer a continuous relaxation spectrum instead of a discrete one. Then the expression for the relaxation modulus reads:

$$G(t-t') = \int_{-\infty}^{\infty} H(\tau)e^{-\frac{t-t'}{\tau}}\,d\ln\tau \tag{3.18}$$

in which the relaxation time τ spreads out over several decades in time.

The experiments most used in determining relaxation spectra are the small amplitude oscillatory shear experiments. In the following, the measured data presented in Section 3.1.1 will be used to fit the relaxation spectra.

Continuous relaxation spectrum

Using a continuous relaxation spectrum the expressions for G' and G'' for a certain frequency ω_j read:

$$G'(\omega_j) = \int_{-\infty}^{\infty} H(\tau)\frac{(\omega_j\tau)^2}{1+(\omega_j\tau)^2}\,d\ln\tau \tag{3.19}$$

$$G''(\omega_j) = \int_{-\infty}^{\infty} H(\tau) \frac{\omega_j \tau}{1 + (\omega_j \tau)^2} \, d\ln\tau \tag{3.20}$$

In practice, the upper and lower limits of the integral are replaced by $\ln \tau_{max}$ and $\ln \tau_{min}$ respectively.

For the determination of $H(\tau)$ from the discrete oscillatory shear data, several approximate relations are available (see [8, 18]), e.g.

$$H(\tau) = \frac{2}{\pi} [G'']_{\omega=1/\tau} \tag{3.21}$$

or

$$H(\tau) = \frac{1}{2} [G_d \sin(2\delta)]_{\omega=1/\tau} \tag{3.22}$$

The spectrum obtained via this approximation is first extrapolated linear at both ends over at least two decades in time. Accordingly $H(\tau)$ can be optimized iteratively so that the experimental mastercurves of the storage and loss moduli can be described over the whole frequency range within experimental error ([29, 38, 54]). The iteration procedure can be summarized by:

1. calculate $H(\tau)$ with (3.22).
2. calculate $\hat{G}'$ and $\hat{G}''$ with the equations (3.19) and (3.20)
3. calculate $\Delta G' = G' - \hat{G}'$ and $\Delta G'' = G'' - \hat{G}''$.
4. if $\Delta G'/G', \Delta G''/G'' \leq \sigma$ then go to 6, else go to 5.
5. calculate $\Delta H = \frac{2}{\pi} \Delta G''$, update the trial solution $H \leftarrow H + \Delta H$, and go to 2.
6. stop the iteration procedure.

where σ is the relative error of the input data. The results of this procedure for PS and PC are shown in figure (3.12) and (3.13) respectively. For PC, the calculated moduli deviate from the measured ones at both ends of the frequency window. In this case, the spectrum can be adjusted by hand to fit the experimental data correctly. Then, it can be shown that the dip in the spectrum at the lefthand side vanishes.

Although for the use of a spectrum as a material property the continuous representation gives the most information, in viscoelastic calculations the discrete spectrum is far more practical. In this case only a limited number of relaxation modes have to be calculated repeatedly, rather than evaluating an integral over several decades in time.

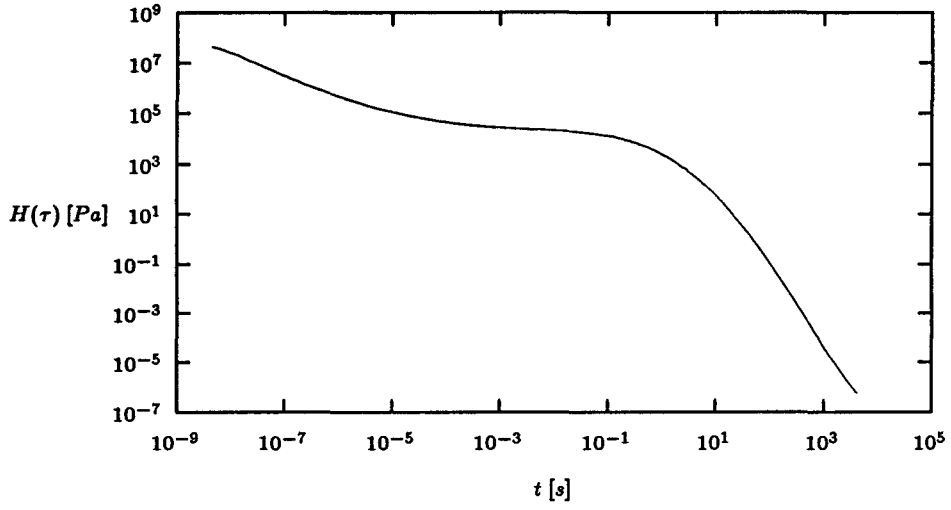

Figure 3.12: Continuous relaxation spectrum for PS Styron 678E at $T = 462$K

Discrete relaxation spectrum

Using a discrete relaxation spectrum with N relaxation modes, the storage and loss moduli for a certain frequency ω_j are given by:

$$G'(\omega_j) = \sum_{i=1}^{N} G_i \frac{(\omega_j \theta_i)^2}{1 + (\omega_j \theta_i)^2} \tag{3.23}$$

$$G''(\omega_j) = \sum_{i=1}^{N} G_i \frac{\omega_j \theta_i}{1 + (\omega_j \theta_i)^2} \tag{3.24}$$

for the multimode Maxwell behaviour. The spectrum for the Leonov is slightly different (Upadhyay *et al.* [57]):

$$G'(\omega_j) = \sum_{i=1}^{N} \eta_i \frac{\theta_i \omega_j^2}{1 + (\omega_j \theta_i)^2} \tag{3.25}$$

$$G''(\omega_j) = \eta_r \omega_j + \sum_{i=1}^{N} \eta_i \frac{\omega_j}{1 + (\omega_j \theta_i)^2} \tag{3.26}$$

Because $\eta_i = G_i \theta_i$, the Leonov model differs only from the Maxwell model in having an additional paramater η_r.

There are various techniques for fitting these equations to the experimental data. It is well-known that the determination of a discrete spectrum is an *ill-posed problem* (see [3, 25, 26, 27, 45]). This leads to undesired phenomena, such as a strong dependence of the solution of the choice and number

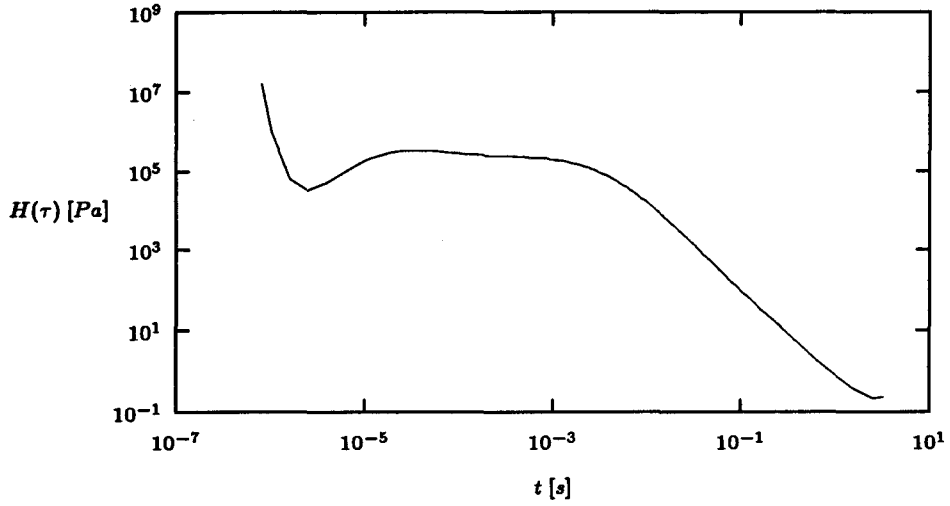

Figure 3.13: Continuous relaxation spectrum for PC Makrolon CD2000 at T = 511K

of parameters — some choices may even lead to negative values, which is physically not meanigful — and standard errors that can become as large as or even larger than the solution values. In the following, four techniques will be treated:

- linear least squares
- linear least squares with regularization
- Levenberg-Marquardt method
- Bayesian estimation method

These techniques deal with the minimization of the object function $\mathcal{H}$:

$$\mathcal{H} = \sum_{j=1}^{M} \left[\sum_{i=1}^{N} \left(\frac{\hat{G}'(\omega_j)}{G'(\omega_j)} - 1 \right)^2 + \sum_{i=1}^{N} \left(\frac{\hat{G}''(\omega_j)}{G''(\omega_j)} - 1 \right)^2 \right] \tag{3.27}$$

where $\hat{G}', \hat{G}''$ are the approximations of the moduli given by (3.23) and (3.24) and G', G'' are the measured data. Some definitions used in the description of the four methods will be given below. Let $\underset{\sim}{a} = [a_1 \cdots a_M]^T$ a column vector of the M parameters to be fitted. Let also $\underset{\sim}{y} = [1 \cdots 1]^T$, $\underset{\sim}{e} = \underset{\sim}{y} - \underset{\sim}{\hat{y}}$ the residual

vector, with

$$\hat{\underset{\sim}{y}} = \begin{bmatrix} \frac{\hat{G}'(\omega_1)}{G'(\omega_1)} \\ \vdots \\ \frac{\hat{G}'(\omega_M)}{G'(\omega_M)} \\ \hline \\ \frac{\hat{G}''(\omega_1)}{G''(\omega_1)} \\ \vdots \\ \frac{\hat{G}''(\omega_M)}{G''(\omega_M)} \end{bmatrix}$$

all column vectors of length $2M$. Then (3.27) can be written as minimizing

$$\mathcal{H}(\underset{\sim}{a}) = \frac{1}{2}\|\hat{\underset{\sim}{y}} - \underset{\sim}{y}\|_2^2 \tag{3.28}$$

where $\|\cdot\|_2$ is the 2-norm. The minimum of (3.28) occurs where the derivatives of $\mathcal{H}$ with respect to $\underset{\sim}{a}$ vanishes. The $2M \times n$ matrix containing the derivatives with respect to the parameters a_i is called the Jacobian matrix and looks like

$$\underline{K} = \begin{bmatrix} \frac{1}{G'(\omega_1)}\frac{\partial \mathcal{H}(\omega_1)}{\partial a_1} & \cdots & \frac{1}{G'(\omega_1)}\frac{\partial \mathcal{H}(\omega_1)}{\partial a_n} \\ \vdots & & \vdots \\ \frac{1}{G'(\omega_M)}\frac{\partial \mathcal{H}(\omega_M)}{\partial a_1} & \cdots & \frac{1}{G'(\omega_M)}\frac{\partial \mathcal{H}(\omega_M)}{\partial a_n} \\ \hline \\ \frac{1}{G''(\omega_1)}\frac{\partial \mathcal{H}(\omega_1)}{\partial a_1} & \cdots & \frac{1}{G''(\omega_1)}\frac{\partial \mathcal{H}(\omega_1)}{\partial a_n} \\ \vdots & & \vdots \\ \frac{1}{G''(\omega_M)}\frac{\partial \mathcal{H}(\omega_M)}{\partial a_1} & \cdots & \frac{1}{G''(\omega_M)}\frac{\partial \mathcal{H}(\omega_M)}{\partial a_n} \end{bmatrix}$$

Finally, the square error is defined by:

$$\epsilon^2 = 1/(2M - n)\underset{\sim}{e}^T\underset{\sim}{e} \tag{3.29}$$

Linear least squares If the data have to be fitted to a model that is a linear combination of some basis functions, a general linear least squares method can be applied. For a relaxation spectrum, this means fitting the moduli G_i for fixed relaxation times. Thus, the estimation for $\underset{\sim}{y}$ can be written as $\hat{\underset{\sim}{y}} = \sum_{i=1}^{N} \underline{K}\underset{\sim}{a}$. Generally the N relaxation times are equally spaced on the logarithmic time axis between $\theta_{min} = 1/\omega_{max}$ and $\theta_{max} = 1/\omega_{min}$.

The parameters can be estimated by solving the so-called normal equations

$$(\underline{K}^T\underline{K})\underset{\sim}{a} = \underline{K}^T\underset{\sim}{y} \tag{3.30}$$

by Gauss-Jordan elimination or LU-decomposition. However, this method is susceptible to round-off errors (Press *et al.* [51]) because the normal equations are in some cases close to singularity. Normally, this gives the user the warning that some basis functions, or some combinations of basis functions, are closely related. However, in the case of fitting the relaxation spectrum, it is sometimes desirable to fit a large number of relaxation modes to the data. This is, for example the case if the spectrum obtained is used to characterize the material.

This problem can be overcome by using a *Singular Value Decomposition (SVD)*. In a overdetermined system ($2M > N$), SVD produces a solution that is the best approximation in the least-squares sense. In the SVD the $2M \times N$ matrix can be written as

$$\underline{K} = \underline{U}\underline{W}\underline{V}^T \tag{3.31}$$

where $\underline{U}$ is an $2M \times 2M$ orthonormal matrix, $\underline{V}$ is an $N \times N$ orthonormal matrix, and $\underline{W}$ is an $N \times N$ diagonal matrix with positive numbers — the singular values of matrix $\underline{K}$ — in descending order. Then, the estimation of the parameters can be calculated with:

$$\underset{\sim}{a} = \underline{V}\underline{W}^{-1}\underline{U}^T\underset{\sim}{y} \tag{3.32}$$

and the standard error in the estimate of parameter a_i is given by

$$\sigma^2(a_i) = \sum_{k=1}^{N} \frac{V_{ik}^2}{W_{kk}^2} \tag{3.33}$$

Equation 3.33 shows that if the singular values of $\underline{K}$ are small, the standard error in a_i increases, meaning that a broad range of values for that parameter can fit the experimental data. This gives an idea of the ill-posedness of the problem. In practice one has to decide which of the small singular values are still meaningfull. If some singular value is smaller than a certain tolerance, the corresponding parameter is if no significance and can be thrown out the equation by setting the reciprocal of the singular value to zero (Press [51]).

The above mentioned solution methods often gives negative values for the estimated relaxation moduli. From a mathematical viewpoint this is correct, because it is just a fit, but these negative values are not physically meaningful. In this case a constrained optimization routine which forces $a_i \geq$ can be helpful. However, the large standard error of the estimated parameters still exists.

Linear least squares with regularization Recently, Honerkamp and Weese [25, 26, 27] proposed a method based on Tikhonov regularization. This regularization technique is used for solving ill-posed problems and is

introduced to reduce to values of the standard errors. The method is based on the SVD. The regularized version [1] of (3.32) is given by:

$$\underset{\sim}{a} = (\underline{V}\underline{W}^2\underline{V}^T + \lambda\underline{I})^{-1}\underline{V}\underline{W}\underline{U}^T\underset{\sim}{y} \tag{3.34}$$

in which the regularization parameter $\lambda > 0$. It can be derived that (3.34) is the solution of the minimization problem

$$\mathcal{H}^r = \mathcal{H} + \lambda\sum_{i=1}^{n} a_i^2 = minimum \tag{3.35}$$

The main problem when using this method is the determination of an appropriate regularization parameter. Honerkamp proposed the following (extra) minimization problem to obtain λ:

$$T(\lambda) = \sum_{i=1}^{n} \frac{\lambda^2}{W_{ii}^2 + \lambda}(\underset{\sim}{U}_i\underset{\sim}{y})^2 + 2\sigma^2\sum_{i=1}^{n}\frac{W_{ii}^2}{W_{ii}^2+\lambda} = minimum \tag{3.36}$$

where σ is the average standard error of the experimental storage and loss moduli. With this method Honerkamp and Weese were able to calculate a hypothetic relaxation spectrum using a large number of relaxation times, without the occurence of negative values of a_i. However, using the regularization for fitting the spectrum to the mastercurves of PS and PC did not give the desired results. Regardless how many relaxation times were chosen, the regularization parameter always was close to zero.

Levenberg-Marquardt method With the nonlinear least squares method of Levenberg-Marquardt it is possible to make a nonlinear regression to determine G_i as well as θ_i. The Levenberg-Marquardt method searches the solution in the direction defined by the modified normal equations (Gill *et al.* [20])

$$(\underline{K}_k^T\underline{K}_k + \lambda_k\underline{I})\delta\underset{\sim}{a}_k = \underline{K}_k^T\underset{\sim}{e}_k \tag{3.37}$$

where λ is a non-negative scalar and the subscript k denotes the iteration number. It is interesting to note that this is the same form as used in the regularization method, with the only difference that (3.37) is iteratively solved instead of in one step.

The estimation of the spectrum with the Levenberg-Marquardt method can be summarized by:

1. give an initial guess for $\underset{\sim}{a}$.
2. calculate square error $\epsilon^2(\underset{\sim}{a})$ with (3.29).
3. pick a value for λ_k, for instance $\lambda_k = 1$.

[1] if $\underline{K}$ is not written in the SVD-form this equation reads as $\underset{\sim}{a} = (\underline{K}^T\underline{K} + \lambda\underline{I})^{-1}\underline{K}^T\underset{\sim}{y}$

4. solve (3.37) for $\delta\underline{a}$ and calculate $\epsilon^2(\underline{a}+\delta\underline{a})$.
5. if $\epsilon^2(\underline{a}+\delta\underline{a}) \geq \epsilon^2(\underline{a})$, increase λ_k by a factor 2 and go back to 4.
6. if $\epsilon^2(\underline{a}+\delta\underline{a}) < \epsilon^2(\underline{a})$, decrease λ_k by a factor 2, update the trial solution $\underline{a} \leftarrow \underline{a}+\delta\underline{a}$, and go back to 4 until convergence has reached (within the given limits)

For the initial guess, the approximate relation (3.22) can be used.

The results of this method are rather good. The estimated parameters were all positive, if the right initial value for λ, for instance $1 \leq \lambda \leq 10$, was chosen. It proved to be useful to scale the relaxation moduli to prevent that the matrix $(\underline{K}_k^T\underline{K}_k + \lambda_k\underline{I})$ becomes ill-conditioned.

Bayesian estimation method Using a Bayesian estimation method not only information of the model and the measurements is used as in a least squares estimation, but also knowledge of the error distribution, and the prior density function of the parameters (weighting) can be used (Verbeek [60]). Like the Levenberg-Marquardt method, the Bayesian method estimates the relaxation times and moduli at the same time.

This estimation method combined with the Gauss-Newton optimization method proves to be rather robust and requires much less intervention of the user in comparison with the Levenberg-Marquardt method. As prior knowledge, a relative error of the parameters can be used.

Results The Bayesian estimation method gives the best results from a mathematical point of view. The relaxation spectrum which has the smallest square error in combination with the restriction that the estimated values for the confidence interval must be smaller than the parameter values is chosen as the best fit. This procedure is sligthly different from the one of Baumgärtel and Winter [3]. They start with a large number of relaxation times (between 1 or 2 per decade) and the spectrum is fitted using a non-linear least squares method. The number of relaxation times is altered during the computation. The criterium for reducing that number was the occurence of negative G_i's and the occurence of coinciding relaxation times. The spectrum with the smallest square error in combination with the smallest number of relaxation times was chosen as the best fit. Unfortunately, they have revealed no further details of their method.

The results are summarized in table 3.2 and 3.3 for PS and PC respectively.

3.2.2 Damping parameters

The parameters of the models for the damping functions can easily be fitted with a linear least squares method. However, the data to be fitted are difficult

Wagner		Leonov	
		$\eta_r = 1.096$ Pas	
θ_i s	G_i Pa	θ_i s	η_i Pas
$2.223 \cdot 10^{-7}$	$8.639 \cdot 10^{6}$	$8.835 \cdot 10^{-7}$	$1.297 \cdot 10^{0}$
$9.587 \cdot 10^{-6}$	$3.879 \cdot 10^{5}$	$1.127 \cdot 10^{-5}$	$3.044 \cdot 10^{0}$
$1.947 \cdot 10^{-4}$	$1.146 \cdot 10^{5}$	$1.175 \cdot 10^{-4}$	$1.236 \cdot 10^{1}$
$3.113 \cdot 10^{-3}$	$6.634 \cdot 10^{4}$	$1.144 \cdot 10^{-3}$	$7.185 \cdot 10^{1}$
$3.181 \cdot 10^{-2}$	$4.230 \cdot 10^{4}$	$8.898 \cdot 10^{-3}$	$4.186 \cdot 10^{2}$
$2.583 \cdot 10^{-1}$	$1.656 \cdot 10^{4}$	$5.842 \cdot 10^{-2}$	$1.718 \cdot 10^{3}$
$1.902 \cdot 10^{0}$	$2.330 \cdot 10^{3}$	$3.290 \cdot 10^{-1}$	$3.881 \cdot 10^{3}$
		$1.946 \cdot 10^{0}$	$4.202 \cdot 10^{3}$

Table 3.2: Linear viscoelastic parameters PS Styron 678E at $T = 462$K

Wagner		Leonov	
		$\eta_r = 1.017$ Pas	
θ_i s	G_i Pa	θ_i s	η_i Pas
$5.993 \cdot 10^{-7}$	$2.424 \cdot 10^{6}$	$6.154 \cdot 10^{-6}$	$4.092 \cdot 10^{0}$
$1.282 \cdot 10^{-5}$	$5.831 \cdot 10^{5}$	$6.223 \cdot 10^{-5}$	$3.537 \cdot 10^{1}$
$1.015 \cdot 10^{-4}$	$5.215 \cdot 10^{5}$	$4.338 \cdot 10^{-4}$	$1.911 \cdot 10^{2}$
$6.048 \cdot 10^{-4}$	$3.789 \cdot 10^{5}$	$2.290 \cdot 10^{-3}$	$3.823 \cdot 10^{2}$
$2.942 \cdot 10^{-3}$	$1.263 \cdot 10^{5}$	$1.110 \cdot 10^{-2}$	$2.479 \cdot 10^{2}$
$1.304 \cdot 10^{-2}$	$1.558 \cdot 10^{4}$	$6.710 \cdot 10^{-2}$	$1.595 \cdot 10^{1}$
$7.609 \cdot 10^{-2}$	$1.490 \cdot 10^{2}$		

Table 3.3: Linear viscoelastic parameters PC Makrolon CD2000 at $T = 511$K

to obtain. There are several ways to get h as a function of the shear strain γ.

The first method makes use of the results of the step strain stress relaxation experiments (figure 3.16). It can be derived that $G(t, \gamma_0) = G^{\ell}(t)h(\gamma_0)$, with $G^{\ell}(t)$ the linear shear relaxation modulus (Laun [36, 37]). The moduli can be shifted vertically onto the linear relaxation modulus to form a mastercurve. The amount of the vertical shift $G(t, \gamma_0)/G^{\ell}(t)$ gives the value of h for the corresponding γ_0. In this way it was possible to determine h up to $\gamma_0 = 5$, which is rather limited.

The second method uses the results of the stress-growth experiments to determine the values of the damping function. Following Wagner [64], $h(\gamma)$

can be derived from the measured $\tau_{12}(t)$ and $N_1(t)$ with $\gamma = \dot{\gamma}t$:

$$h(\gamma) = \frac{1}{\gamma}\left[\frac{\tau_{12}(\gamma)}{G^{\ell}(\gamma)} - \frac{1}{\dot{\gamma}}\int_0^{\gamma} \tau_{12}(\gamma')\frac{m^{\ell}(\gamma')}{G^{\ell 2}(\gamma')}\,d\gamma'\right] \tag{3.38}$$

$$h(\gamma) = \frac{1}{\gamma^2}\left[\frac{N_1(\gamma)}{G^{\ell}(\gamma)} - \frac{1}{\dot{\gamma}}\int_0^{\gamma} N_1(\gamma')\frac{m^{\ell}(\gamma')}{G^{\ell 2}(\gamma')}\,d\gamma'\right] \tag{3.39}$$

where m^{ℓ} is the linear viscoelastic memory function. In this way, values for $h(\gamma)$ up to $\gamma = 20$ can be obtained.

The parameters of the models for the damping function can also be determined directly by fitting the equation that decribes the experiment to the experimental data. For example, the exponential model for the damping function, can be obtained to fit equation (B.3) to the measured transient viscosity. It proved that the primary normal stress in the constant shear rate experiments is most sensitive to the choice of the parameters in the model, so this type of experiments is preferred over the steady-state viscosity data.

Now the damping values are determined, the models of the damping functions can be fitted to the data (figure 3.14). The parameters of the damping functions models can be found in table 3.4. In contrast with the findings of Laun [37], the values of the damping function determined with the step strain experiments differ not much of the values obtained with (3.39).

	PS Styron 678E
m	0.84
n_1	0.34
n_2	0.19
β	0.14

Table 3.4: Damping function parameters (Wagner double exponential and Papanastasiou)

3.3 Comparison of constitutive models

With the spectrum determined and the damping parameters found it is possible to predict various types of shear flow experiments with the constitutive equations. The expressions that describe a particular shear flow can be found in Appendix B. The comparisons are given for PS only. The calculations are carried out using the linear viscoelastic parameters determined in the previous section. The non-linear behaviour of the melt is described by the double exponential damping function for the Wagner model.

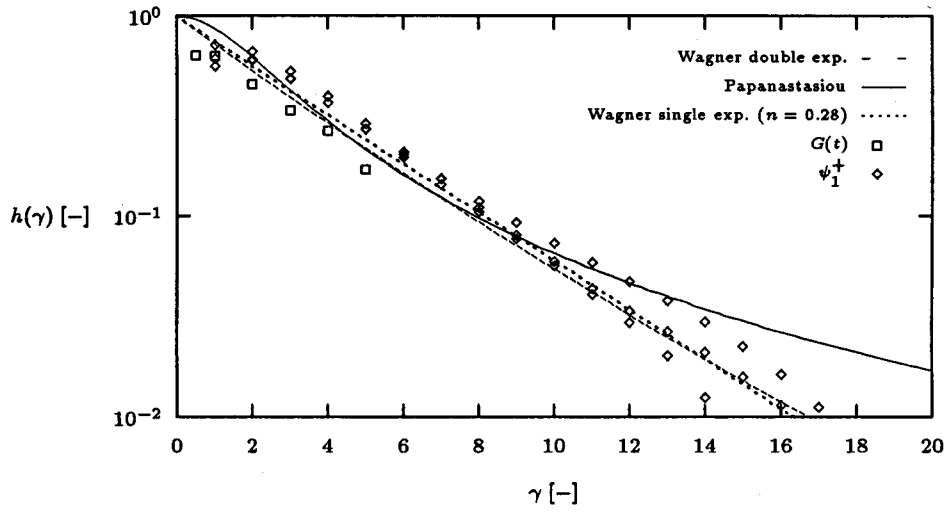

Figure 3.14: Damping function of PS Styron 678E as evaluated form step-strain experiments and constant shear rate experiments. The lines represents the fitted models.

Steady state viscosity

Applying the empirical Cox-Merz rule, the steady-state viscosity values can be considered equal to the values of the dynamic viscosity

$$\eta(\dot{\gamma}) = \eta_d(\omega)|_{\omega=\dot{\gamma}} \qquad \eta_d = \sqrt{\eta'^2 + \eta''^2} \tag{3.40}$$

To check the validity of the Cox-Merz rule, the steady state viscosity is measured for shear rates up to $2s^{-1}$ with the Rheometrics RMS-800 and in the high shear rate region with a capillary rheometer (both at DSM Research). The measured results and the model predictions are depicted in figure 3.15 for PS. The predicted values with the Wagner model are slightly below the measured values. However, it may be concluded that the experimental results compare well with the model predictions.

Step strain stress relaxation

For this type of strain history the results are only calculated with the Leonov model. The damping function of the Wagner model is fitted to these results, so it is of no use to check the predictive quality of this model with this experiment. The results can be found in figure 3.16. The predicted relaxation modulus deviates from the measured modulus in the region of small γ_0. At higher shear strains the predicted moduli agree well with the measured ones.

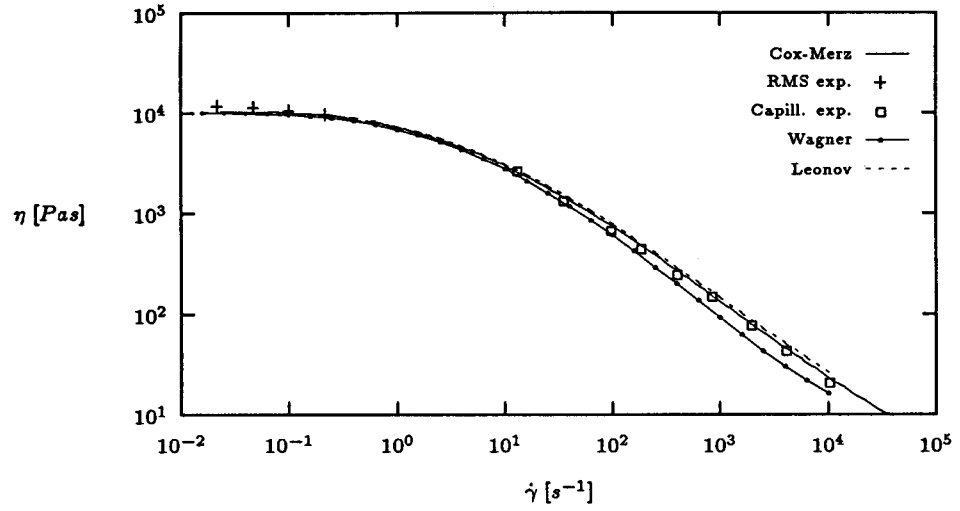

Figure 3.15: Steady state shear viscosity as function of shear rate of PS Styron 678E at $T = 462$K

Stress growth at constant shear rate

The results of the predictions of the Wagner and Leonov model for the constant shear rate experiments can be found in figure 3.17 and 3.18. In the low shear rate region, the predictions are worse than at the higher shear rates. In spite of the fact that the parameters of the damping model are fitted with the data of the primary normal stress coefficient, the results are a little disappointing. The difference at the smaller times (the delay with respect to the measured values) is probably due to a radial flow of the melt in the cone-plate gap (Laun [37]). However, the essential features such as the stress-overshoot are described by both models.

Stress relaxation after cessation of steady shearing flow

Finally the predictions of the Wagner and the Leonov model are given for the stress relaxation after cessation of steady shearing flow experiment. The results are shown in figure 3.19 and figure 3.20. The largest differents between the predicted and the measured values are found with this experiment. Again the predictions at relatively low shear strain values are much worse than at the higher strains, especially at the longer times. The observed difference in this region is probably due to the fact that the maximum relaxation time used for the calculations is too small. Extending the relaxation time spectrum with higher values for the relaxation times will give better

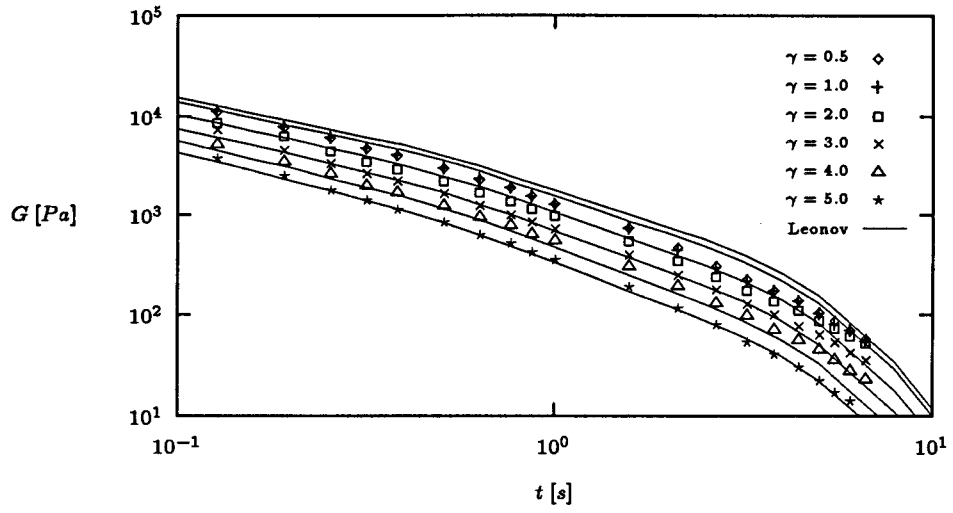

Figure 3.16: Step strain stress relaxation experiments for PS Styron 678E at T = 462K.

results (see Appendix C). However, adding more modes to the spectrum will increase the computating time with numerical calculations of realistic flows considerably, because for every relaxation mode the stress must be evaluated. Moreover, from a mathematical viewpoint the spectrum with more modes than in the 'optimal' spectrum is less accurate, because the estimated confidence interval can become as large as the estimated parameter values. For the extended spectrum given in Appendix C, the confidence intervals for most of the parameters are nearly as twice as large as the parameter values itself!

3.4 Conclusion

In this chapter two viscoelastic constitutive equations are compared with experimental results. For that purpose the model parameters are fitted. The model predictions using the mathematical best fit give a poor description of the stress growth at constant shear rate and the cessation after steady shearing experiments. The results obtained with an extended spectrum fit the measurements quite well. For the numerical simulations of the multilayer injection moulding process a generalized Newtonian constitutive equation is used (see Appendix D).

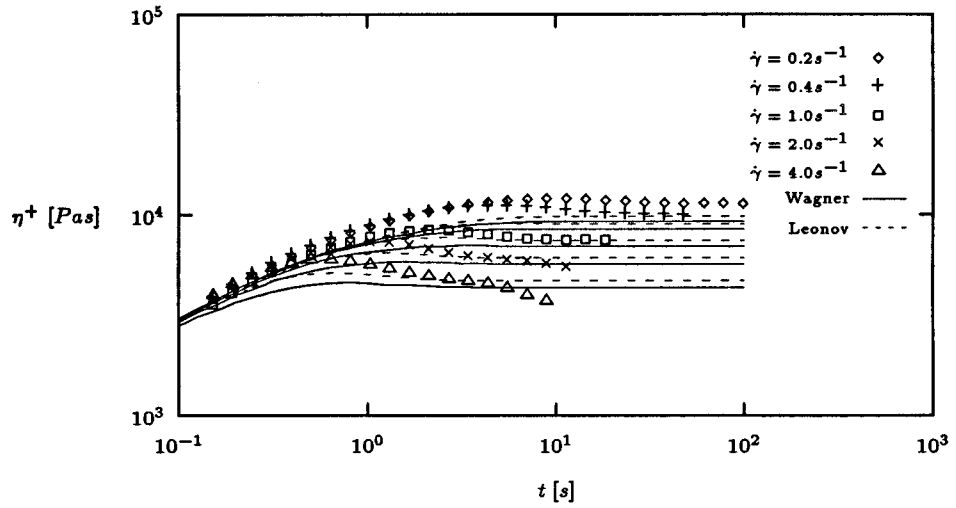

Figure 3.17: Transient viscosity for PS Styron 678E for stress growth at constant shear reates of $\dot{\gamma}_0 = 0.2, 0.4, 1, 2$, and $4s^{-1}$ at $T = 462$K.

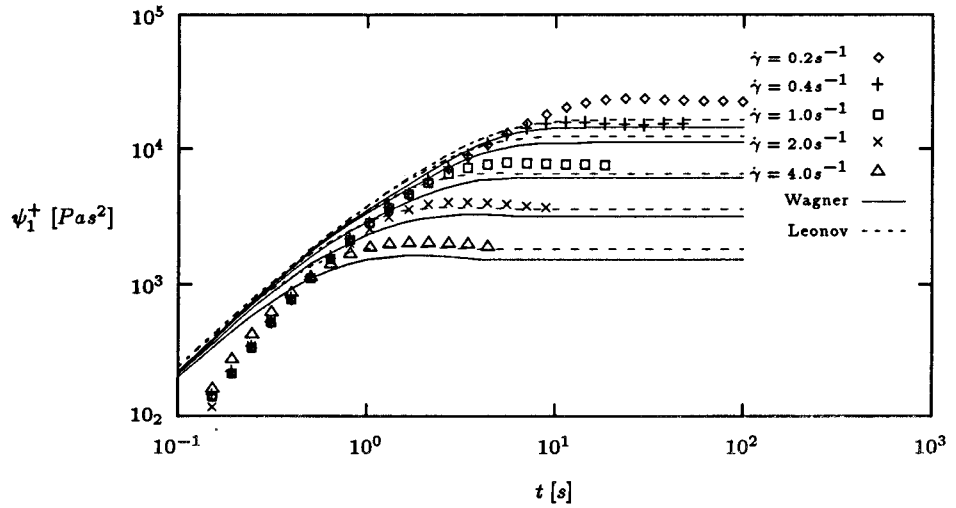

Figure 3.18: Transient primary normal stress coefficient for PS Styron 678E for stress growth at constant shear reates of $\dot{\gamma}_0 = 0.2, 0.4, 1, 2$, and $4s^{-1}$ at $T = 462$K.

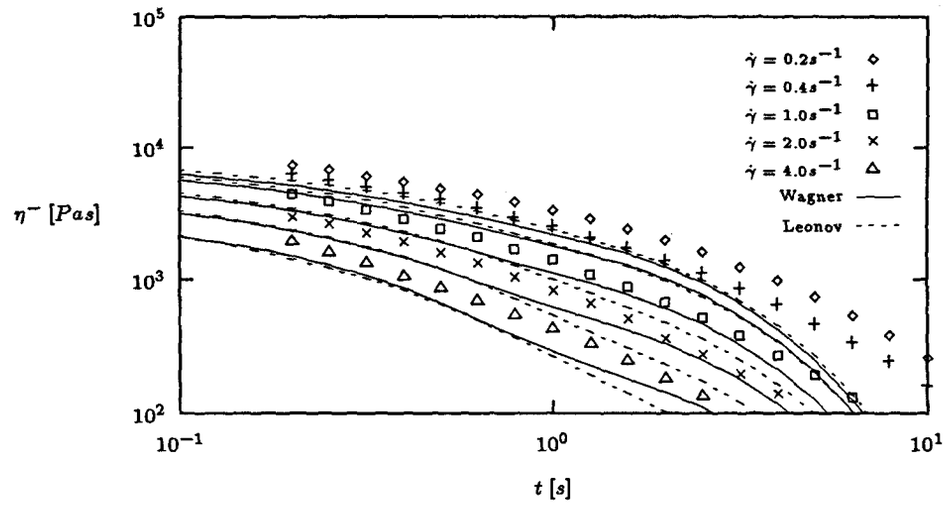

Figure 3.19: Transient viscosity for PS Styron 678E for stress relaxation after steady shear with shear reates of $\dot{\gamma}_0 = 0.2, 0.4, 1, 2$, and $4s^{-1}$ at $T = 462$K.

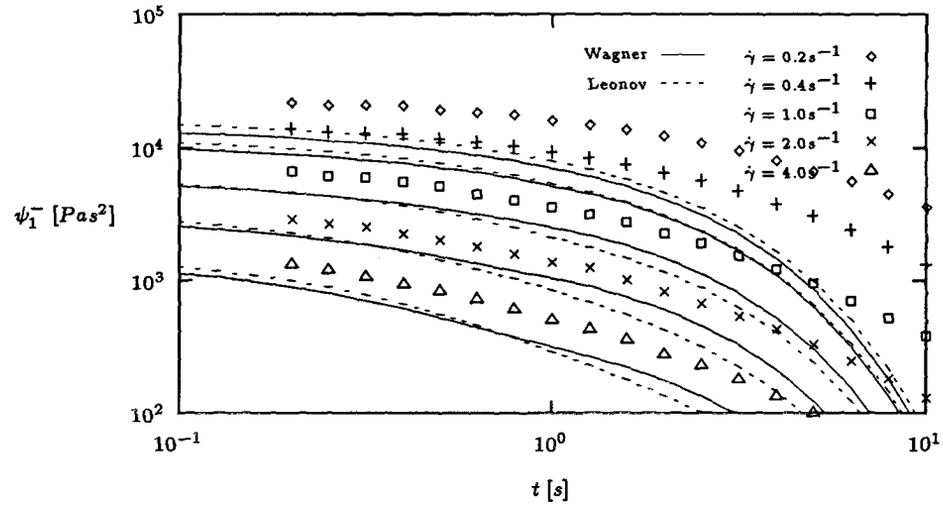

Figure 3.20: Transient primary normal stress coefficient for PS Styron 678E for stress relaxation after steady shearing with shear reates of $\dot{\gamma}_0 = 0.2, 0.4, 1, 2$, and $4s^{-1}$ at $T = 462$K.

Chapter 4

Numerical aspects of particle tracking

In this section several numerical schemes will be discussed to solve the instationary scalar convection equation (2.31). One problem that must be dealt with is the ability of convecting steep gradients in the solution field. In the application to particle tracking, these gradients are introduced in the solution by the redistribution of the scalar values in the front region or by the occurence of weldlines. The convection equation can be solved by either FDM or FEM techniques. The performance of these schemes is tested with two model problems, a translating Gaussian hill in 1D and a rotating Gaussian hill in 2D (Molenkamp test [50]).

4.1 Finite difference solution

The class of hyperbolic partial differential equations, to which the instationary convection type of equations belong, can be solved with a large number of FDM schemes (see for instance Hirsch [24]). Some of the schemes are developed for dealing with large gradients in the solution field. Most of them stem from the field of gas-dynamics for the calculation of the travelling of shockwaves. In this section, a brief overview of some schemes is given together with some illustrative examples in 1D and 2D.

For convenience the one-dimensional convection equation is used for deriving the FDM schemes. The problem is stated as: find a solution $c(x,t)$ of

$$\frac{\partial c}{\partial t} + v\frac{\partial c}{\partial x} = 0 \tag{4.1}$$

$$c(x,0) = \phi(x) \tag{4.2}$$

with $\phi(x)$ a known filed, and $v \geq 0$. The time domain of interest is given by $\mathcal{T} =]0,t[$ and the spatial domain by $\Omega =]-\infty,\infty[$, so there is no influence of

boundary conditions. The equation is computed in a $m \times k$ equally spaced grid in the space-time domain in which a meshpoint is represented by $(x,t) = (i\Delta x, n\Delta t)$.

A finite difference scheme is derived by chosing an appropriate approximation of the temporal and spatial derivative in (4.1). The following schemes will be treated:

- Forward Euler schemes
  - central difference
  - first order upwind
  - Van Leer
- Backward Euler schemes
  - central difference
- Crank-Nicholson scheme
- Baker and Oliphant scheme

This schemes demonstrate the most important features of these numerical approximations, such as stability, numerical diffusion and dispersion. The schemes are at most second order accurate in space. Higher order schemes are not treated, because they are seldom found in practical applications.

Forward Euler schemes

In this type of schemes, the temporal derivative is approximated by forward difference formula. This leads to an explicit scheme, since each discretized equation contains only one unkown at time $t+\Delta t$. The Euler explicit schemes are first order accurate in time ($\mathcal{O}(\Delta t)$).

Central difference

Writing the spatial derivative as a central difference formula, the well-known scheme of $\mathcal{O}(\Delta t, \Delta x^2)$ reads:

$$\frac{c_i^{n+1} - c_i^n}{\Delta t} + v\frac{c_{i+1}^n - c_{i-1}^n}{2\Delta x} = 0 \tag{4.3}$$

The computational molecule looks like:

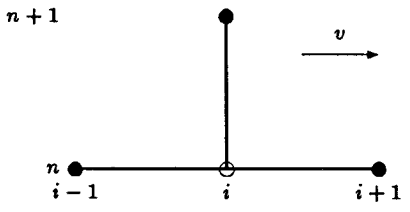

It can be derived easily by a check of consistency that the truncation error ϵ_T of this scheme is given by:

$$\epsilon_T = -\frac{\Delta t}{2} v^2 \frac{\partial^2 c}{\partial x^2} + \mathcal{O}(\Delta t^2, \Delta x^2) \tag{4.4}$$

The equivalent differential equation contains an additional (numerical) diffusion term with a negative coefficient. It may be obvious that this scheme is unstable, since the negative numerical diffusion causes amplification of any disturbance.

First order upwind

In the first order upwind scheme, the spatial derivative is approximated by a first order backwards difference formula:

$$\frac{c_i^{n+1} - c_i^n}{\Delta t} + v \frac{c_i^n - c_{i-1}^n}{\Delta x} = 0 \tag{4.5}$$

In this case, only one meshpoint in the upstream direction is used :

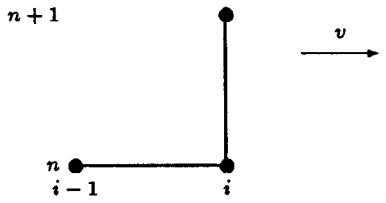

The truncation error is given by

$$\epsilon_T = -(\frac{\Delta t}{2} v^2 - v \frac{\Delta x}{2}) \frac{\partial^2 c}{\partial x^2} + \mathcal{O}(\Delta t^2, \Delta x^3) \tag{4.6}$$

This scheme adds numerical diffusion to the original differential equation. The scheme is conditionally stable for

$$\frac{v \Delta t}{\Delta x} \leq 1 \tag{4.7}$$

Equation (4.7) is called the Courant-Friedrichs-Lewy (CFL) condition. It is useful to define the dimensionless number $Cou = \frac{v \Delta t}{\Delta x}$, called the Courant number. With this definition the CFL-condition is expressed as $Cou \leq 1$.

Van Leer

The Van Leer FDM combines two schemes, the first order upwind scheme and the second order accurate upwind scheme of Fromm ([33, 50, 59]). The method works with a flux-limiter to switch between the two schemes. The fluxes are calculated across the cell-boundaries of a certain mesh-point. For equally spaced meshpoints, this implies that a staggered grid is used to calculate the fluxes. This is shown in the computational molecule.

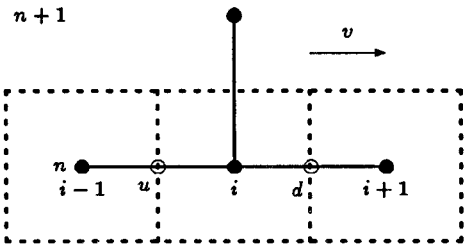

Inbetween the points i and $i+1$ an downstream point d represents the downstream cell boundary of point i, whereas the upstream point u is the downstream point of mesh-point $i-1$. The value of c_d is calculated using the flux limiter: If

$$|c_{i-1}^n - 2c_i^n + c_{i+1}^n| \geq |c_{i-1}^n - c_{i+1}^n|$$

there are wiggles detected and $c_d^n = c_i^n$, corresponding to the upwind flux of the first order upwind scheme, otherwise c_d^n is calculated with

$$c_d^n = c_i^n + (1 - Cou^n)\frac{(c_i^n - c_{i-1}^n)(c_{i+1}^n - c_i^n)}{(c_{i+1}^n - c_{i-1}^n)}$$

which is the limited Fromm flux. With these fluxes the values at time-level $t + \Delta t$ can be calculated with the formula:

$$c_i^{n+1} = c_i^n + (Cou_d^n\, c_d^n - Cou_u^n\, c_u^n) \tag{4.8}$$

where Cou_d^n, Cou_u^n are the Courant numbers evaluated at the downstream and upstream cell boundaries respectively. In other words: as long as the solution field is smooth a high order scheme is used, but if oscillations occur they are damped out with a first order upwind scheme. It can be derived that the Van Leer scheme is $\mathcal{O}(\Delta t, \Delta x^2)$ if no onset of wiggles is detected, otherwise the scheme is of order $\mathcal{O}(\Delta t, \Delta x)$. Because of the incorporating of the first order upwind scheme, the Van Leer scheme is conditionally stable for $Cou \leq 1$.

Backward Euler schemes

Chosing a backward difference for the temporal derivative, the implicit or backward Euler schemes can be derived. Now, the unknowns appear all at time-level $t + \Delta t$. The Euler implicit schemes are all first order accurate in time ($\mathcal{O}(\Delta t)$). *Central difference*

The difference scheme can be derived by simple changing the subscripts n in the spatial derivative of (4.3) by $n+1$:

$$\frac{c_i^{n+1} - c_i^n}{\Delta t} + v\frac{c_{i+1}^{n+1} - c_{i-1}^{n+1}}{2\Delta x} = 0 \tag{4.9}$$

With the computational molecule:

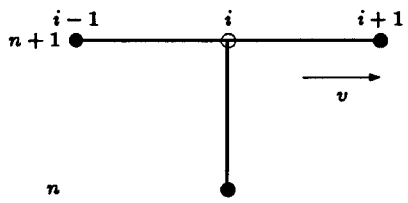

The truncation error derived by a check of consistency is of the form:

$$\epsilon_T = \frac{\Delta t}{2} v^2 \frac{\partial^2 c}{\partial x^2} + \mathcal{O}(\Delta t^2, \Delta x^2) \tag{4.10}$$

The first term in the truncation error represents the numerical diffusion. In constrast with the explicit scheme, the diffusion coefficient is positive, so that this scheme is unconditionally stable for all v.

Other difference formulas for the spatial derivatives can be used as well (for instance an upwind difference), but will not given here.

Crank-Nicholson scheme

In the Crank-Nicholson scheme 6 mesh-points are considered in evaluating c_i^{n+1}, 3 at time-level n and 3 at level $n+1$. In fact, it is a weighted average of the explicit and implicit Euler schemes.

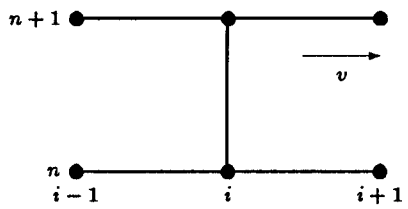

Using a central difference formula for the convection term, the scheme is formulated by:

$$\frac{c_i^{n+1} - c_i^n}{\Delta t} + \theta v \frac{c_{i+1}^{n+1} - c_{i-1}^{n+1}}{2\Delta x} + (1-\theta) v \frac{c_{i+1}^n - c_{i-1}^n}{2\Delta x} = 0 \tag{4.11}$$

with $0 \leq \theta \leq 1$. The Crank-Nicholson scheme appears for $\theta = 1/2$. The truncation error is given by:

$$\epsilon_T = -v^2 \frac{\Delta t}{2}(1-2\theta)\frac{\partial^2 c}{\partial x^2} + (\cdots)\frac{\partial^3 c}{\partial x^3} + \mathcal{O}(\Delta t^4, \Delta x^4) \tag{4.12}$$

The scheme is unconditionally stable, because the numerical diffusion is positive for $0 \leq \theta \leq 1$. However, for $\theta = 1/2$ this term vanishes and the order of accuracy in time is increased by one. In that case, the truncation error

contains additional dispersion, causing oscillations when steep gradients in the solution field are present.

Using this scheme with an upwind difference formula instead of the central difference for the convective derivative the diffusion is introduced and the order of accuracy in space is reduced to $\mathcal{O}(\Delta x)$.

Baker and Oliphant scheme

In the implicit scheme derived by Baker and Oliphant, three time-levels are considered in evaluating the temporal derivative. Using the central difference formula for the convective term, the finite difference scheme reads:

$$\frac{3c_i^{n+1} - 4c_i^n + c_i^{n-1}}{2\Delta t} + v\frac{c_{i+1}^{n+1} - c_{i-1}^{n+1}}{2\Delta x} = 0 \tag{4.13}$$

With the computational molecule:

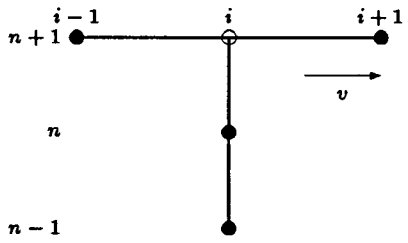

The truncation error is given by:

$$\epsilon_T = (-\frac{v^3\Delta t^2}{3} - \frac{v\Delta x^2}{6})\frac{\partial^3 c}{\partial x^3} + \mathcal{O}(\Delta t^4, \Delta x^4) \tag{4.14}$$

The truncation error of this unconditionally stable scheme is dispersive.

Test problems

The presented finite difference schemes are tested with a convection of a Gaussian hill. The explicit schemes are tested in 1D as wel as in 2D. The conditions of the test problems are:
1D:

$$v = 1,\ x \in [0,1],\ \Delta t = \frac{1}{90},\ \Delta x = \frac{1}{50},\ t_0 = 0 \text{ and } t_{end} = 0.4.$$

$$\phi(x) = \exp\left(-\frac{1}{2}(\frac{x - 0.2}{\sigma})^2\right)$$

2D (Molenkamp test):

$$v = [2\pi y, 2\pi x],\ (x,y) \in [0,1] \times [0,1],\ \Delta t = \frac{1}{470},\ \Delta x = \Delta y = \frac{1}{40},$$

$$t_0 = 0, \text{ and } t_{end} = 1.$$

$$\phi(x,y) = \exp\left(-\frac{1}{2}((\frac{x - 0.3}{\sigma})^2 + (\frac{y - 0.3^2}{\sigma}))\right)$$

where $\sigma = 0.06$. The maximum Courant number is $Cou = 0.55$ for both the test problems.

Test problem 1

The results of the test problem for the explicit central scheme are shown in figure 4.1a. For this scheme the Gaussian hill is convected in 10 time steps, clearly demonstrating the instability of this scheme.

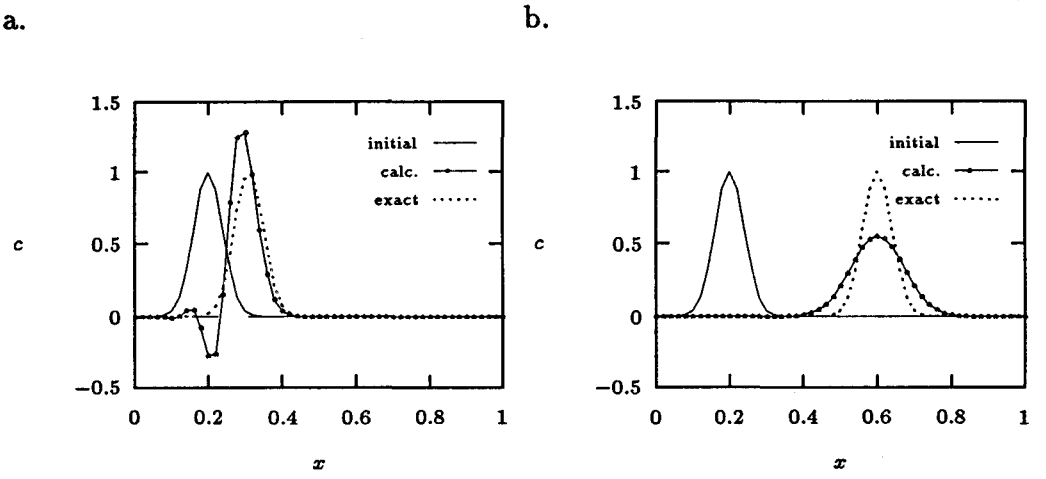

Figure 4.1: Translating Gaussian hill. Euler explicit schemes: central difference (a) and first order upwind (b)

The results of the other two explicit schemes are shown in figure 4.1b and 4.2a. In both cases the convected solution is flattened compared with the exact solution. The Van Leer scheme proves to be much less diffusive then the first order upwind scheme. The maximum of the solution is convected well, in terms of position, by both schemes. The diffusive nature of the implicit,central scheme can be seen in figure 4.2b. with this scheme the maximum of the convected solution lags behind the maximum of the exact solution. The same phenomenon occurs with the Crank-Nicholson,central (figure 4.3a) and the Baker and Oliphant,central scheme (figure 4.3b). However, these schemes are much less diffusive than the other ones, but the numerical dispersion introduces oscillations in the upstream direction.

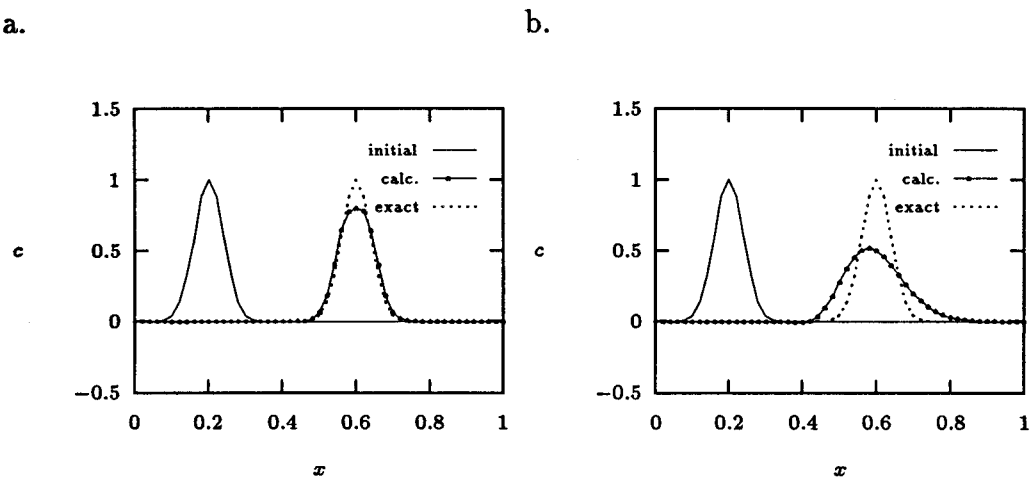

Figure 4.2: Translating Gaussian hill. Euler explicit, Van Leer scheme (a) and Euler implicit, central difference scheme (b)

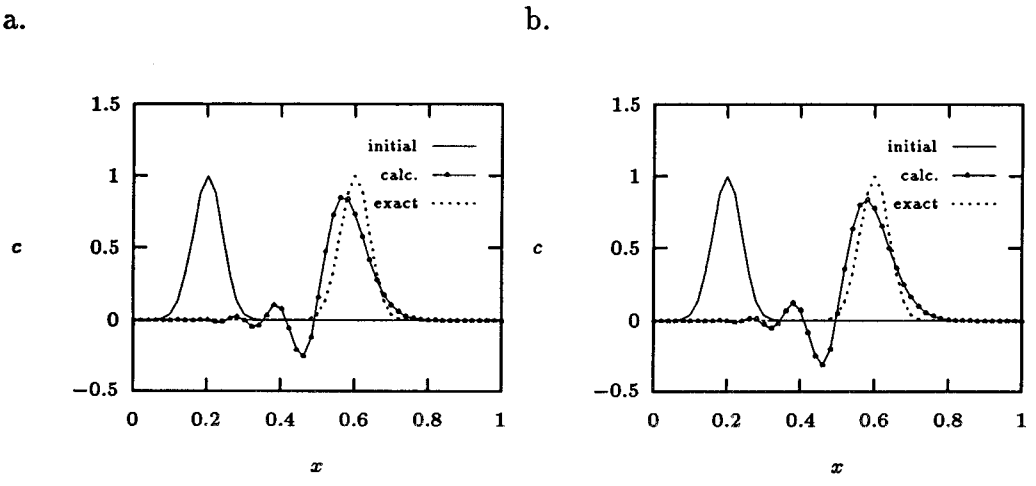

Figure 4.3: Tranlating Gaussian hill. Crank-Nicholson, central difference scheme (a) and Baker and Oliphant, central difference scheme (b)

Test problem 2 (Molenkamp test)

The initial solution of this test problem is plotted in figure 4.4. The Gaussian hill is rotated a full revolution with the first order upwind and the Van Leer scheme. The results are shown in figure 4.5 and 4.6. In 2D the first order upwind is much more diffusive than in 1D, the maximum height is dropped below 14% of the initial value. The Van Leer scheme shows the same behaviour, but the maximum is still 50% of the initial value.

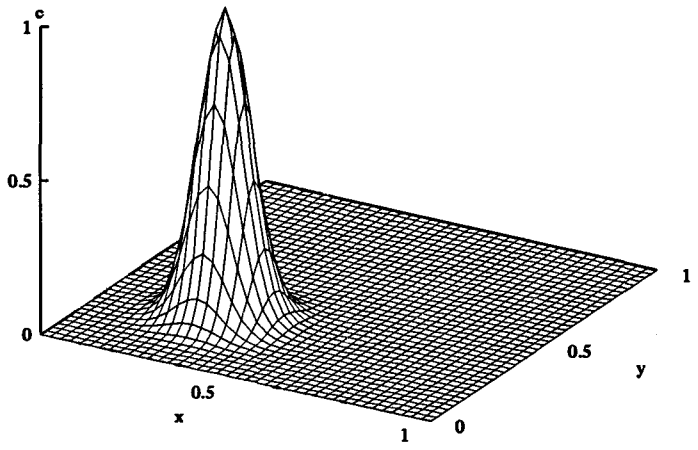

Figure 4.4: Initial solution for Molenkamp test

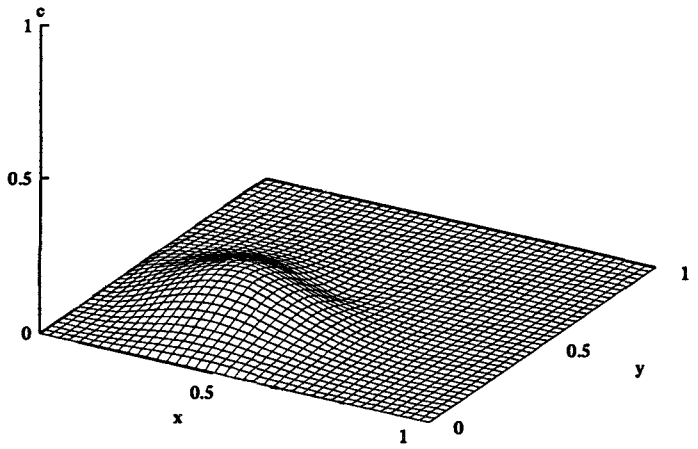

Figure 4.5: Rotating Gaussian hill. Euler explicit, first order upwind

From the test problems it can be concluded that the Van Leer finite difference scheme gives the best results, i.e. no oscillations and an exact convection of the maximum.

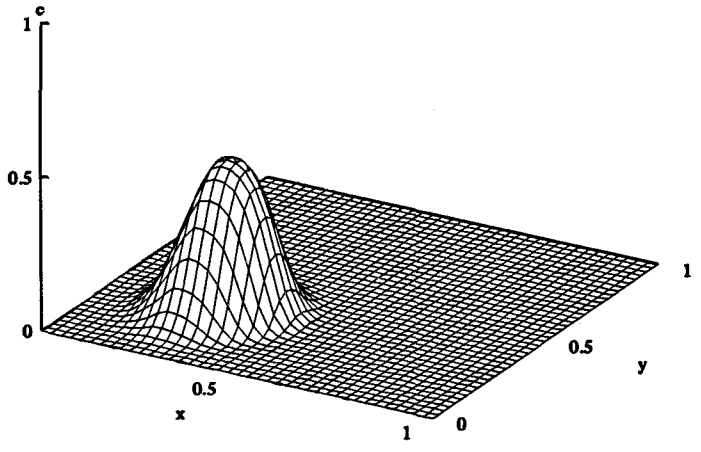

Figure 4.6: Rotating Gaussian hill. Euler explicit, Van Leer

4.2 Finite element solution

The finite element method (FEM) originates from the field of structural analysis. Nowadays, a lot of attention is paid to develop methods for solving convection dominated type of problems, e.g. in simulating the flow of viscoelastic fluids.

In FEM the space domain is divided in elements of arbitrary shape and size, usual triangles or quadrilaterals for a 2D problem. Within an element a number of points (nodes) are defined in which the unknown values are determined. The field variables are approximated by a linear combination of known *shape functions*. The approximate solution c^h of $c(\vec{x})$ can be written as:

$$c^h(\vec{x}) = \sum_{A}^{N_{nd}} \tilde{N}_A(\vec{x}) c_A \tag{4.15}$$

where the summation is performed over all nodes N_{nd}, $\tilde{N}_A(\vec{x})$ is the shape function for node A and c_A is the approximate solution at that node. Consider a one-dimensional finite element mesh with piecewise linear shape functions, then the shape functions are illustrated by:

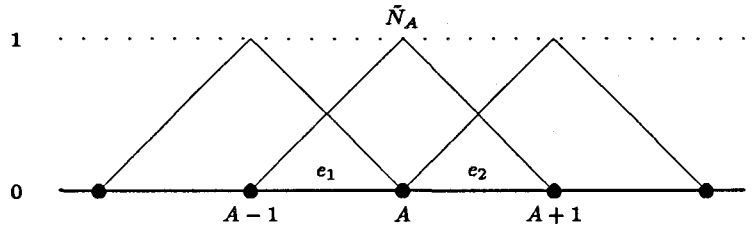

Using the weighted residual formulation, the weak form of the convection equation is given by

$$(w, \frac{\partial c}{\partial t} + \vec{v} \cdot \vec{\nabla} c) = 0 \tag{4.16}$$

In the Bubnow-Galerkin FEM, the weighting functions w are taken equal to the shape functions $\tilde{N}$. Due to the symmetry of the interpolation of the weighting functions, the Bubnow-Galerkin FEM gives a central difference scheme for the convective derivative when used on a uniform mesh. It is known in the previous section that this type of difference schemes are unstable or that they introduce oscillations depending on the choice of the time-integration (explicit or implicit). This behaviour is clearly demonstrated in figure 4.7 and 4.8. In these figures the results are plotted of the Molenkamp test with the same test conditions as with the FDM schemes. The time-integration is performed by the Euler implicit (figure 4.8) and the Crank-Nicholson method (figure 4.7). The calculations are performed with the finite element package SEPRAN using 3200 linear triangular elements.

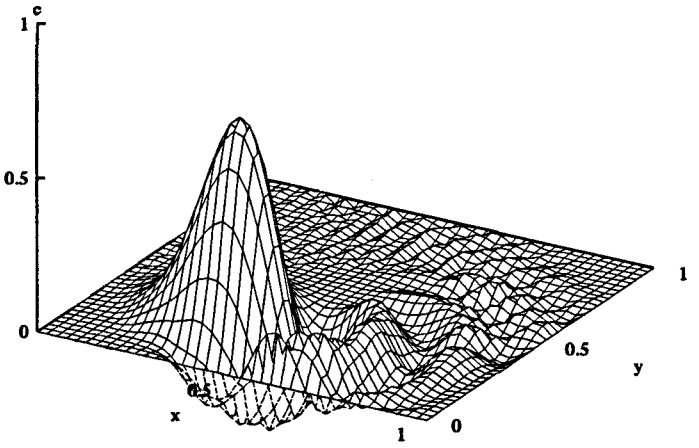

Figure 4.7: Rotating Gaussian hill. Galerkin solution with the Crank-Nicholson time-integration

In accordance with the results of the 1D test problem, also oscillations in the upstream direction are generated.

With the knowledge obtained from the analysis of the finite difference schemes, it proves desirable to use an upwind scheme to get rid of the oscillations. Therefore, the weighting functions have to be modified in such a way that the upstream nodes are weighted heavier than the downstream nodes. For this purpose, Hughes and Brooks [10] proposed to modify the weighting function by:

$$\tilde{w} = w + \alpha \vec{v} \cdot \vec{\nabla} w \tag{4.17}$$

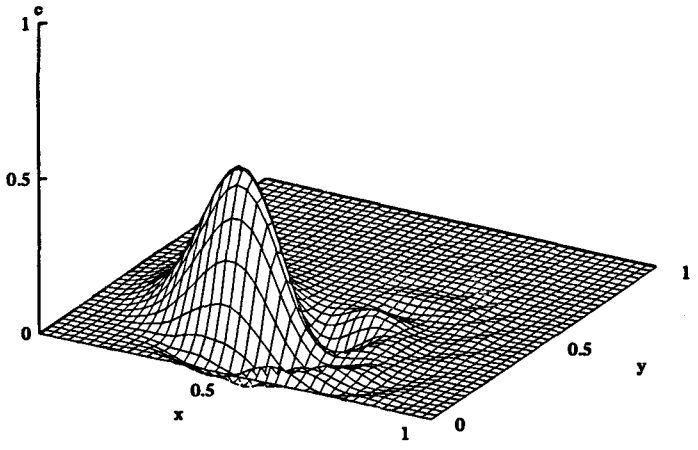

Figure 4.8: Rotating Gaussian hill. Galerkin solution with the Euler implicit time-integration

For linear 1D elements such a weighting function is plotted in figure 4.9. Now,

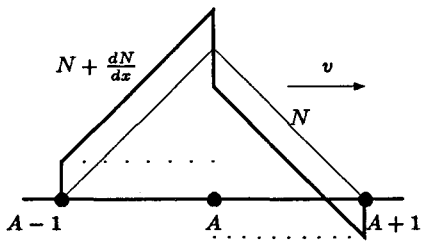

Figure 4.9: Upwind basis functions for SUPG in a one dimensional mesh

the weighting functions differ from the shape functions, which is known as the Petrov-Galerkin FEM. For the basis functions given in figure 4.9 the method is called the Streamline Upwind Petrov Galerkin (SUPG) FEM. Results of this method for the Molenkamp test are shown in figure 4.10. The temporal derivative is approximated by the Crank-Nicholson time integration and again 3200 linear triangular elements are used. The test conditions are equal to the conditions given for the FDM schemes.

There are various other methods developed for solving the convection problem which are not discussed here, because they are not yet implemented and tested. Some of these schemes are known for finite element formulations and for finite difference schemes. For example, the Explicit Taylor-Galerkin

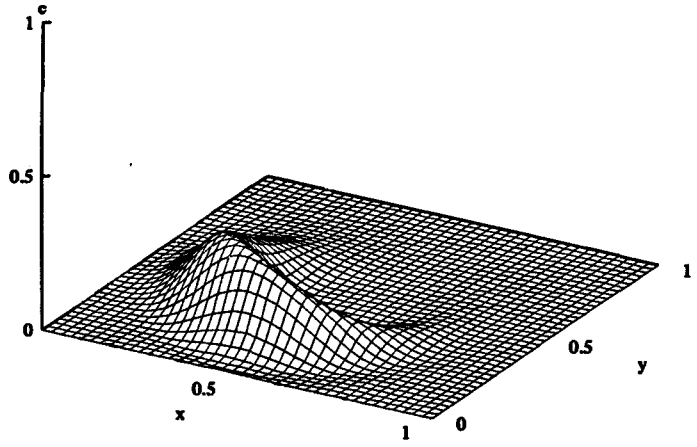

Figure 4.10: Rotating Gaussian hill. SUPG with Crank-Nicholson time-integration

method is better known as the Lax-Wendroff finite difference scheme [2]. The equivalence of the Van Leer scheme in FEM is the Taylor-Galerkin Discontinuous Finite Element Method (TG/DFEM) [13]. A promising method is the Time Discontinuous Galerkin Least Squares (TD/GLS) method. With this method the weighting function in not only modified by adding the derivative of the weighting function, but it is modified with the whole differential equation. This requires a finite element discretization of the time as well, because the weighting funtion has become time-dependent. Using an upwinding by discontinuity in time the problem size can be reduced, because only one time slab has to be considered at the time. Results of these methods can be found in: Baaijens [2] and Pironneau [49].

4.3 Conclusion

In this chapter numerical schemes are discussed for solving the instationary scalar convection equation. For the simulation of the multilayer moulding process, the Galerkin FEM with the Euler implicit time-integration is implemented in VIp. Some results can be found in the next chapter. The oscillations introduced by this scheme are undesirable for particle tracking, since then additional label values are created. Hence, the more advanced finite element techniques will be studied in future.

Chapter 5

Numerical simulations

In this chapter particle tracking in a simple 2D geometry is done using the Van Leer finite difference scheme. The results obtained serve as a reference for the finite element implementation in VIp. Further the simulation of filling a T-shaped cavity is compared with results obtained with INJECT-3, in which the particle tracking is carried out using an Euler explicit upwind scheme.

5.1 Particle tracking in 2D

The influence of the type of front model on particle tracking is studied by the simulation of the isothermal filling of a end-gated rectangular cavity (figure 5.1) with a Newtonian fluid. The problem can be simplified to 2D, since the main flow is unidirectionally. The velocity $v_x(z)$, which is independent

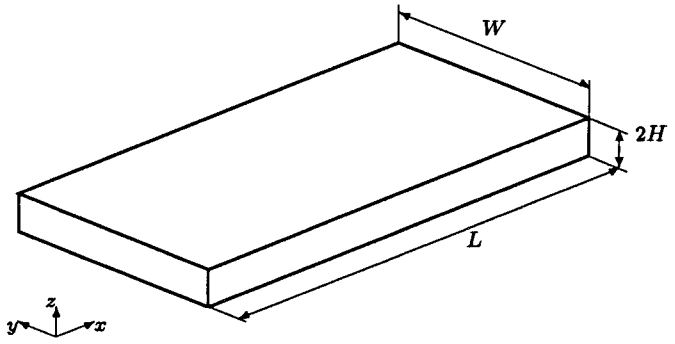

Figure 5.1: Mould geometry of the rectangular strip

of time and position, is given by:

$$v_x(z) = \frac{3}{2} v_0 \left(1 - \frac{z^2}{H^2}\right) \tag{5.1}$$

where v_0 is the gap-averaged velocity. Particle tracking is done by means of the Van Leer finite difference scheme. The x-z plane is discretized using n gridlines and m gridlevels for the x, z direction respectively, both equally spaced. The time steps taken are related to the gridline spacing Δx by: $\Delta t = \Delta x / v_0$. For that reason, the flow front position is moved one gridline every time step. To enforce numerical stability when using the Van Leer scheme, the convection of the label field is carried out in 2 steps, so that the maximum Courant number is equal to 0.75. In this problem, the particle identity is represented by the starting time and position (t_0, z_0) when entering the mould cavity. Using either the simplified front model or the parametrized version of the Bhattacharji and Savic model, the convection problem can be reduced further to 1D, since the label values at different gridlevels are coupled at the front region only.

The cavity dimensions are $L \times W \times 2H = 300 \times 75 \times 2\ mm^3$. The mould is filled in $t_{fill} = 1s$ with timesteps of $\Delta t = 1/150$. The average velocity is $v_0 = 300mm/s$ and the gridlevels are spaced with $\Delta z = 1/40$. For the calculations the following dimensionless variables are used: $x^* = x/L$, $z^* = z/H$, $v_x^*(z^*) = v_x/v_0$, and $t^* = t/t_{fill}$. Because of symmetry, only one mould half is considered.

The need of a finite difference scheme that is able to convect steep gradients in the solution field may be clear of figure 5.2. In this figure, the t^*- and the z^*-label values on a certain gridlevel above the folding line z_f are plotted, clearly demonstrating the presence of steep gradients in the solution. In this

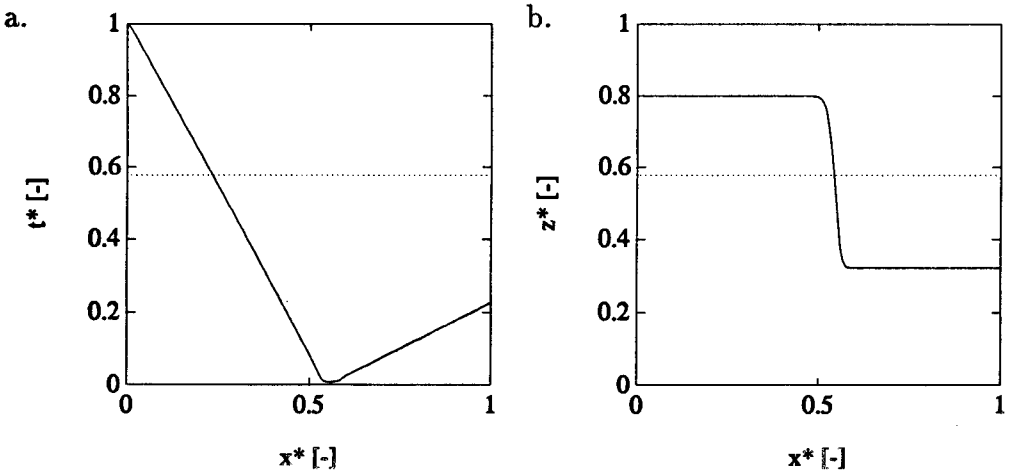

Figure 5.2: Label values on gridlevel $z^* = 0.8$, t^*-labels (a) and z^*-labels (b). Dashed line represents the folding line.

figure, the influence of the numerical diffusion of the Van Leer scheme can be seen by the smoothing of the sharp transitions in the label fields.

The residence time distribution for filling the mould is plotted in figure 5.3 for both front models. The curve for the maximum residence time $t^* = 1$ is

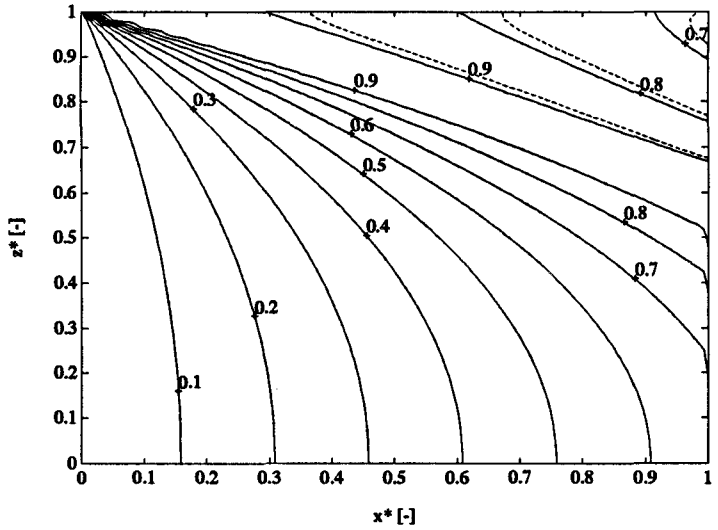

Figure 5.3: Residence time distribution in filling a mould. Full line: simplified front model, dashed line: Bhattacharji and Savic front model

not shown in the figure, because that value is get lost due to the numerical diffusion introduced by the Van Leer scheme ($t^*_{max} = 0.98$). Normally, this envelope is situated between the curves with $t^* = 0.9$ and starts at $(x^*, z^*) = (0, 1)$ and ends at $(x^*, z^*) = (1, 1/\sqrt{3})$. Particles below this line of maximal residence time have never reached the flow front, whereas particles above it have experienced the fountain flow. It is obvious that the difference between the two models only occurs in the area above that envelope.

The use of the conservation of identity method in simulating the multilayer injection moulding process is demonstrated in figure 5.4. In figure 5.4a a specific layer distribution is indicated to produce a multilayer product. The corresponding injection sequence is given in figure 5.4b, where the z^*-label values are plotted against the t^*-label values. For instance, this plot can be used for programming the injection moulding units for injecting the two components. The injection sequence obtained with the simplified front model differs not much from the one obtained with the Bhattacharji and Savic model. Therefore, it can be concluded that the simplified front model is accurate enough for this application. However, for processes where the residence time plays an important role, e.g. in the reactive injection moulding, the Bhattacharji model has to be used (Castro and Macosko [12]).

5.2 Multilayer injection moulding

In the numerical simulation of the multilayer injection injection moulding process the midplane is discretized by a FEM mesh for solving the impuls

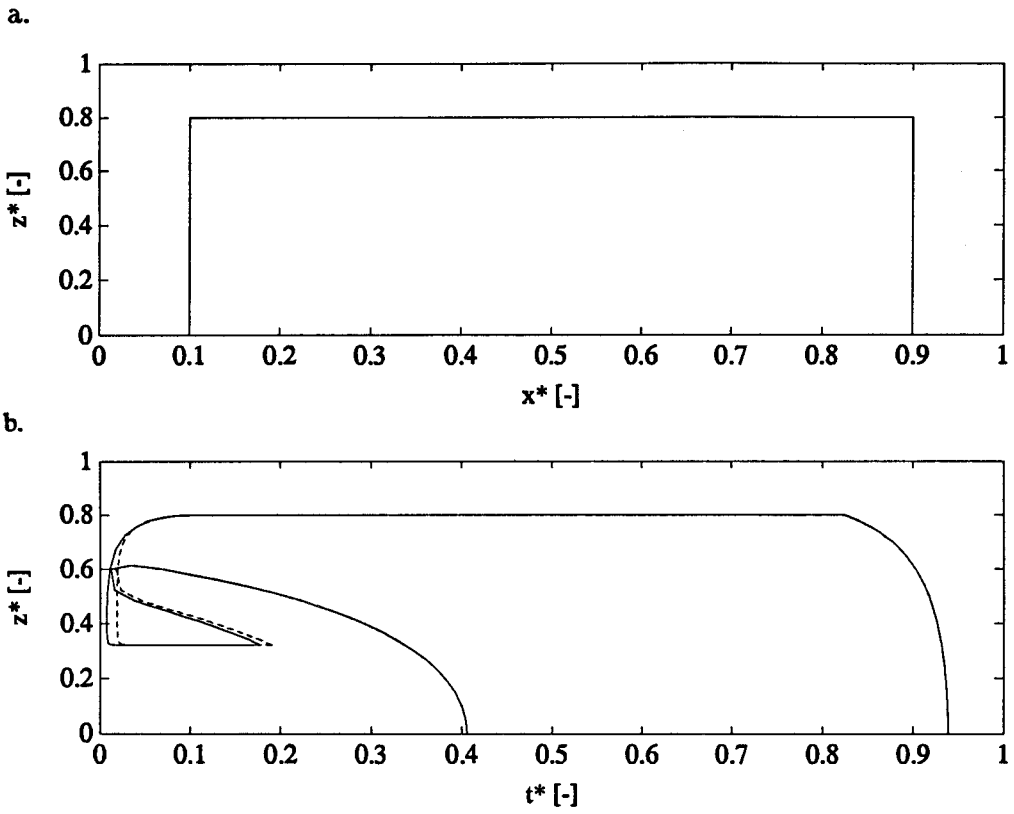

Figure 5.4: Specific layer distribution of a multilayer product. Desired layer distribution (a) and corresponding injection sequence (b). Full line: Bhattacharji and Savic front model, dashed line: simplified front model

equation and a FDM grid is used for the calculation of the energy equation in the thickness direction ($2\frac{1}{2}$D approach). During the simulation, the gridspacing of the FDM grid is altered in such a way that the number of gridpoints in the fluid and in the solid layer are kept constant. In this way, the gripoints with the same gridnumber form a plane in which the convection equation can be solved. Therefore, the spatial dimension of the particle tracking problem is reduced to 2D. The particle tracking procedure is implemented in VIp, a FEM based program for simulating moulding processes. Therefore the conservation of identity equation is solved using the Bubnow-Galerkin FEM. The Euler implicit time integration is used, because this schemes is unconditionally stable and less dispersive than the Crank-Nicholson method.

First, the isothermal filling of the rectangular strip (figure 5.1) with a non-Newtonian polymer melt is simulated. The particle identity is again defined by the starting position and time (t_0, y_0, z_0) when entering the mould cavity. The convection problem is solved using a 2×20 mesh of bilinear rectangular elements while the thickness direction is divided into 21 gridlevels.

The fountain phenomena is modeled with the simplified front model. Figure 5.5 shows the label values at a gridlevel above the folding line. A small

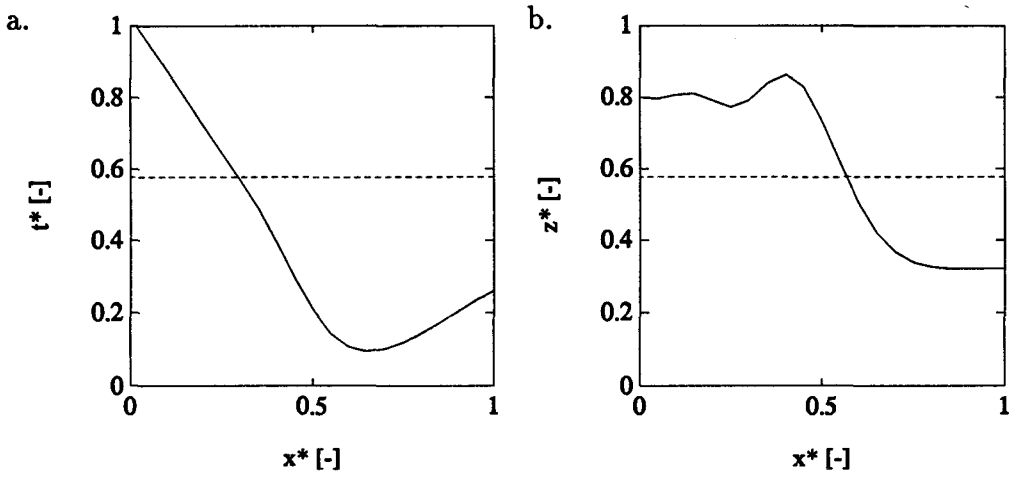

Figure 5.5: Label values at gridlevel $z = 0.8$, t^*-labels (a) and z^*-labels (b)

oscillation can be seen in the neighbourhood of the discontinuity in the z-label values. Due to the numerical diffusion introduced by the Euler implicit scheme the t-label values close to the sharp transition is much more smoothed when compared with figure 5.2a. In figure 5.6 the z^*-label values are plotted against the t^*-label values for the same specific layer distribution as shown in figure 5.4a. This plot clearly shows the influence of the numerical diffusion

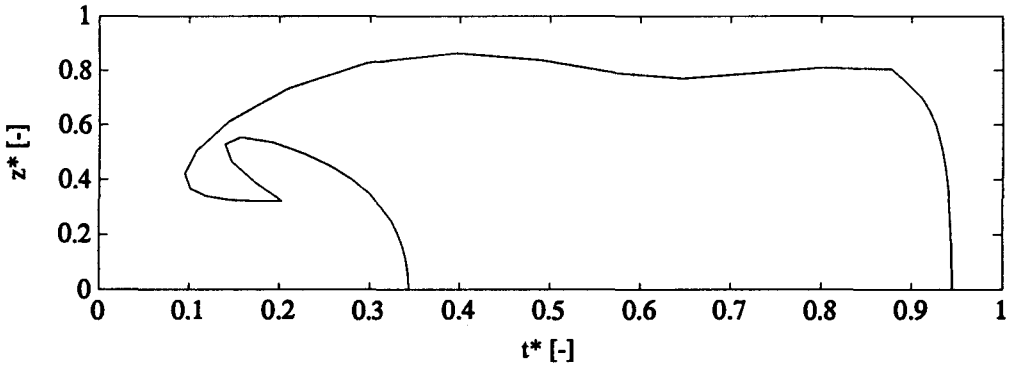

Figure 5.6: Injection sequence for producing a multilayer product

on the calculated injection sequence (compare with figure 5.4).

In appendix D more results can be found. The y-label distribution in the midplane of the product is plotted in figure D.1. Due to oscillations the maximum y-label value is somewhat larger than the maximum y-coordinate. Finally, in figure D.2 in appendix D the time-labels at the mould wall are plotted. This figure gives information when breakthrough of a second com-

ponent in sequential injection occurs. In this case the second component may be injected after $0.263s$ to avoid breakthrough of that component.

The last example is the isothermal filling of a T-shaped strip. The geometry of the T-strip is plotted in 5.7. The results can be found in appendix D.

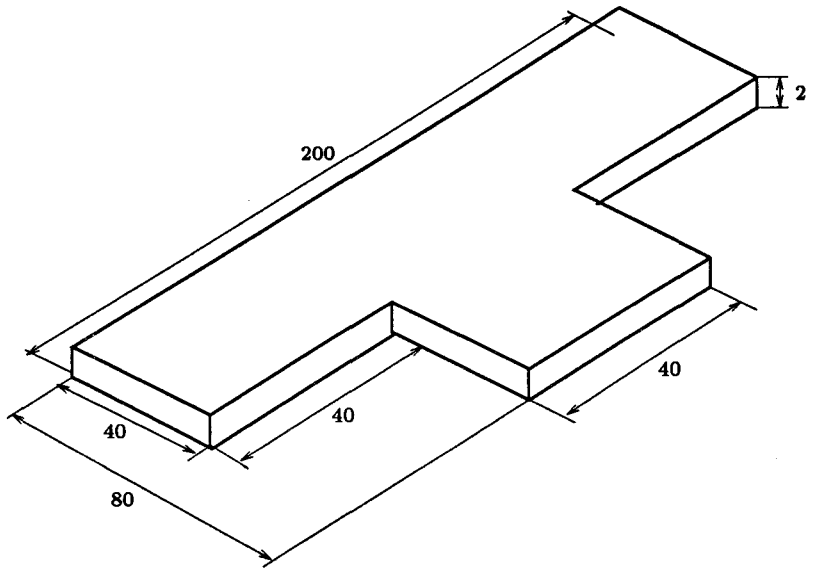

Figure 5.7: Mould geometry of the T-strip

The t- and the y-labels in the midplane are plotted for different percentages of filling: 50, 60, 70, 80, 90, and 100%. The same example was used by Van der Velden [58], who applied a first order upwind scheme with Euler explicit time integration. The results agree well with those of Van der Velden [58], in spite of some oscillations that occur. When using the Galerkin FEM, they appear first when the fluid reaches the corner of the side part of the cavity.

Chapter 6

Conclusions and recommendations

In this report, the multilayer injection moulding process is modeled in order to predict the injection sequence or configuration needed for producing a product with a specific layer distribution for one component only. The simulation of the flow in thin-walled products is established using the $2\frac{1}{2}$D approach. To predict the layer distribution in a product the flow history of material elements has to be known. For that purpose, a particle tracking procedure is developed based on the conservation of identity of the particles. Particles are labeled when they enter the mould with their identity. During the flow in the mould the identity does not change, hence the the particle tracking problem can be modeled with a conservation law of the form of a scalar convection equation. This equation can be solved with several FDM or FEM techniques. Besides the accurate solution of the particle tracking, also the material behaviour has to be known well. Linear and non-linear viscoelastic measurements are carried out to characterize the rheological behaviour of two amorphous melts. The predictive quality of two non-linear viscoelastic models, the Wagner and Leonov model, is tested using the experimental results.

Conclusions

The modeling of the particle tracking with the conservation of identity method proves to be flexible and requires much less storage capacity compared with the path-reconstruction method. The label distribution at the moving flow front can be modeled adequately using either the Bhattacharji and Savic or the simplified model. For the purpose in multilayer injection moulding, the simplified front model, which neglects the residence time in the front region, is accurate enough. Due to the label redistribution at the flow front, steep gradients occur in the label solution fields. For that reason, numerical

schemes has to be found which are able to convect solutions with discontinuities or steep gradients. From the finite difference schemes tested, the Van Leer scheme proves to give the best results, although the numerical diffusion introduced by the scheme is considerable when used on a coarse grid. The Galerkin FEM with a Crank-Nicholson time integration is used for solving the particle tracking problem in the injection moulding simulation. In spite of oscillations introduced by this numerical scheme, the results are promising.

In the characterization of the visco-elastic material behaviour, special attention is paid to the determination of the relaxation spectrum of a polymer material. Fitting a discrete spectrum to the data of the storage and loss moduli proved to be ill-posed. With a non-linear regression technique often non-physical negative relaxation strengths and/or times occur. The Bayesian estimation procedure used, is rather robust and the so obtained spectrum fits the linear viscoelastic experiments quite well. However, in describing the start-up and cessation after steady shear flow experiments the model predictions deviates considerably from the experimental results, especially in the case of the relatively small shear rates. Extension of the discrete relaxation spectrum with longer relaxation times will improve the model predictions. The mathematical best fit gives in this case a rather poor fysical fit.

Recommendations

The study described in this report gives rise to the following recommendations for future research:

- The particle tracking procedure implemented in VIP, a programm for simulation of moulding processes, has to be improved by using a FEM-technique more capable of convecting solution with discontinuities or steep gradients than the Galerkin FEM. The SUPG, TD/GLS and TG/DFEM are possible alternatives.
- The particle tracking in $2\frac{1}{2}$D-geometries has to be extended for use with products with bifurcations or changing wall-thicknesses. At this moment, it is possible that at different positions in the product the same identity labels are present, because no special treatment in above mentioned cases is implemented.
- The simulation of the filling of a multilayer product has to be extended to handle the flow of different materials in one mould cavity.
- For the simulation of the injection of reactive materials, the Bhattacharji and Savic fountain flow model has to be implemented in VIp.
- Post-processing procedures are needed for representing the results – injection sequence or configuration – for $2\frac{1}{2}$D geometries. Also, the results have to be translated to injection conditions for controlling the

multilayer injection moulding machine.

- The simulated results should be compared with results carried out on a multilayer injection moulding machine.
- To avoid extrapolation of the time or frequency domain when using a viscoelastic model in the injection moulding simulation, experiments in the high shear rate region has to be carried out.
- Checking the validity of the decoupled approach in viscoelastic calculations.

Appendix A

Fountain flow model of Bhattacharji and Savic

The analytical solution of the 2D fountain flow is derived by assuming that:

- the fluid behaves Newtonian and is incompressible.
- the contact angle at the wall is 90° and the front is flat.
- there is no wall-slip except at the moving contact line.
- the inertia terms can be neglected.
- the conservation of momentum can be considered to be quasi-stationary.

With the origin positioned at the free surface, the problem can be formulated by:

$$\vec{\nabla}^4 \psi = 0 \tag{A.1}$$

with the boundary conditions:

$$\begin{aligned}
v_x &= \bar{v}_x && \text{for } z = H/2,\ x > 0 \\
v_x &= 0 && \text{for } x = 0 \\
v_z &= 0 && \text{for } z = H/2 \\
\frac{\partial v_x}{\partial z} &= 0 && \text{for } z = 0 \\
\frac{\partial v_z}{\partial x} &= 0 && \text{for } x = 0
\end{aligned}$$

where H is the gap-height of a rectangular channel. The streamfunction ψ is defined by:

$$v_x = -\frac{\partial \psi}{\partial z} \qquad v_z = \frac{\partial \psi}{\partial x} \tag{A.2}$$

Integrating (A.1) analytically and simplifying the expression for ψ so obtained, gives the following formulas for the velocity components behind an

advancing front ([12]):

$$v_x(x,z) = -\bar{v}_x\left(\frac{1}{2} - 6\frac{z^2}{H^2}\right)\left[1 - 1.45e^{-5\frac{z}{H}}\sin(0.76 + 2\frac{x}{H})\right] +$$
$$-0.53\left(1 - 80\frac{z^4}{H^4}\right)\left[e^{-5\frac{z}{H}}\sin(2\frac{x}{H})\right] \quad \text{(A.3)}$$

$$v_z(x,z) = \bar{v}_x\frac{z}{H}\left(1 - 4\frac{z^2}{H^2}\right)\left[3.63e^{-5\frac{z}{H}}\sin(0.76 + 2\frac{x}{H})\right.$$
$$\left.-1.45e^{-5\frac{z}{H}}\cos(0.76 + 2\frac{x}{H})\right] \quad \text{(A.4)}$$
$$-2\frac{z}{H}\left(1 - 16\frac{z^4}{H^4}\right)\left[1.32e^{-5\frac{z}{H}}\sin(2\frac{x}{H}) - 0.53e^{-5\frac{z}{H}}\cos(2\frac{x}{H})\right]$$

The particles in the front region can be tracked by integrating the velocity field using a Runga-Kutta integration technique. The flow paths can be constructed for a specific residence time of the particle in the fountain region. In this way, two relations can be derived that give the residence time in the front and the position of inflow as a function of the position of outflow of the fountain region. The relations are fitted with a 6th order polynomial ([58]):

$$z_i^*(z_o^*) = \sum_{i=0}^{6} a_i z_o^{*i}$$
$$t_r^*(z_o) = \sum_{i=0}^{6} b_i z_o^{*i}$$

The coordinates are made dimensionless by $z_i^* = z_i/2H$ and $z_o^* = z_o/2H$ and the residence time by $t_r^* = \frac{t_r \bar{v}_x}{H}$. The parameters a_i and b_i are:

i	a	b
0	4.377	76324.9
1	-25.336	-576340.5
2	74.619	1810274.2
3	-118.676	-3025308.9
4	103.284	2836063.3
5	-46.599	-1413695.4
6	8.330	292695.3

The results of the fit can be found in figure 2.6.

Appendix B

Expressions of non-linear shear flow experiments for Wagner and Leonov model

The expressions that describe the non-linear shear flow experiments presented in section 3.1.2 are summarized in this appendix for the Wagner and the Leonov models. The expressions for the Wagner model are derived using the single exponential damping function. The derivation of these expressions with the double exponential damping funtion proceeds in the same way, because $\sigma_{12}(t) = f_1\sigma_{12}(t, n_1) + f_2\sigma_{12}(t, n_2)$. For the Leonov the components of the Finger tensor $\bar{\mathbf{B}}_{ei}$ will be given.

Step strain stress relaxation

Wagner model

Using (3.13) the expression for the relaxation modulus reads (Laun [36]):

$$G(t, \gamma_0) = e^{-n\gamma_0} \sum_{i=1}^{N} G_i e^{-\frac{t+\Delta t}{\theta_i}} \left[1 + \frac{\Delta t}{2\theta_i} + \frac{\Delta t}{\theta_i} \sum_{k=3}^{\infty} \frac{1}{k!} (\frac{\Delta t}{\theta_i} + n\gamma_0)^{k-2}\right] \quad \text{(B.1)}$$

Leonov model

With the initial conditions:

$$\bar{B}_{11i}(0) = 1 + \dot{\gamma}^2\Delta t^2 = 1 + \gamma_0^2$$
$$\bar{B}_{12i}(0) = \dot{\gamma}\Delta t = \gamma_0$$
$$\bar{B}_{22i}(0) = 1$$

the expression for the relaxation modulus reads ($\Delta t \rightarrow 0$):

$$G(t, \gamma_0) = \sum_{i=1}^{N} \frac{\eta_i}{\theta_i} \frac{4e^{-t/\theta_i}}{4 + \gamma_0^2(1 - e^{-2t/\theta_i})} \quad \text{(B.2)}$$

Stress growth at constant shear rate

Wagner model

The transient viscosity and primary normal stress coefficient can be expressed by:

$$\eta^+(t,\dot{\gamma}_0) = \sum_{i=1}^{N} \frac{G_i\theta_i}{(1+n\dot{\gamma}_0\theta_i)^2}\left[1 - e^{-t_{r,i}}(1 - n\dot{\gamma}_0\theta_i t_{r,i})\right] \tag{B.3}$$

$$\psi^+(t,\dot{\gamma}_0) = 2\sum_{i=1}^{N} \frac{G_i\theta_i^2}{(1+n\dot{\gamma}_0\theta_i)^3}\left[1 - e^{-t_{r,i}}(1 + t_{r,i} - \frac{n\dot{\gamma}_0\theta_i}{2}t_{r,i}^2)\right] \tag{B.4}$$

with the reduced time $t_{r,i} = t(1/\theta_i + n\dot{\gamma}_0)$. The expression for the steady state viscosity can be derived easily by substituting $t_{r,i} \gg 1$ in the above given equation for η^+.

Leonov model

For shear flow, the transient viscosity and primary normal stress coefficient are given by:

$$\eta(t,\dot{\gamma}_0) = \eta_r + \frac{1}{\dot{\gamma}_0}\sum_{i=1}^{N}\frac{\eta_i}{\theta_i}\bar{B}_{12i} \tag{B.5}$$

$$\psi(t,\dot{\gamma}_0) = \frac{1}{\dot{\gamma}_0^2}\sum_{i=1}^{N}\frac{\eta_i}{\theta_i}(\bar{B}_{11i} - \bar{B}_{22i}) \tag{B.6}$$

The components of the Finger tensor has to determined numerically by solving the following set of equations:

$$\dot{\bar{B}}_{11i} = 2\dot{\gamma}_0\bar{B}_{12i} - \frac{1}{2\theta_i}(\bar{B}_{11i}^2 + \bar{B}_{12i}^2 - 1) \tag{B.7}$$

$$\dot{\bar{B}}_{12i} = \dot{\gamma}_0\bar{B}_{22i} - \frac{1}{2\theta_i}(\bar{B}_{11i} + \bar{B}_{22i})\bar{B}_{12i} \tag{B.8}$$

$$\bar{B}_{11i}\bar{B}_{22i} - \bar{B}_{12i}^2 = 1 \tag{B.9}$$

with the initial conditions:$\bar{B}_{11i}(0) = \bar{B}_{22i}(0) = 1$ and $\bar{B}_{12i}(0) = 0$.

Stress relaxation after cessation of steady shearing flow

Wagner model

The transient viscosity and primary normal stress coefficient for this type of experiment are given by:

$$\eta^-(t,\dot{\gamma}_0) = \sum_{i=1}^{N}\frac{G_i\theta_i}{(1+n\dot{\gamma}_0\theta_i)^2}e^{-t/\theta_i} \tag{B.10}$$

$$\psi^-(t,\dot{\gamma}_0) = 2\sum_{i=1}^{N}\frac{G_i\theta_i^2}{(1+n\dot{\gamma}_0\theta_i)^3}e^{-t/\theta_i} \tag{B.11}$$

Leonov model

For the cessation after steady shearing analytical expressions for the components of the Finger tensor are derived by Upadhyay [57]:

$$\bar{B}_{12i} = \frac{4\beta_i e^{-t/\theta_i}}{(1-\beta_i^2 e^{-2t/\theta_i})\sqrt{\alpha_i^2+4}} \tag{B.12}$$

$$\bar{B}_{11i} - \bar{B}_{22i} = \frac{4\alpha_i\beta_i e^{-t/\theta_i}}{(1-\beta_i^2 e^{-2t/\theta_i})\sqrt{\alpha_i^2+4}} \tag{B.13}$$

with

$$\alpha_i = \frac{\bar{B}_{11i}(0) - \bar{B}_{22i}(0)}{\bar{B}_{12i}(0)} \qquad \beta_i = \sqrt{\frac{\bar{B}_{11i}(0) + \bar{B}_{22i}(0) - 2}{\bar{B}_{11i}(0) + \bar{B}_{22i}(0) + 2}} \tag{B.14}$$

The initial conditions are the steady state values given by:

$$\bar{B}_{11i}(0) = \frac{\sqrt{2}X_i}{\sqrt{1+X_i}}, \quad \bar{B}_{12i}(0) = \frac{2\dot{\gamma}_i\theta_i}{1+X_i}, \quad \bar{B}_{22i}(0) = \frac{\sqrt{2}}{\sqrt{1+X_i}} \tag{B.15}$$

Substituting the components of the Finger tensor in the equations (B.5) and (B.6) gives the relations for η^- and ψ^- respectively.

Appendix C

Prediction Wagner model with extended spectrum

In order to improve the predictive behaviour of the Wagner model for the cessation of steady shear flow experiments, a relaxation spectrum with a larger number of relaxation times (N=12) is used. The spectrum is fitted with the Levenberg-Marquardt method, because the maximum relaxation time fitted with the Bayesian estimation method is too low the describe this type of experiment accurately enough. However, the confidence intervals of most of the parameters are larger than the parameter values itself and also the square error is much larger: 0.00479 for the Bayesin method and 0.112 for the Levenberg-Marquardt method. The number of modes is about $1\frac{1}{2}$ per decade. The parameter values are summarized in table C.1. The results for the cessation of steady shear flow experiment are plotted in figure C.1 and C.2. The model predictions using this relaxation spectrum is much better than the results presented in figure 3.19 and 3.20. Also the start-up shear flow experiment is desribed much better with this spectrum (see figure C.3). The other non-linear shear flow experiments can also be predicted more accurate using this spectrum. Of course, the model predictions with the Leonov model can be improved in the same way.

Wagner	
θ_i s	G_i Pas
$7.659 \cdot 10^{-7}$	$1.433 \cdot 10^{6}$
$1.011 \cdot 10^{-6}$	$6.189 \cdot 10^{5}$
$2.908 \cdot 10^{-6}$	$2.934 \cdot 10^{5}$
$1.699 \cdot 10^{-5}$	$1.558 \cdot 10^{5}$
$3.328 \cdot 10^{-4}$	$9.455 \cdot 10^{4}$
$1.516 \cdot 10^{-3}$	$6.743 \cdot 10^{4}$
$6.579 \cdot 10^{-3}$	$5.077 \cdot 10^{4}$
$2.848 \cdot 10^{-2}$	$3.593 \cdot 10^{4}$
$1.233 \cdot 10^{-1}$	$1.970 \cdot 10^{4}$
$5.337 \cdot 10^{-1}$	$7.245 \cdot 10^{3}$
$2.310 \cdot 10^{0}$	$1.524 \cdot 10^{3}$
$1.000 \cdot 10^{1}$	$1.890 \cdot 10^{2}$

Table C.1: Linear viscoelastic parameters PS Styron 678E at $T = 462$K, fitted with Levenberg-Marquardt method

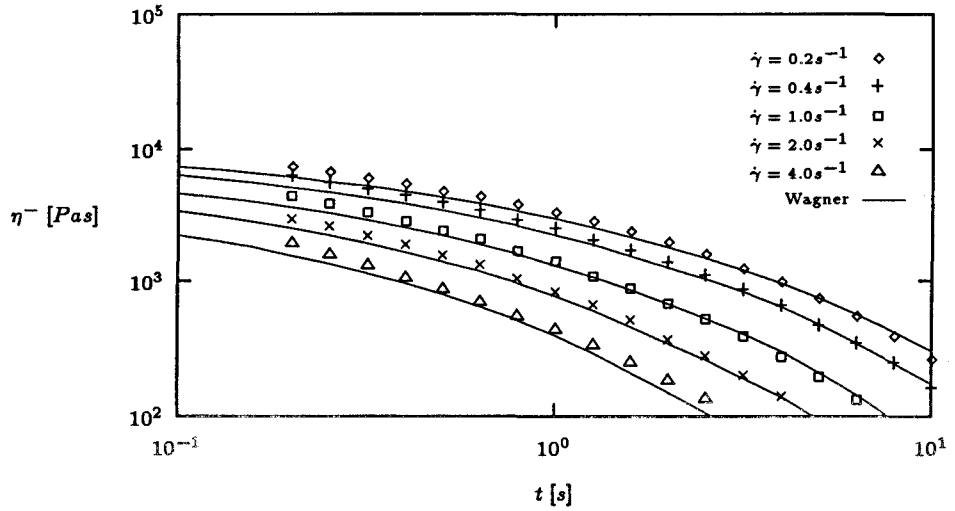

Figure C.1: Transient viscosity for PS Styron 678E for stress relaxation after steady shear with shear reates of $\dot{\gamma}_0 = 0.2, 0.4, 1, 2$, and $4s^{-1}$ at $T = 462$K.

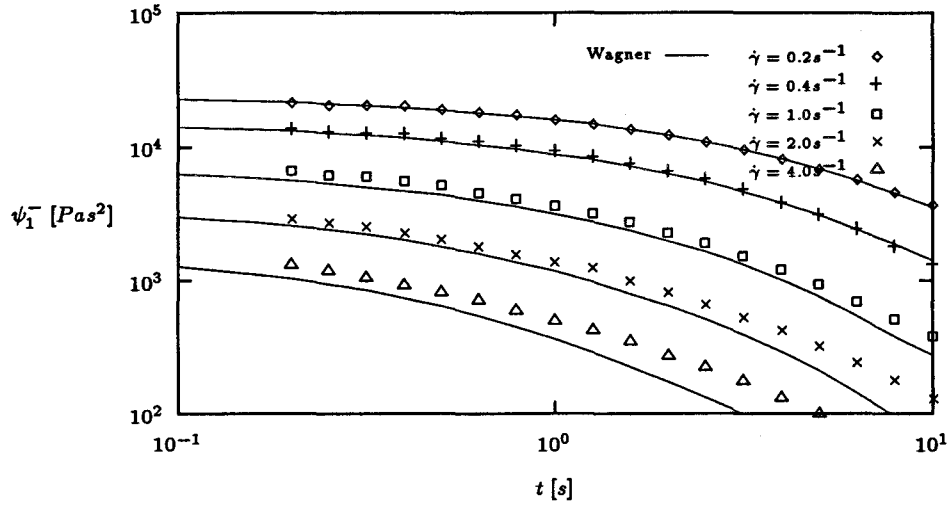

Figure C.2: Transient primary normal stress coefficient for PS Styron 678E for stress relaxation after steady shearing with shear reates: $\dot{\gamma}_0 = 0.2, 0.4, 1, 2,$ and $4s^{-1}$ at $T = 462$K.

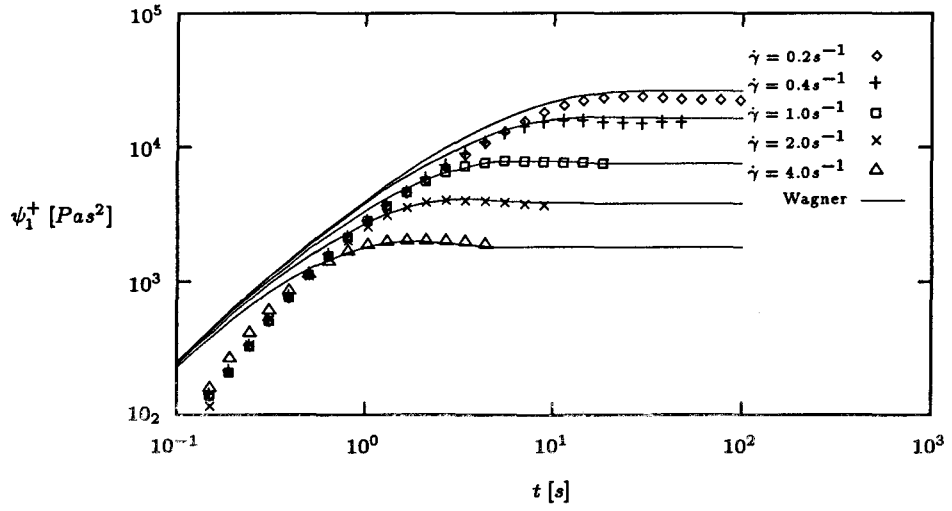

Figure C.3: Transient primary normal stress coefficient for PS Styron 678E for stress growth at constant shear rates of $\dot{\gamma}_0 = 0.2, 0.4, 1, 2,$ and $4s^{-1}$ at $T = 462$K.

Appendix D

Numerical simulations multilayer injection moulding process

For the numerical simulations of the multilayer injection moulding process the steady state viscosity is modeled by a 7-constant Cross model:

$$\eta(\dot{\gamma}, T, p) = \frac{\eta_0(T,p)}{1 + (\eta_0 \dot{\gamma}/\tau^*)^{1-n}} \tag{D.1}$$

with:

$$\eta_0(T,p) = D_1 \exp\left(\frac{-A_1(T - T^*)}{A_2 + T - T^*}\right)$$

$$T^*(p) = D_2 + D_3 p, \quad A_2(p) = \tilde{A}_2 + D_3 p$$

The parameters are listed in table D.1.

A_1		25.74
$\tilde{A}_2$	K	61.01
D_1	Pas	$4.76 \cdot 10^{10}$
D_2	K	373
D_3	K/Pa	$5.1 \cdot 10^{-7}$
n		0.25
τ^*	Pa	$3.08 \cdot 10^4$

Table D.1: Parameters in 7-constant Cross model for PS Styron 678E

The Tait equation is used to model the $p\nu T$-relation:

$$\nu(p,T) = (a_0 + a_1(T - T_g))\,(1 - 0.0894 \ln(1 + p/B)) \tag{D.2}$$

$$B(T) = B_0 e^{-B_1 T}, \quad T_g(p) = T_g(0) + sp$$

The parameters are given in table D.2. The thermal capacity is considered

a_0	m^3/kg	$9.72 \cdot 10^{-4}$
a_1	$m^3/(kgK)$	$5.4 \cdot 10^{-7}$
B_0	Pa	$2.5 \cdot 10^{8}$
B_1	C^{-1}	$4.1 \cdot 10^{-3}$
$T_g(0)$	K	373
s	K/Pa	$5.1 \cdot 10^{-7}$

Table D.2: Parameters in Tait equation for PS Styron 678E

to be constant $c_p = 2000\ J/(kgK)$ just as the thermal conductivity $\lambda = 0.16\ J/(m\,K)$.

The process conditions are:

		Rect. strip	T-strip
Q	m^3/s	$4.5 \cdot 10^{-5}$	$1.92 \cdot 10^{-5}$
T_{wall}	K	550	550
T_{inj}	K	550	550
$2H$	m	$2 \cdot 10^{-3}$	$2 \cdot 10^{-3}$

Results rectangular strip

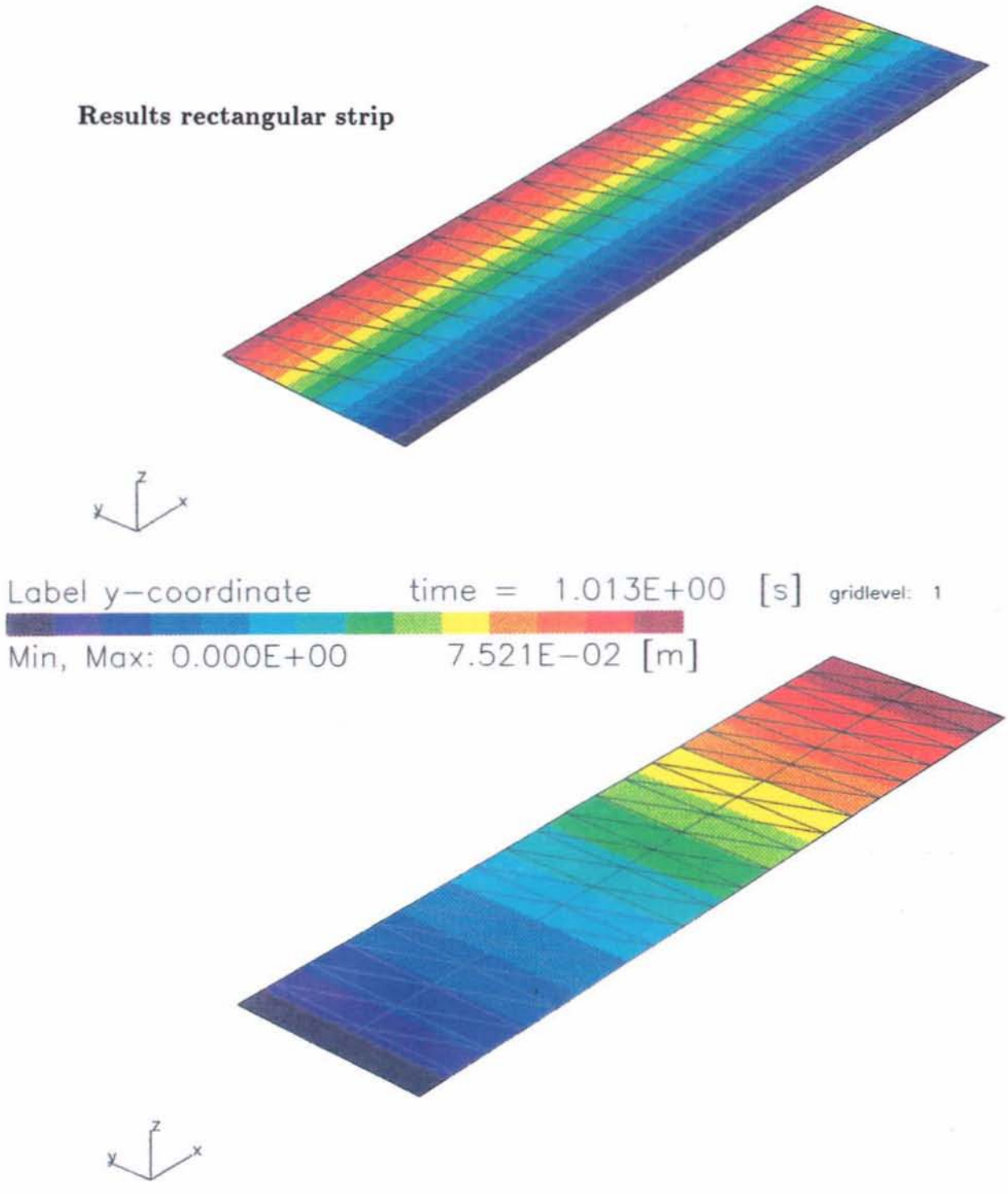

Figure D.1: Y-label distribution in midplane of cavity (above) and time-label distribution at the mould wall (below) at the end of filling.

Results T-shaped strip

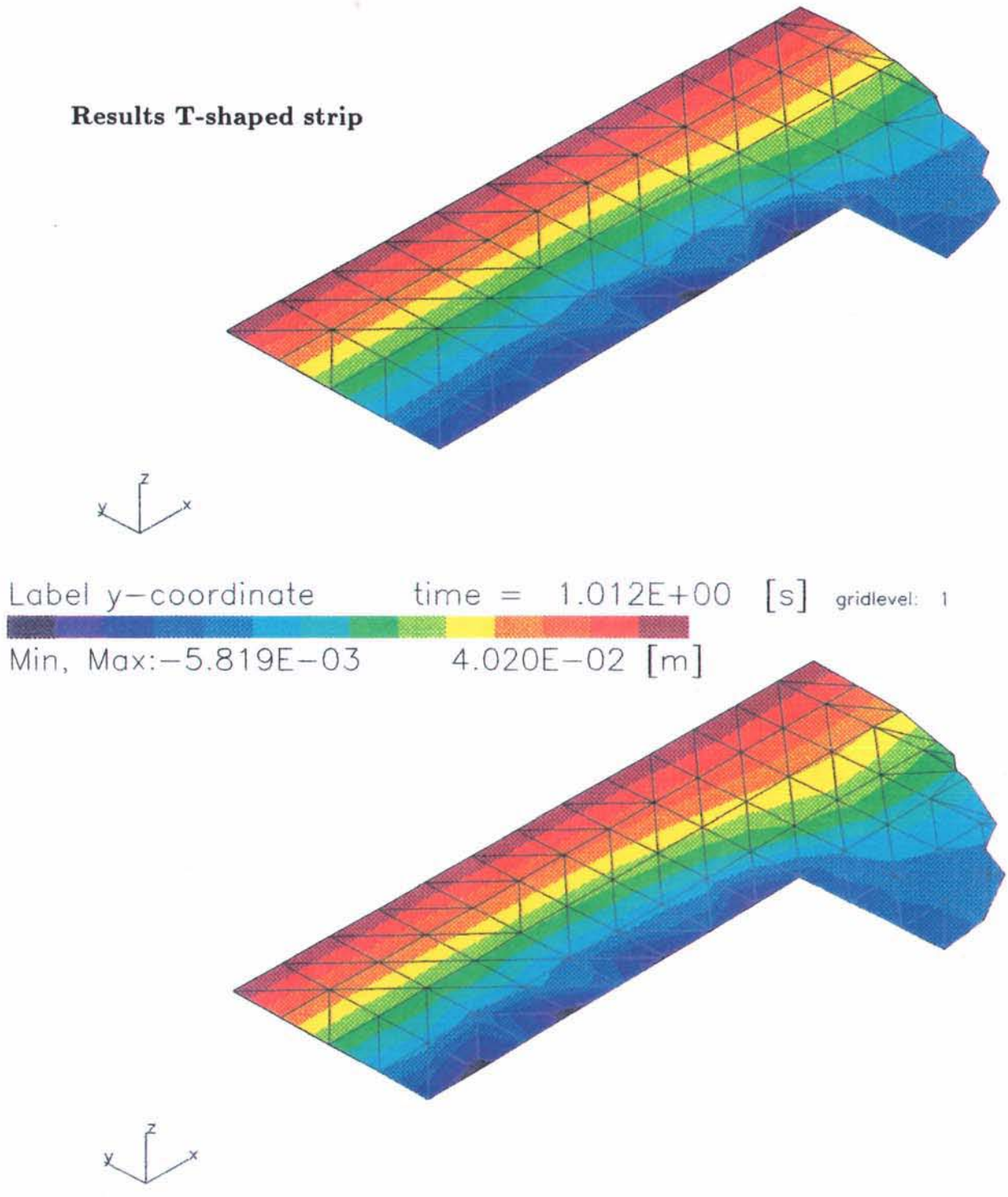

Figure D.2: Y-label distribution in midplane of cavity at 50% (above) and 60% (below) of the filling stage.

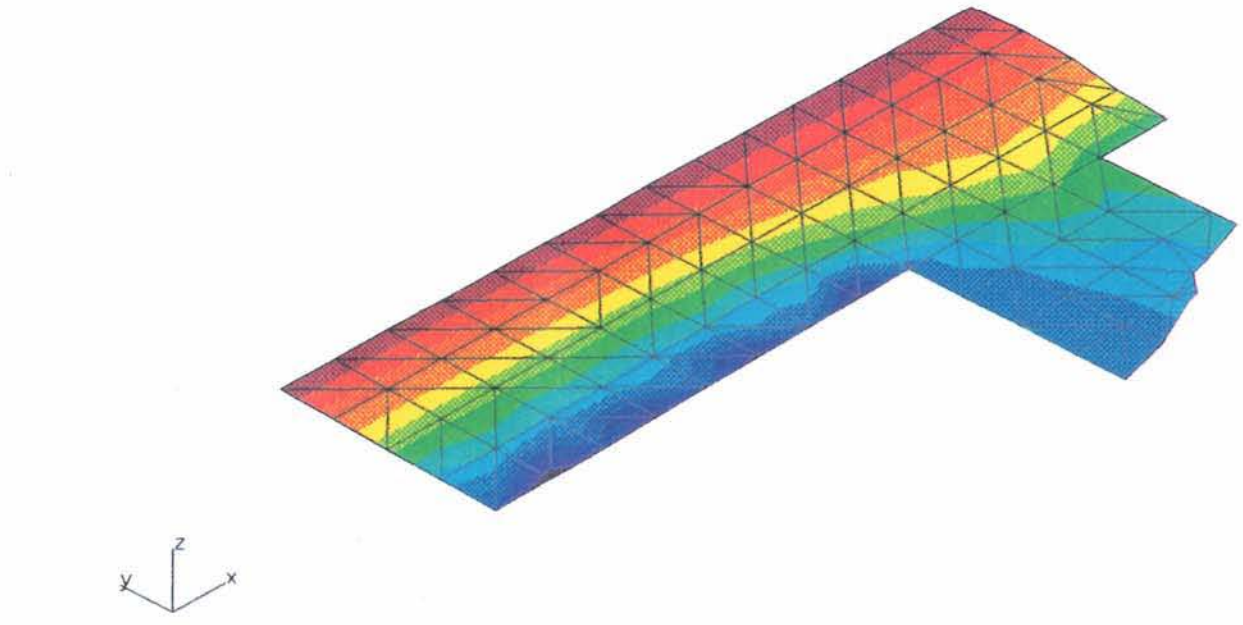

Figure D.3: Y-label distribution in midplane of cavity at 70% (above) and 80% (below) of the filling stage.

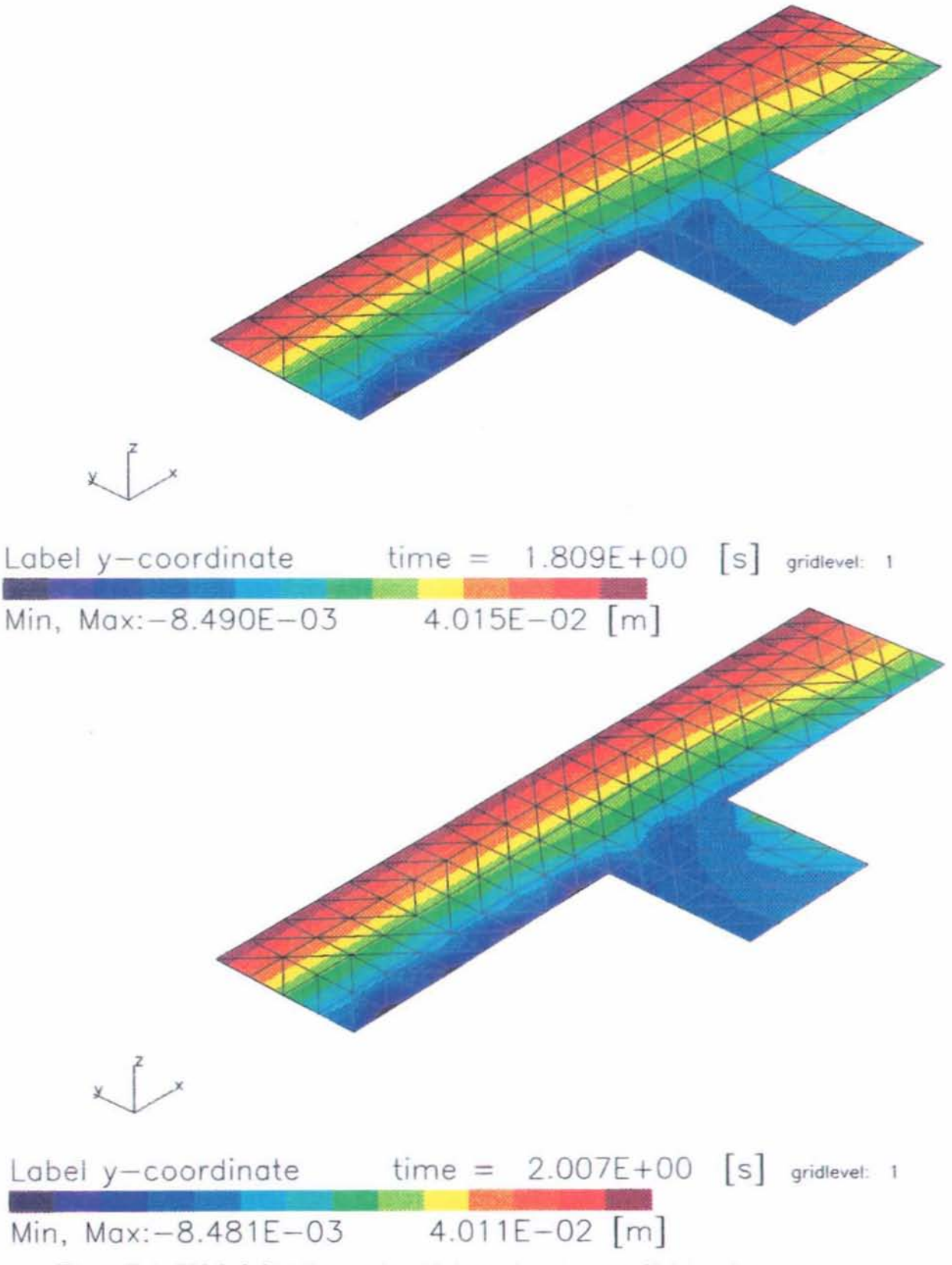

Figure D.4: Y-label distribution in midplane of cavity at 90% (above) and at the end (below) of the filling stage.

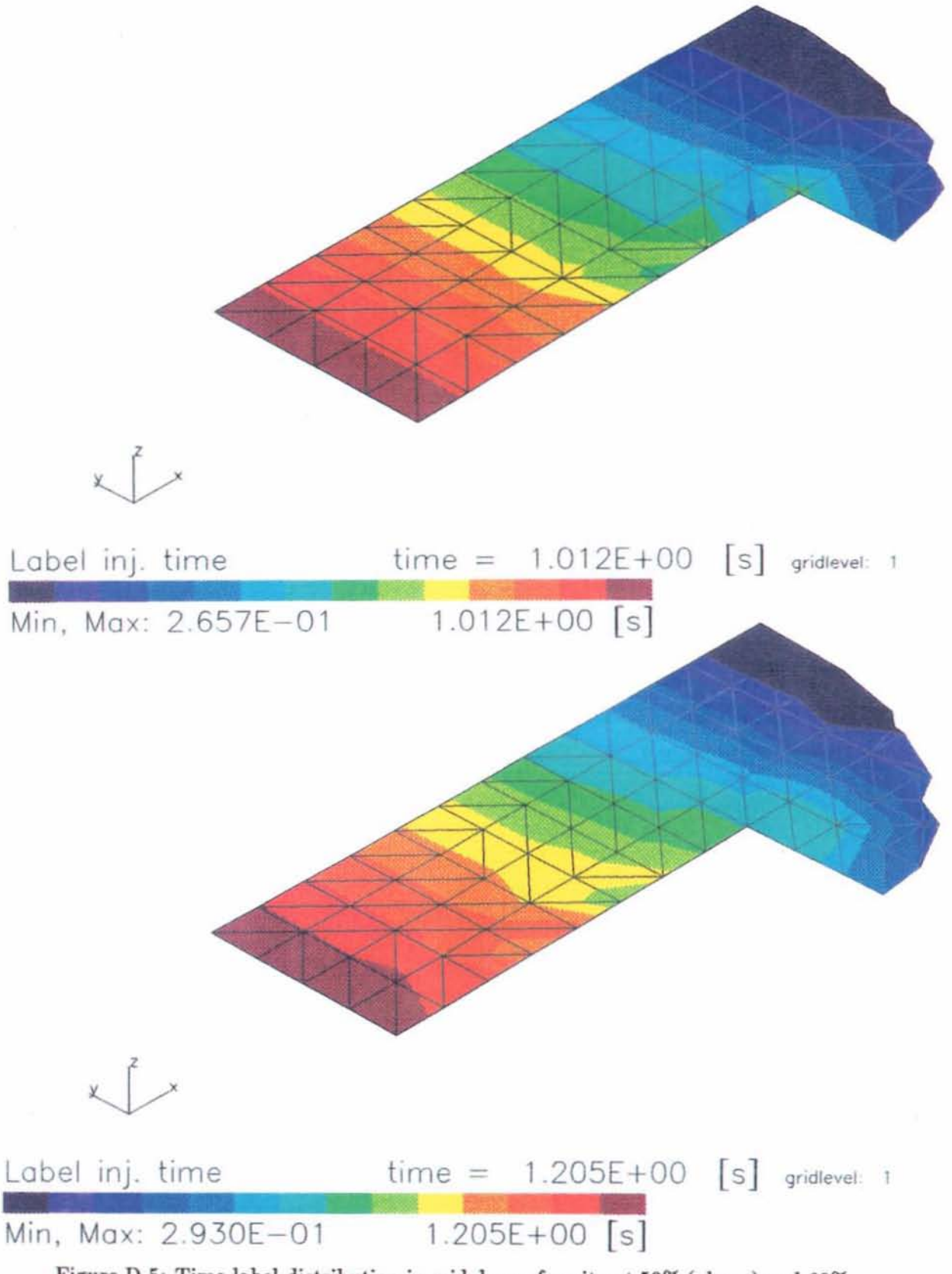

Figure D.5: Time-label distribution in midplane of cavity at 50% (above) and 60% (below) of the filling stage.

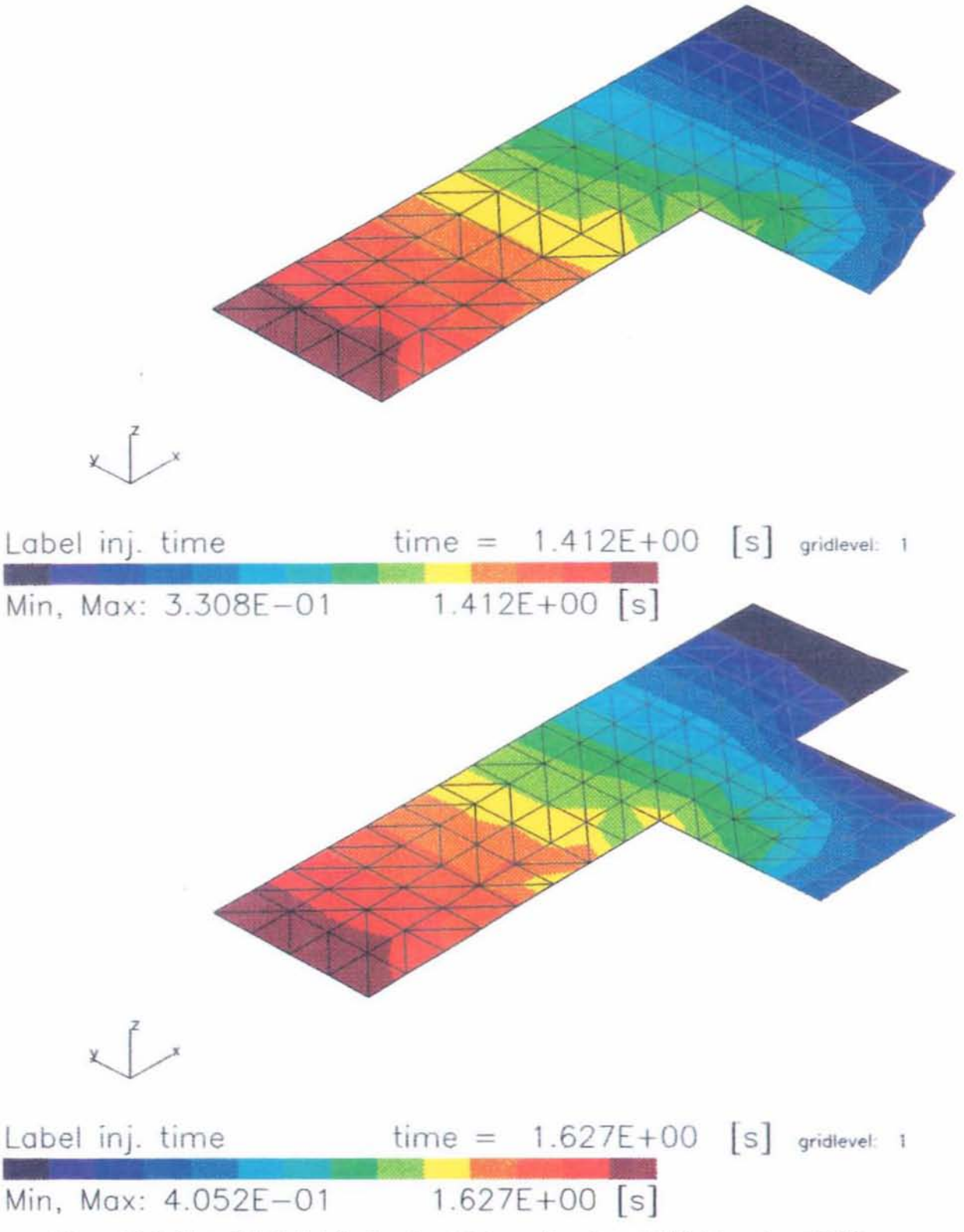

Figure D.6: Time-label distribution in midplane of cavity at 70% (above) and 80% (below) of the filling stage.

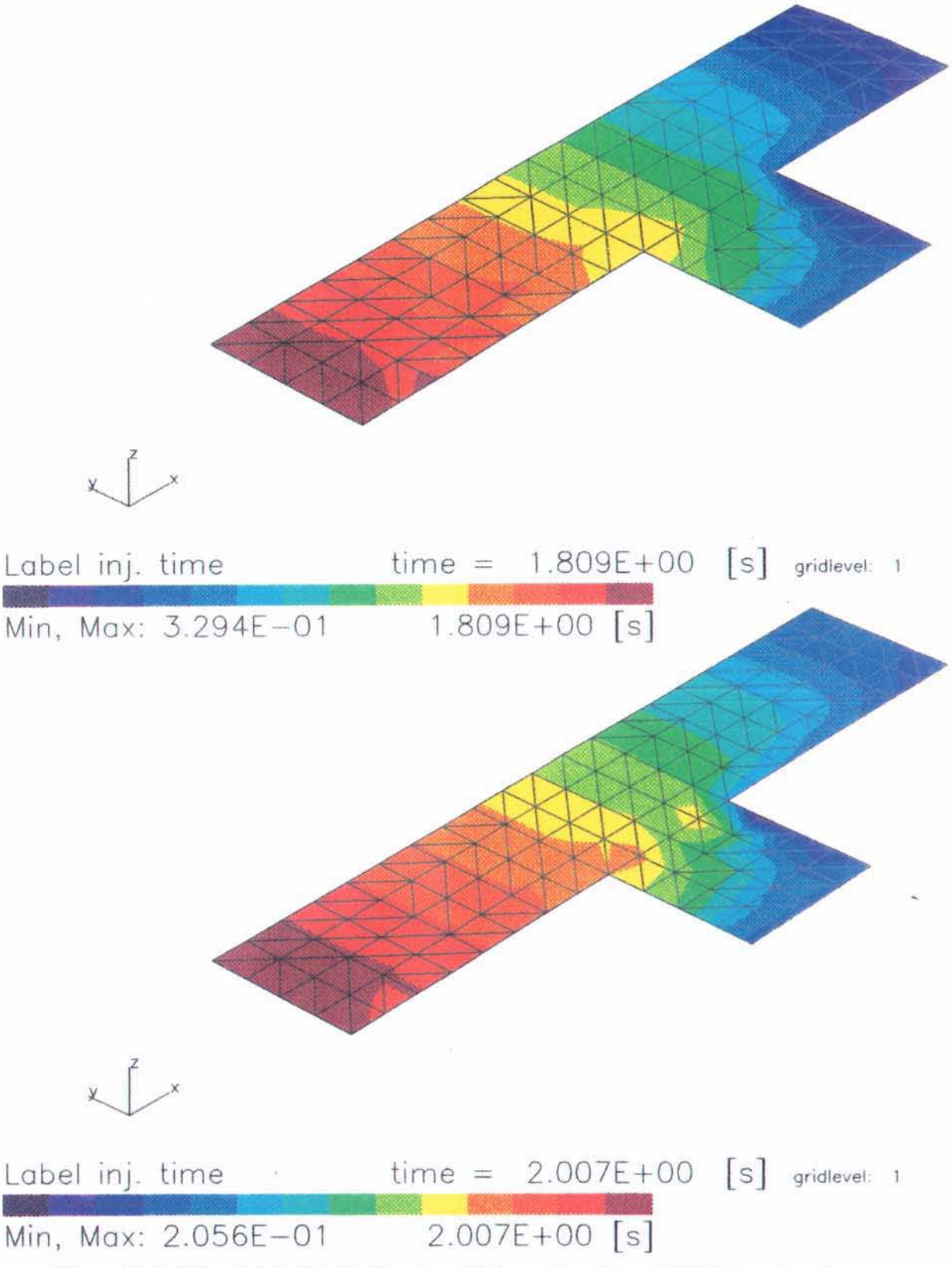

Figure D.7: Time-label distribution in midplane of cavity at 90% (above) and at the end (below) of the filling stage.

Bibliography

[1] F. P. T. Baaijens. A constitutive equation for compressible polymeric liquids. Philips Internal Report 311/87, Philips Research Laboratories, 1987.

[2] F. P. T. Baaijens. Applied computational mechanics 2, 1992.

[3] M. Baumgärtel and H. H. Winter. Determination of discrete relaxation and retardation time spectra from dynamic mechanical data. *Rheol. Acta*, 28:511–519, 1989.

[4] R. A. Behrens, M. J. Crochet, C. D. Denson, and A. B. Metzner. Transient free-surface flows: Motion of a fluid advancing in a tube. *AIChE. J.*, 33:1178–1168, 1987.

[5] B. Bernstein, E. A. Kearsley, and L. J. Zapas. A study of stress relaxation with finite strain. *Trans. Soc. Rheology*, 7:391–410, 1963.

[6] S. Bhattacharji and P. Savic. Real and apparent non-Newtonian behaviour in viscous pipe flow of suspensions driven by a fluid piston. In A. F. Charwat, editor, *Proc. 1965 Heat Transf. Fluid Mech. Inst.*, pages 248–262. Stanford University Press, 1965.

[7] R. B. Bird, W. E. Stewart, and E. N. Lightfoot. *Transport Phenomena.* John Wiley & Sons, New York, 1960.

[8] H. C. Booij and J. H. M. Palmen. Some aspects of linear and nonlinear viscoelastic behaviour of polymer melts in shear. *Rheol. Acta*, 21:376–387, 1982.

[9] A. H. M. Boshouwers and J. J. van der Werf. *Inject-3, A Simulation Code for the Filling Stage of the Injection Moulding Process of Thermoplastics.* PhD thesis, Eindhoven University of Technology, 1988.

[10] A. N. Brooks and T. J. R. Hughes. Streamline upwind/Petrov-Galerkin formulations for convection dominated flows with particular emphasis on the incompressible Navier-Stokes equations. *Computer Methods in Applied Mechanics and Engineering*, 32:199–259, 1982.

[11] L. W. Caspers. Calculation of trajectories in the numerical simulation of the injection moulding process. Master's thesis, Eindhoven University of Technology, 1991. (in Dutch).

[12] J. M. Castro and C. W. Macosko. Studies of moldfilling and curing in the reaction injection molding process. *AIChE. J.*, 28:250–260, 1982.

[13] K. Y. Choe and K. A. Holsapple. The Taylor-Galerkin discontinuous finite element method, An explicit scheme for nonlinear hyperbolic conservation laws. *Finite Elements in Analysis and Design*, 10:243–265, 1991.

[14] D. J. Coyle, J. W. Blake, and C. W. Macosko. The kinematics of fountain flow in mold-filling. *AIChE. J.*, 33:1168–1177, 1987.

[15] L. F. A. Douven. *Towards the Computation of Properties of Injection Moulded Products: Flow- and Thermally Induced Stresses in Amorphous Thermoplastics.* PhD thesis, Eindhoven University of Technology, 1991.

[16] F. Dupret and L. Vanderschuren. Calculation of the temperaure field in injection molding. *AIChE. J.*, 34:1959–1972, 1988.

[17] H. Eckardt. Co-injection charting new territory and opening new markets. *J. of Cellular Plastics*, 23:555–592, 1987.

[18] J. D. Ferry. *Viscoelastic Properties of Polymers.* John Wiley & Sons, New York, third edition, 1980.

[19] P. J. Garner and D. F. Oxley, 1969. British patent No.1, 156, p.217, Assigned to ICI.

[20] P. E. Gill, W. Murray, and M. H. Wright. *Practical Optimizatiom.* Academic Press, London, 1981.

[21] C. G. Gogos, C. Huang, and L. R. Schmidt. *Pol. Eng. Sci.*, 26:1457, 1986.

[22] C. A. Hieber. In A. I. Isayev, editor, *Injection and Compression Molding Fundamentals*, chapter 1. Marcel Dekker, Inc., 1987.

[23] C. A. Hieber and S. F. Shen. A finite-element/finite-difference simulation of the injection-molding filling process. *J. Non-Newtonian. Fluid Mech.*, 7:1–32, 1980.

[24] C. Hirsch. *Numerical computation of internal and external flows. Vol 1 & 2.* John Wiley and Sons, Chicester, 1988.

[25] J. Honerkamp. Ill-posed problems in rheology. *Rheol. Acta*, 28:363–371, 1989.

[26] J. Honerkamp and J. Weese. Determination of the relaxation spectrum by a regularization method. *Macromolecules*, 22:4372–4377, 1989.

[27] J. Honerkamp and J. Weese. Tikhonovs regularization method for ill-posed problems. *Continuum Mech. Thermodyn.*, 2:17–30, 1990.

[28] C. L. Tucker III. *Fundamentals of Computer Modeling for Polymer Processing.* Hanser Publishers, Munich, 1991.

[29] H. Janeschitz-Kriegl. *Polymer Melt Rheology anf Flow Birefringence.* Springer-Verlag, Berlin, 1983.

[30] M. R. Kamal, E. Chu, P. G. Lafleur, and M.E. Ryan. Computer simulation of injection mold filling for viscoelastic melts with fountain flow. *Pol. Eng. and Sc.*, 26:190–196, 1986.

[31] M. R. Kamal and P. G. Lafleur. Computer simulation of injection molding. *Pol. Eng. and Sc.*, 22:1066–1074, 1982.

[32] A. Kaye. Technical Report Note No. 134, College of Aeronautics, Cranfield, U.K., 1962.

[33] K. Koenen. Flux-limiting methods and the implementation of Van leer's scheme in PHOENICS. Technical report, Institute for Continuing Education, Eindhoven University of Eindhoven, 1991.

[34] P. G. Lafleur and M. R. Kamal. A structure-oriented computer simulation of the injection molding of viscoelastic crystalline polymers part I: Model with fountain flow, packing, solidification. *Pol. Eng. and Sc.*, 26:92–102, 1986.

[35] R. G. Larson. *Constitutive Equations for Polymer Melts and Solutions.* Butterworths, Boston, 1988.

[36] H. M. Laun. Description of the non-linear shear behaviour of a low density polyethylene melt by means of an experimentally determined strain dependent memory function. *Rheol. Acta*, 17:1–15, 1978.

[37] H. M. Laun. Prediction of elastic strains of polymer melts in shear and elongation. *J. of Rheol.*, 30:459–501, 1986.

[38] P. Leblans. *Constitutive analysis of the nonlinear viscoelasticity of polymer fluids in various types of flow.* PhD thesis, University of Antwerpen, 1986.

[39] A. I. Leonov. Nonequilibrium thermodynamics and rheology of viscoelastic polymer media. *Rheol. Acta*, 15:85–98, 1976.

[40] A. I. Leonov. On a class of constitutive equations for viscoelastic fluids. *J. Non-Newtonian Fluid Mech.*, 25:1–59, 1987.

[41] A. I. Leonov, E. H. Lipkina, E. D. Paskhin, and A. N. Prokunin. Theoretical and experimental investigation of shearing in elastic polymer liquids. *Rheol. Acta*, 15:411–426, 1976.

[42] I. Manas-Zloczower, J. W. Blake, and C. W. Macosko. Space-time distribution in filling a mold. *Pol. Eng. Sci.*, 27:1229–1235, 1987.

[43] H. Mavridis, A. N. Hrymak, and J. Vlachopoulos. Finite element simulation of fountain flow in injection molding. *Pol. Eng. and Sc.*, 26:449–454, 1986.

[44] H. Mavridis, A. N. Hrymak, and J. Vlachopoulos. The effect of fountain flow on molecular orientation in injection molding. *J. of Rheol.*, 32:639–663, 1988.

[45] N. Orbey and J. M. Dealy. Determination of the relaxation spectrum from oscillatory shear data. *J. of Rheol.*, 35:1035–1049, 1991.

[46] A. C. Papanastasiou, L. E. Scriven, and C. W. Macosko. An integral constitutive equation for mixed flows: viscoelastic characterization. *J. Rheol.*, 27:387–410, 1983.

[47] G. W. M. Peters. Modeling of the injection moulding of reactive materials. Technical Report WFW 89050, Eindhoven University of Technology, 1989.

[48] G. W. M. Peters, 1992. Private communication.

[49] O. Pironneau. *Finite elements methods for fluids.* John Wiley and Sons, Chicester, 1989.

[50] M. Pourquié. Numerical comparison of advection schemes to be used on a coarse grid. Technical Report MEAH-94, Laboratory for Aero- and Hydrodynamics, Delft University of Technology, 1990.

[51] W. H. Press, B. P. Flannery, A. A. Teukolsky, and W. T. Vetterling. *Numerical Recipes; The Art of Scientific Computing.* Cambridge University Press, New York, 1988.

[52] W. Rose. *Nature*, 191:242, 1961.

[53] L. R. Schmidt. A special mold and tracer technique for studying shear and extensional flows in a mold cavity during injection molding. *Pol. Eng. Sci.*, 14:797–800, 1974.

[54] B. J. R. Scholtens. Linear thermoviscoelasticity and characterization of noncrystalline epdm rubber networks. *J. of Pol. Sci: Pol. Phys. Ed.*, 22:317–344, 1984.

[55] M. J. H. Schouenberg. A comparison of two constitutive equations for non linear visco-elastic material behaviour in shear flow. Master's thesis, Eindhoven University of Technology, 1991. (in Dutch).

[56] C. W. M. Sitters. *Numerical Simulation of Injection Moulding.* PhD thesis, Eindhoven University of Technology, 1988.

[57] R. K. Upadhyay, A. I. Isayev, and S. F. Shen. Transient shear flow behavior of polymeric fluids according to the Leonov model. *Rheol. Acta*, 20:443–457, 1981.

[58] P. J. L. van der Velden. Particle tracking in reactive flows. Master's thesis, Eindhoven University of Technology, 1991. (in Dutch).

[59] B. van Leer. Towards the ultimate conservative difference scheme. ii. monotonicity and conservation combined in a second-order scheme. *J. of Comp. Phys.*, 14:361–370, 1974.

[60] G. Verbeek. Estimation of non-linear dynamical systems with application to landing gear. Technical report, Institute for Continuing Education, Eindhoven University of Technology, 1991.

[61] E. Vos, H. E. H Meijer, and G. W. M. Peters. Multilayer injection molding. *Int. Pol. Proc.*, 6:42–50, 1991.

[62] M. H. Wagner. Analysis of time-dependent non-linear stress-growth data for shear and elongational flow of a low-density branched polyethylene melt. *Rheol. Acta*, 15:136–142, 1976.

[63] M. H. Wagner. Prediction of primary normal stress difference from shear viscosity data using a single integral constitutive equation. *Rheol. Acta*, 16:43–50, 1977.

[64] M. H. Wagner. A constitutive analysis of uniaxial elongational flow data of a low-density polyethylene melt. *J. of Non-Newtonian Fluid Mech.*, 4:39–55, 1978.

[65] M. H. Wagner, T. Raible, and J. Meissner. *Rheol. Acta*, 18:427, 1979.

[53] L. R. Schmidt. A special mold and tracer technique for studying shear and extensional flows in a mold cavity during injection molding. *Pol. Eng. Sci.*, 14:797–800, 1974.

[54] B. J. R. Scholtens. Linear thermoviscoelasticity and characterization of noncrystalline epdm rubber networks. *J. of Pol. Sci: Pol. Phys. Ed.*, 22:317–344, 1984.

[55] M. J. H. Schouenberg. A comparison of two constitutive equations for non linear visco-elastic material behaviour in shear flow. Master's thesis, Eindhoven University of Technology, 1991. (in Dutch).

[56] C. W. M. Sitters. *Numerical Simulation of Injection Moulding.* PhD thesis, Eindhoven University of Technology, 1988.

[57] R. K. Upadhyay, A. I. Isayev, and S. F. Shen. Transient shear flow behavior of polymeric fluids according to the Leonov model. *Rheol. Acta*, 20:443–457, 1981.

[58] P. J. L. van der Velden. Particle tracking in reactive flows. Master's thesis, Eindhoven University of Technology, 1991. (in Dutch).

[59] B. van Leer. Towards the ultimate conservative difference scheme. ii. monotonicity and conservation combined in a second-order scheme. *J. of Comp. Phys.*, 14:361–370, 1974.

[60] G. Verbeek. Estimation of non-linear dynamical systems with application to landing gear. Technical report, Institute for Continuing Education, Eindhoven University of Technology, 1991.

[61] E. Vos, H. E. H Meijer, and G. W. M. Peters. Multilayer injection molding. *Int. Pol. Proc.*, 6:42–50, 1991.

[62] M. H. Wagner. Analysis of time-dependent non-linear stress-growth data for shear and elongational flow of a low-density branched polyethylene melt. *Rheol. Acta*, 15:136–142, 1976.

[63] M. H. Wagner. Prediction of primary normal stress difference from shear viscosity data using a single integral constitutive equation. *Rheol. Acta*, 16:43–50, 1977.

[64] M. H. Wagner. A constitutive analysis of uniaxial elongational flow data of a low-density polyethylene melt. *J. of Non-Newtonian Fluid Mech.*, 4:39–55, 1978.

[65] M. H. Wagner, T. Raible, and J. Meissner. *Rheol. Acta*, 18:427, 1979.

[66] M. L. Williams, R. F. Landel, and J. D. Ferry. *J. Am. Chem. Soc.*, 77:3701, 1955.

[67] W. F. Zoetelief and G. W. M. Peters. Multilayer injection moulding: Particle tracking. In *Procedings 8th Annual Meeting Pol. Proc. Soc., New Delhi India*, pages 99–100, march 1992.